Cell Performance and Anodic Processes
in Aluminium Smelting
Studied by Product Gas Analysis

by

Mark Murray Radley Dorreen

A thesis submitted to the University of Auckland
in fulfilment of the requirements for the degree of
Doctor of Philosophy in Engineering

Auckland   **May 2000**

Abstract

Aluminium smelting is an energy intensive process, and as a result there has been considerable and ongoing research over a number of decades on the energy efficiency of various aspects of the process. One of the most important measures is current efficiency, which has been shown to have direct relationships with current density, cell temperature, electrolyte chemistry, and anode-cathode distance. The effects of these variables on current efficiency are generally accepted, however there remains debate over the influence of the alumina concentration in the electrolyte on current efficiency.

This research relied upon the development of a laboratory scale aluminium smelting cell where the current efficiency was measured via sampling of the product gases. A modified oxygen balance was used, with gas analysis performed using online mass spectrometry.

The findings of this research agreed with the accepted current efficiency trends, showing a current density influence of 17.25 %CE per A/cm^2, over the range 0.3 and 1.1 A/cm^2. The influence of electrolyte chemistry was -7.8 %CE per unit cryolite molar ratio, between cryolite ratios 1.99 and 3. The anode-cathode distance was shown to have no influence on current efficiency in this cell, contradicting the established findings, however this was expected because of the design of the cell with no metal pad at the cathode and therefore constant mass transfer conditions at all the anode-cathode distances used.

The most significant finding concerning current efficiency is that the variation with alumina concentration is so small, -0.0376 %CE/wt% Al_2O_3, that there is effectively no influence. While in many other studies an influence was found, the values and direction of the relationship varied. This suggests that in many cases the observed variation in current efficiency was actually caused by a change in the level of stability in the cell, by processes such as dissolution of sludge from the cathode or the thermal disturbance of alumina feeding, whereas in this research the cell was stable under all operating conditions.

In recent years there has been significant focus on the environmental impact of the emissions from aluminium smelters. Of particular interest are the perfluorocarbons and sulfurous species, because of the impact on global warming and the ozone layer.

Thermodynamic predictions indicate that the CF_4 formed at anode effect is in concentrations orders of magnitude higher than C_2F_6. Gas analysis from a cell going onto anode effect shows CF_4 formed only after the cell voltage has increased stepwise. The role of carbonyl fluoride in the onset of anode effect was investigated, and COF_2 was detected in the product gas shortly before the anode effect began. This indicates that COF_2 is a precursor to anode effect, by being formed as the anode polarisation increases before the anode effect begins. Voltage analysis shows the polarisation increases sufficiently to allow the electrolytic formation of COF_2. Once formed, the COF_2 then reacts with anode carbon, forming the initial layer of CF_4 under the anode. The thickness of the CF_4 layer increases until it becomes insulating, causing the voltage to increase suddenly in what is traditionally viewed as the anode effect onset, after which CF_4 and C_2F_6 are formed electrolytically.

Sulfur dioxide has generally been considered the most important sulfurous species in the waste gases from aluminium smelting. The sulfur in the anode carbon, however, is initially released as carbonyl sulfide in the zone under the anodes where the oxidation potential is low. The COS is then oxidised to SO_2 as it passes through progressively increasing oxidation potential zones, until it is released from the cell in the drafting air and most of the COS has reacted.

Acknowledgements

Table of Contents

List of Figures

List of Tables

1.   Introduction.

Approximately 20 million tonnes of aluminium are produced commercially each year by the Hall-Héroult process, which is both energy and materials intensive and produces environmentally unfriendly secondary products. Because of the vast amounts of energy consumed, the efficiency of the process, most commonly measured by the current efficiency, is of great importance. This can be measured in different ways, and used to demonstrate the performance of aluminium smelting cells with respect to different operating variables.

The variables that impact on current efficiency and are important to cell operation are cell temperature, current density, anode-cathode distance, electrolyte chemistry, and alumina concentration. Of these, alumina concentration is considered the most important because as alumina is the main raw material consumed in the process, the alumina content in the electrolyte varies significantly during electrolysis. Because of this the impact of alumina concentration on current efficiency is an important consideration in alumina feeding strategies. However, in spite of this the volume of research carried out both in industry and academia still provides a conflicting picture into the effect of alumina concentration on current efficiency, with some researchers showing a positive influence of alumina, others a negative influence and even no influence at all.

As the alumina concentration in the electrolyte is depleted through electrolysis, the operating mode of the cell passes through a transition into anode effect, when the voltage across the cell increases dramatically and large amounts of tetrafluoromethane (CF_4) and hexafluoroethane (C_2F_6) are generated. The anode effect is detrimental because of the extra energy consumed, the disruption to the stability of the cell, and the fluorocarbon gases released which have a far greater effect on global warming through the greenhouse effect than the carbon dioxide formed during normal electrolysis. While the operational impact of the anode effect phenomenon has been studied extensively, and more recently the environmental impact has attracted more attention, there is still uncertainty over the mechanisms surrounding the onset of anode effect.

1

The widely believed theory of spontaneous formation of CF_4 at increased cell voltage is challenged by the theory of carbonyl fluoride (COF_2) formation as an intermediate compound leading to CF_4 formation.

1.1.   Purpose of this Research.

The main aim of this project was to investigate the relationship between current efficiency and the cell variables anode-cathode distance, current density, electrolyte chemistry and most importantly alumina concentration in the aluminium smelting cell. The main tool used was gas analysis and the oxygen balance technique to determine current efficiency. However, while doing this it also branched out to investigate the related and very relevant issues of the anode effect phenomenon, other gases formed in the aluminium smelting cell such as fluoride and sulfurous species, and the polarisation components of the cell voltage. A combination of cell voltage analysis and gas analysis was used to investigate the anode effect and its onset.

1.2.   Scope of the Experimental Work.

To perform this research it was required to develop a system that enabled experimentation in the laboratory. This included the modification and maintenance of a laboratory furnace, the design and construction of a laboratory scale aluminium cell, the installation of the gas analysis equipment used to capture the analytical data, and the set-up of computerised controlling and data acquisition systems. The development of the experimental system as a whole contained considerable evolution as difficulties were encountered and overcome until the set-up that best suited the experimental requirements was found.

Experiments were performed investigating the effects of anode-cathode distance, current density, electrolyte chemistry and alumina concentration on current efficiency. Experiments were also performed to investigate the different gas species, of a fluoride and sulfurous nature, produced during both normal electrolysis and anode effect. Particular attention was paid to the onset of anode effect, and the role played by carbonyl fluoride at that time. These experimental measurements were compared to theoretical equilibrium gas composition

predictions that were made. The cell voltage during electrolysis was analysed to highlight the anode reaction polarisation and the magnitude of its change as anode effect was approached.

1.3. Coverage of the Thesis.

The second chapter of this thesis provides a general background into the theory of aluminium smelting, and looks at the energy requirements of the electrolysis process. Current efficiency, and the different methods used to determine it, are described in detail, especially the oxygen balance method applied here. The effects of cell variables on current efficiency are presented, and the areas where there is uncertainty over the effects of variables on current efficiency are highlighted. The anode effect phenomenon, as well as carbon consumption and sulfurous gas species arising from aluminium production are all discussed.

The theory behind gas analysis, in particular the mass spectrometric method used in this study, is given in chapter 3. The gas analysis system used is described in detail, showing the set-up and how it was operated. The design and operation of the laboratory scale aluminium cell is also described in detail in chapter 4, describing how it was linked to and operated with the gas analysis system.

The current efficiency determination algorithm is outlined in chapter 5, giving the accuracy of the method and crosschecks to verify the values given.

In chapter 6 the general performance of the laboratory cell is demonstrated, and then in more detail the influence of the variables mentioned above on current efficiency. In particular the findings of the influence of alumina concentration are presented, compared to previous studies, and justified.

The cell voltage analysis is presented in chapter 7, showing the complimentary results of the independent methods of current interruption and cell voltage breakdown. The magnitude of the anode reaction polarisation increase during electrolysis until anode effect onset is discussed.

Chapter 8 covers the anode effect in detail, showing theoretical predictions of the gas species formed and the changes with different cell oxidation conditions. Experimental measurements of the species detected during anode effect are given, as well as evidence of carbonyl fluoride involvement in the onset of anode effect. The anode effect is linked to the cell voltage and in particular the anode reaction polarisation component.

The theoretical predictions of sulfurous species formed in the cell, and the corresponding experimental measurements, are given in chapter 9.

2. Background and Theory.

2.1. Aluminium Production.

The basic principles behind the only commercially viable method of aluminium production have remained relatively unchanged since 1886, when the process was simultaneously patented by Charles Martin Hall in America and Paul Héroult in France. World primary aluminium production was 4.5 million tonnes in 1960, which increased to 19.4 million tonnes in 1995 [1]. Aluminium is desired for a wide range of applications because of its properties of light weight, high strength and resistance to atmospheric corrosion. The automotive industry is a large consumer of aluminium as lighter, more efficient vehicles are sought after. Other markets include beverage cans, as composites in fabrication and construction material, electrical transmission lines and many more. Because of these various uses, the demand for aluminium and therefore its production is likely to continue to increase.

The Hall-Héroult process is based on the electrolytic reduction of alumina, dissolved in a molten cryolite-based electrolyte, to aluminium using sacrificial carbon as shown in reaction *2.1*.

$$2Al_2O_{3(dissolved)} + 3C_{(solid)} = 4Al_{(liquid)} + 3CO_{2(gas)} \tag{2.1}$$
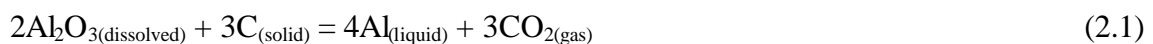
This electrolytic process takes place in large numbers of reactors, known as Hall-Héroult cells or Hall cells. A schematic of a Hall-Héroult cell is shown in Figure 2.1. Features are the steel shell, the carbon lining to contain the electrolyte and protect the steel from corrosive attack, the molten pad of aluminium acting as the cathode surface, and the carbon anodes suspended from the superstructure of the cell. There are two main designs of cell, Söderberg and prebaked anode types. Söderberg cells have one large continuous anode studded with many steel conducting contacts, which is lowered periodically to maintain a constant distance between anode and cathode surfaces. The anode is made as a paste and placed in the cell

over the bath, where it is baked by the heat of the cell. Prebaked anode cells have many smaller anodes, typically in two rows, with one anode replaced every 24-36 hours. The anodes are prebaked in a large baking furnace before being placed in the electrolytic cell.
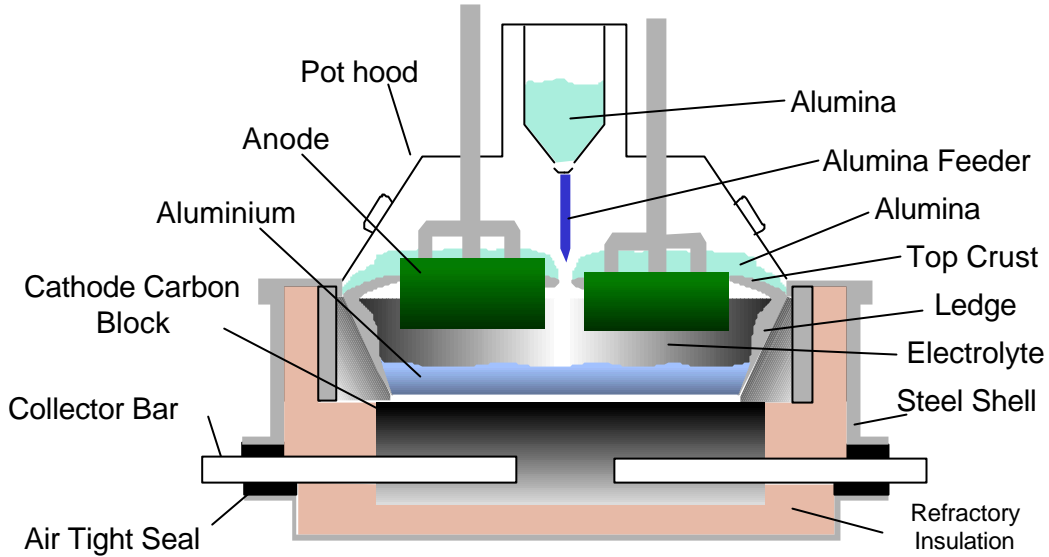
Figure 2.1 *Schematic of a prebaked anode Hall-Héroult cell.*

The main component in the electrolyte is cryolite (Na_3AlF_6), which is the double-salt of sodium fluoride (NaF) and aluminium fluoride (AlF_3). A commonly used term descriptive of the electrolyte is the cryolite or molar ratio (CR), which refers to the molar ratio of sodium fluoride to aluminium fluoride. With pure cryolite the cryolite ratio of NaF to AlF_3 is 3, and as aluminium fluoride is added the cryolite ratio decreases. The cryolite ratio is also referred to as the bath or weight ratio (BR), being the weight ratio of NaF to AlF_3. By coincidence the molecular weight of NaF is almost exactly half that of AlF_3, which makes the bath ratio equal to half of the cryolite ratio. Therefore the bath ratio of pure cryolite is 1.5.

Common additives to the cryolite are calcium fluoride (CaF_2), aluminium fluoride (in excess of the stoichiometric amount from pure cryolite) and sometimes lithium fluoride (LiF) and magnesium fluoride (MgF_2), as well as the reactant alumina. For a typical electrolyte composition, the cryolite ratio can be given by:

$$CR = \frac{1.2\,(100 - CaF_2 - Al_2O_3 - xsAlF_3)}{0.4\,(100 - CaF_2 - Al_2O_3 - xsAlF_3) + xsAlF_3} \tag{2.2}$$

where CaF_2 and Al_2O_3 in wt%, and $xsAlF_3$ is the wt% in excess of that from pure cryolite [2].

These additives have the effect of lowering the melting point from 1010°C to the operating range of 955-975°C. Alumina is maintained in the range 2-6wt% by feeding periodically. Before feeding, the solid crust on the surface of the electrolyte must be broken, either down the entire centre channel or half of the channel with a breaker bar, or in small holes for point feeding. With breaker bar cells, the feeding is less frequent and the amount of alumina dumped into the electrolyte from a hopper above is larger, whereas for point feeding the feeds are frequent and smaller. The production of aluminium is material and energy intensive, with the following inputs to a cell necessary to produce one ton of metal [3]:

- 1.90-1.93 tons of smelter grade alumina
- 0.4-0.47 tons of anode carbon
- 15-50 kg of aluminium fluoride
- 12800-16000 kWh of electrical energy
- considerable volumes of air passing over the top of the anodes and anode insulation to capture gaseous emissions.

Thus one can gain an appreciation of the scale of operation of a modern smelter, with production ranging up to 500,000 tons of aluminium per year.

While the basic aluminium smelting process has not changed much in over 100 years, the energy required to produce one kilogram of aluminium has dropped from 40kWh to less than 13kWh, and the electrical efficiency has increased from 70% to greater than 95% for the best cells [4].

2.2. Cell Energy Requirements.

While the Nernst potential for reaction *2.1* at 975°C is only 1.18V, polarisation (η) and resistive (IR) components raise the cell voltage to around 4.5V.

The overall cell voltage V^{cell} may be expressed as:

$$V^{cell} = E^{rev} + \eta_{an} + \eta_{cat} + \eta_{conc} + IR_{electrolyte} + IR_{bub} + IR_{cat} + IR_{an} + IR_{ext} \qquad (2.3)$$

7

where h_{an}, h_{cat} and h_{conc} are the anode, cathode and concentration polarisations, I is the cell current in amperes, and R is the resistance of the electrolyte, bubble layer, cathode, anode and external connections, in ohms.

E^{rev} is made up of the standard electrode potential ($E°$) and the activity contribution (a) of the species in reaction *2.1*, and can be given by equation *2.4*:

$$E^{rev} = E^o - \frac{RT}{6F} \ln \frac{a_{Al}^2 \cdot a_{CO_2}^{3/2}}{a_{Al_2O_3} \cdot a_C^{3/2}} \tag{2.4}$$

The activities of Al and C are unity as they are pure condensed phases in their standard states. The activity of CO_2 can also be assumed as unity as the nearly pure gas contacts the anode at approximately 1 atmosphere [5].

The standard electrode potential $E°$ is given by the change in Gibbs energy:

$$E^o = -\frac{\Delta G^o}{6F} \tag{2.5}$$

With the activity simplifications, equation *2.4* can be written as:

$$E^{rev} = -\frac{\Delta G^o}{6F} + \frac{RT}{6F} \ln a_{Al_2O_3} \tag{2.6}$$

Based on the data of Rolin [6] the alumina activity can be given by:

$$a_{Al_2O_3} = \left(\frac{\% Al_2O_3}{\% Al_2O_3(sat)} \right)^{2.77} \tag{2.7}$$

This gives an activity contribution to the cell voltage of up to 50mV, however there is some debate as to the value of the index in this equation.

The cathode becomes polarised due to the concentration overvoltage from an accumulation of NaF and depletion of AlF_3 in the boundary layer at the cathode surface. This can be given by the Alcoa equation [7]:

$$\boldsymbol{h}_{cat} = \frac{2.732 - 0.248 \cdot (CR) \cdot T}{34590} \ln \frac{i}{0.257} \tag{2.8}$$

where T is the temperature (Kelvin), i is the cathodic current density (A/cm^2) and CR is the cryolite molar ratio of NaF/AlF$_3$ in the electrolyte. Typical values for cathode polarisation are 60-100 mV [7].

The anodic polarisation or overvoltage, $\boldsymbol{h}_{an}$, is quite large, 0.4-0.6V. It is not known exactly why the anode becomes polarised, although it is thought to be related to reactions with surface complexes. It is often represented by a Tafel equation:

$$\boldsymbol{h}_{an} = a + b \log i \tag{2.9}$$

where a and b are constants (a = 0.4-0.6 V, b = 0.17-0.27 V/decade) and i is the anodic current density (A/cm^2).

There can be a small overvoltage caused by a concentration gradient of alumina adjacent to the anode. This is given by:

$$\boldsymbol{h}_{conc} = \frac{RT}{nF} \ln \left(1 - \frac{i}{i_c} \right) \tag{2.10}$$

It has been assumed that the limiting current density i_c (A/cm^2) is the same as the critical current density for anode effect. The i_c is difficult to estimate for industrial cells, but has been calculated by Piontelli *et al.* [8] for laboratory cells:

$$i_c = \left[5.5 + 0.018(T - 1323) \right] A^{-0.1} \left[(\% \, Al_2O_3)^{0.5} - 0.4 \right] \tag{2.11}$$

where A is the anode area (cm^2). The concentration polarisation, $\boldsymbol{h}_{conc}$, is small, in the range 5-10 mV, and is not often considered, or may be included in the anode polarisation.

Although the combined anode and concentration overpotential data for laboratory and plant seldom agree closely, the trends are generally similar for current density and alumina concentration [9]:

Table 2.1 Anode Polarisation in the Laboratory and Plant [9].

Al_2O_3 (wt%)	Current Density (A/cm^2)					
	0.7		0.9		1.1	
	Overvoltage (V)					
	Lab.	Plant	Lab.	Plant	Lab.	Plant
1.5	-	0.95	-	1.09	-	1.23
2	0.65	0.84	0.71	0.98	0.76	1.13
5	0.54	0.51	0.63	0.65	0.70	0.81

The difference between laboratory and plant data is due to any or all of the following:

- concentration gradients in the cell,

- variations in carbon quality,

- different electrode orientations,

- and different electrolyte composition ranges.

The voltage drop through the electrolyte, $IR_{electrolyte}$, and across the bubble layer under the anode, IR_{bub}, are often calculated separately. The electrolyte resistance is easily calculated from many published correlations, however the bubble resistance is more difficult to determine. An equation which combines them and gives the total resistivity in the inter-electrode gap is given by Hyde and Welch [10]:

$$R_{electrolyte} = \frac{1}{kA}\left[(D - d_b) + \frac{d_b}{(1 - \boldsymbol{j})}\right]$$
(2.12)

where k is the electrical conductivity of the electrolyte ($\Omega^{-1}m^{-1}$), A is the electrode area (cm^2), D is the inter-electrode spacing (cm), d_b is the bubble layer thickness (cm) and $\boldsymbol{j}$ is the anode surface fractional gas coverage. Aarberg *et al*. [11] determined the average bubble layer thickness to be 0.5cm and the average fractional anode surface coverage to be about 0.45 by experimentation in a laboratory scale cell. There are many different correlations for electrolyte

10

conductivity, most of which give consistent values of about 2-2.5 $\Omega^{-1}m^{-1}$ for a normal electrolyte composition and temperature. For the purposes of this study the conductivity equation given by Wang *et al.* [12] was used, while another recent publication by Hives *et al.* [13] also gives an expression for electrolyte conductivity.

The remaining three terms in equation *2.3* can be grouped together as they are the voltage drops through the anode carbon, IR_{an}, though the cathodes, IR_{cat}, and across all the connections that make up the circuit from one cell to the next, IR_{ext}. The external voltage drops should remain relatively constant, although the cathode drop changes slowly with time. Obviously, for any single anode the voltage drop will decrease as the anode becomes smaller through consumption, but the combined effect of all anodes in the cell should be minimal. The cathode voltage drop generally increases slowly with time over the life of the cell through processes such as sodium intercalation [14].

A schematic of the voltage drops in a cell is shown in Figure 2.2.

Voltage component	Volts
External (anode)	0.10
Contact (anode)	0.05
Anode	0.33
Reaction E^{rev}	1.18
Polarisation (anode)	0.48
Electrolyte	1.42
Polarisation (cathode)	0.05
Cathode	0.33
Contact (cathode)	0.06
External (cathode)	0.30
Total voltage	4.30
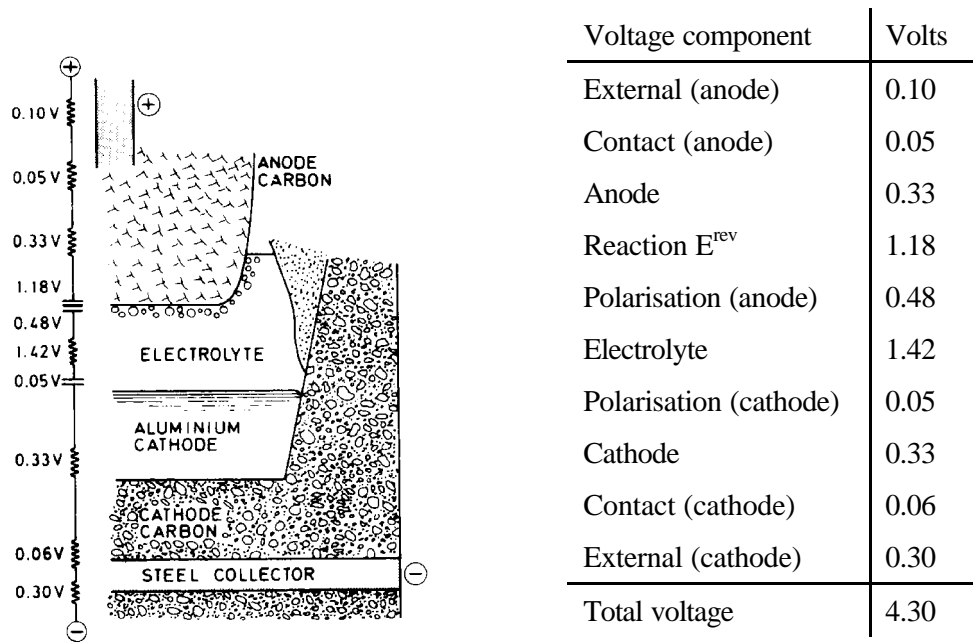
Figure 2.2 *Schematic of the voltage drops through a cell with anodic current density of 0.7 A/cm^2, taken from Grjotheim and Welch [14].*

In this diagram the IR_{bub} term is included in the electrolyte voltage drop, and the concentration polarisation is included in the anode polarisation term. As seen in reactions *2.8* and *2.9*, the cathode and anode polarisations are dependent on the current density. The cathode voltage

11

drop changes with cell age as the cathode changes condition through sodium intercalation, and the cathode contact voltage drop also changes with age as the contact between the cathode and the steel current collector bar degrades. The voltage drops where the current carrying metal is connected to the carbon anode and cathodes will vary depending on the jointing technique used.

The resistive heating of the electrolyte provides the energy to maintain the cell at the operating temperature, and the cell must be carefully controlled to ensure the heat balance is maintained. Heat is lost from the cell through the sides and base of the shell, through the cathode current collector bars, as convection from the top of the frozen electrolyte crust, from the top of the anodes and in the heated cell gas out the exhaust fume ducting.

2.3. Current Efficiency.

The main process occurring in an alumina reduction cell is the production of aluminium metal, as described by reaction *2.1*. Faraday's law can be used to relate the theoretical production of metal to the cell current:

$$P = \frac{MI}{zF}$$
(2.13)

where P is the amount of metal produced at the cathode (g/s), M is the molecular weight of the metal (g/mol), I is the cell current (A), z is the number of electrons in the reaction and F is Faraday's constant.

According to Faraday's law as shown in equation *2.13* the production of aluminium will be 0.168kg/kiloampere-hour at 100% efficiency. Thus for a modern 280kA smelter, each cell is theoretically capable of producing more than 1100kg of aluminium per day. However any reactions competing with the main reaction *2.1* or any back-reactions will result in a reduction in the amount of aluminium produced.

The ratio of the actual aluminium metal produced to the theoretical aluminium metal produced per unit of electric current is known as the "Current Efficiency". The aluminium produced has

a low solubility in the electrolyte, where the dissolved metal can react in several ways. The main back reaction is the re-oxidation of dissolved aluminium to alumina, with carbon dioxide reduced to carbon monoxide:

$$2Al_{(dissolved)} + 3CO_{2(gas)} = Al_2O_{3(dissolved)} + 3CO_{(gas)} \qquad (2.14)$$
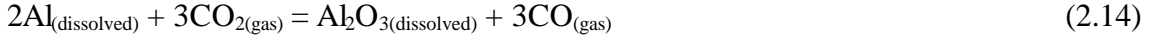
Re-oxidation of the main electrolysis products reduces the amount of metal produced at the cathode relative to current, and is the main cause of lost current efficiency. Loss in efficiency also affects the specific energy consumption E [14], which is given by:

$$E = \frac{2.980 \cdot V}{x} \quad \text{kWh per kg Al} \qquad (2.15)$$

where V is the cell voltage and x is the fractional current efficiency, given by

$$x = \frac{per\ cent\ current\ efficiency}{100\%} \qquad (2.16)$$

Thus it can be seen that for minimum energy consumption the cell voltage must be as low as possible and the current efficiency as close to 100% as possible. The minimum theoretical energy consumption is 3.52 kWh/kg Al, although because of the increased cell voltage discussed earlier and less than 100% current efficiency, present cell technology operates at around 13kWh/kg Al.

As well as the main back reaction *2.14*, there are many other reactions that consume electric current without producing the maximum theoretical yield of aluminium. Some of these are:

- the electrolytic formation of CO, which is particularly important at areas of low current density such as the sides of the anode:

$$Al_2O_{3(dissolved)} + 3C_{(s,anode)} = 2Al_{(l)} + 3CO_{(g)} \qquad (2.17)$$

- metal shorting (at the anode):

$$Al_{(dissolved)} = Al^{3+}{}_{(dissolved)} + 3e^- \qquad (2.18)$$

13

- the reduction of CO and CO_2 gas by dissolved aluminium to C:

$$3CO_{(gas)} + 2Al_{(dissolved)} = 3C_{(s)} + Al_2O_{3(dissolved)} \qquad (2.19)$$

$$3CO_{2(gas)} + 4Al_{(dissolved)} = 3C_{(s)} + 2Al_2O_{3(dissolved)} \qquad (2.20)$$

- the formation of aluminium carbide:

$$4Al_{(l)} + 3C_{(s,lining)} = Al_4C_{3(s)} \qquad (2.21)$$
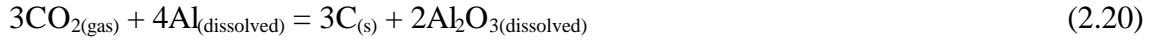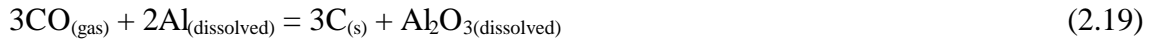
- and the reoxidation of any dissolved aluminium carbide, which while not affecting current efficiency directly, it does promote further aluminium carbide formation:

$$Al_4C_{3(dissolved)} + 9CO_{2(g)} = 2Al_2O_{3(dissolved)} + 12CO_{(g)} \qquad (2.22)$$

Although there are many possible reactions resulting in a lowering of faradaic current efficiency, it is generally recognised that the main reaction lowering efficiency is the back reaction *2.14*, and the contribution to inefficiency from these other reactions is small [15]. The mechanism of the back reaction has been studied in detail to determine the rate controlling step. Figure 2.3 depicts the generation of CO_2 at the anode and the recombination with metal originating from the cathode.
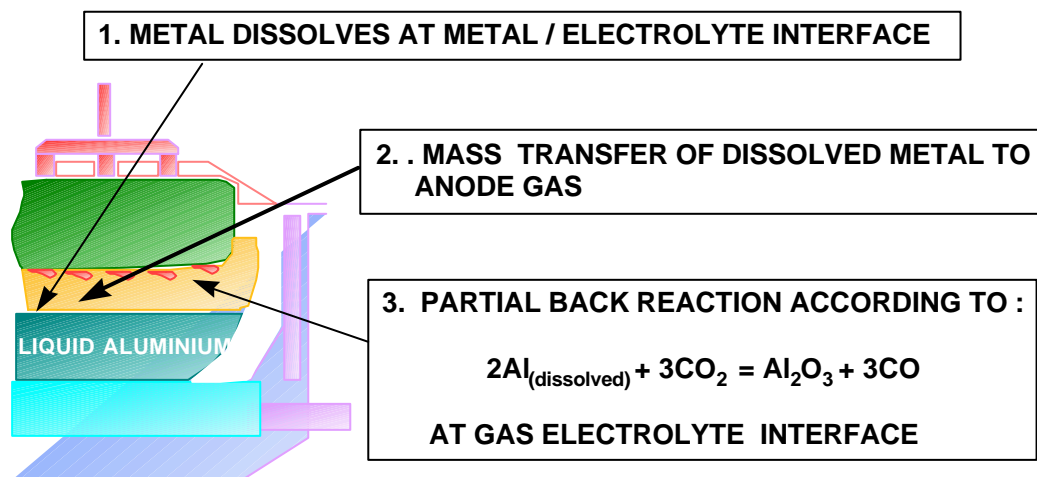
Figure 2.3 *Schematic of the back-reaction zones, with simplified reaction steps.*

Zhang [16] proposed four different back-reaction schemes differing in the level of electrolyte mixing and reaction rates, and listed nine steps for the back-reaction. These can be simplified to the following four steps:

For the metal:

1) Dissolution of metal to saturation at the metal-electrolyte interface.

2) Transport of metal through the boundary layer by diffusion.

3) Mass transfer of dissolved metal through the bulk electrolyte to the reaction interface by convection and some diffusion.

4) Chemical reaction between dissolved metal and either dissolved or gaseous carbon dioxide at the reaction interface.

If dissolved carbon dioxide is considered the reacting phase, then additional steps can be written for CO_2:

5) Dissolution of CO_2 at the bubble-electrolyte interface.

6) Mass transfer of dissolved CO_2 through the boundary layer at the electrolyte-gas interface by diffusion.

7) Mass transfer of dissolved CO_2 to the reaction interface zone by convection and some diffusion.

There have been numerous studies to determine the rate-controlling step of metal reoxidation. Zhang [16] reviewed a number of these, which showed that for laboratory cells with limited convection or stirring the rate controlling step is (3). When rapid mass transfer is ensured through vigorous agitation the rate controlling steps are (1) and/or (2).

The solubility of both aluminium and carbon dioxide in the electrolyte are important to the back-reaction process. The solubility of aluminium in a given electrolyte is not known exactly, although several correlations are available in the literature. Electrolyte additives can be used to lower the aluminium solubility, and at the same time lower the liquidus temperature, which is also desired. The effects of electrolyte additives are discussed in more detail in section 2.5.3.

Although the solubility of carbon dioxide in the electrolyte is thought to be much lower than that of aluminium, it still could be important in the back reaction steps because of the large gas/electrolyte interface area due to the gas bubbles. The electrolyte/metal interface area is smaller, inspite of the deformation due to the metal pad wave motion.

15

2.4. Methods for Measuring Current Efficiency.

The desire to operate cells at the highest possible current efficiency has led to the development of many different methods for measuring the efficiency. The variety is due in part to the technology available when each was developed, and also the specific motivation for the current efficiency measurement.

There are two main types of methods, the first based on accounting for the aluminium produced, and the second on analysing the waste gases released.

2.4.1. Aluminium Balance.

The conventional method for measuring current efficiency has been to compare the weight of metal produced with the theoretical faradaic production. This gives accurate efficiencies, and can give the current efficiency for a single cell or an entire pot-line, but has the main disadvantage of being slow. The average current efficiency can only be determined over a long time frame, such as several weeks or months.

Methods with a faster response but still based on the amount of aluminium produced involve using tracers which are placed in the cell. The dilution over time can be used to determine the metal produced and hence the current efficiency. Tracers used include copper, silver, and radioactive cobalt, zirconium, iridium and gold. While the tracer techniques enable current efficiencies to be determined in a shorter time, the equipment and sampling needed mean they can be complicated.

The main disadvantage of the methods based on comparing actual and theoretical metal production is that they take no account of specific events occurring in the cell. The major interruptions to steady operation include anode removal and replacement, lowering of anodes to maintain inter-electrode spacing, crust breaking and alumina feeding, anode effects, and depletion of alumina between feeds. Whilst long term current efficiency data is important, the short term variation is equally important as even the smallest gain in efficiency has a large economic benefit.

As a result, more rapid response methods of measuring current efficiency have been investigated. The gas-analysis techniques overcome the problems of obtaining short term data and a fast response time, and are described below.

2.4.2. Gas Analysis and the Pearson-Waddington Equation.

The basis for the gas analysis method of measuring current efficiency was promoted by Pearson and Waddington in 1947 [17]. They observed that the current efficiency was related to the amount of carbon dioxide in the anode gas produced. This led to the well known Pearson-Waddington (P-W) equation for current efficiency:

Current Efficiency % = ½(% CO content of anode gases) + 50 (2.23a)

The assumption behind this equation is that the main reaction *2.1* producing metal and the main back reaction *2.14* reoxidising metal are the only reactions occurring in the cell. The PW equation can be written in a different form due to the ratio of the gases formed in the main forward and back reactions:

$$\% CE = 1 - 0.5 \left(\% CO_{(gas)} \right)$$ (2.23b)

and can also be written to allow for dilution of the anode gases, as may be the case in laboratory cells with a carrier gas:

$$\% CE = 0.5 + 0.5 \left[\frac{yCO_2}{yCO + yCO_2} \right]$$ (2.23c)

where yCO_2 and yCO are the fractions of those species in the total gas from the cell.

This simple equation allowed the current efficiency to be determined by sampling the anode gases from a particular anode, or from the exhaust duct of a cell. The gas analysis technique could vary, with samples analysed on site if the equipment allowed, or later in a laboratory. The current efficiency could be determined as frequently as gas samples could be taken. In this way the performance of a cell could now be monitored through different events rather than

just gaining a long term average measure. As an approximation to the current efficiency the Pearson-Waddington equation is useful, as it simplifies the gas analysis required to only determining the amount of carbon dioxide and/or carbon monoxide released.

The P-W equation is based on ratio of CO_2 to CO, and the assumption that the only reaction altering the CO_2/CO ratio is also the only reaction responsible for lowering the current efficiency. However, the assumption of only the main reaction and back-reaction occurring can easily be challenged. There are many reactions that reduce the current efficiency without affecting the CO_2/CO ratio, some that affect the CO_2/CO ratio without affecting the current efficiency and also those which cause a change in both gas ratio and efficiency. Some of these are listed in section 2.3 (Current Efficiency). In both metal shorting (reaction *2.18*) and the formation of aluminium carbide (reaction *2.21*) no gas is formed. The reduction of CO and CO_2 and the oxidation of aluminium carbide (reactions *2.19*, *2.20*, *2.22*) all alter the gas ratio. Some other important reactions between carbon, oxygen, CO_2 and CO are:

$$C_{(s,anode)} + CO_{2(g)} = 2CO_{(g)} \tag{2.24}$$

$$2CO_{(g)} + O_{2(g)} = 2CO_{2(g)} \tag{2.25}$$

$$C_{(s,anode)} + O_{2(g)} = CO_{2(g)} \tag{2.26}$$

$$2C_{(s,anode)} + O_{2(g)} = 2CO_{(g)} \tag{2.27}$$

Reaction *2.24*, otherwise known as the Boudouard reaction, is considered to play a very important role as it can proceed in anoxic environments such as under the crust and under the anode where the carbon dioxide is initially formed. Figure 2.4 shows the equilibrium constant of the Boudouard reaction, indicating its extreme favourability at the temperatures encountered in the cell. In fact, the reaction still proceeds in a forward direction down to 702°C, so as carbon dioxide bubbles are released and travel up the side of the anode they can still react with the anode carbon. There is a decreasing temperature profile up the anode as shown in Figure 2.6. The sides of the anode may become eaten away in a concave manner, and the anode gas may be partially trapped or held in this region, increasing the possibility for reaction.

18
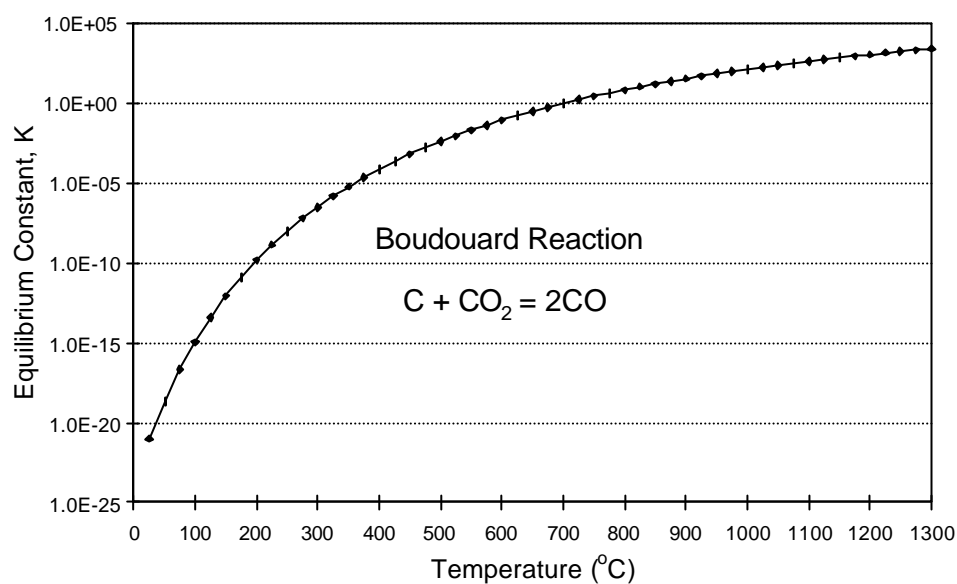
Figure 2.4 *Equilibrium constant for the Boudouard reaction.*

Reactions *2.26* and *2.27* are important as they indicate that any anode carbon exposed to air at a suitable temperature will react, increasing the amount of carbon used and also altering the CO_2/CO ratio. These two reactions are more significant at temperatures lower than for the Boudouard reaction, as seen in Figure 2.5.
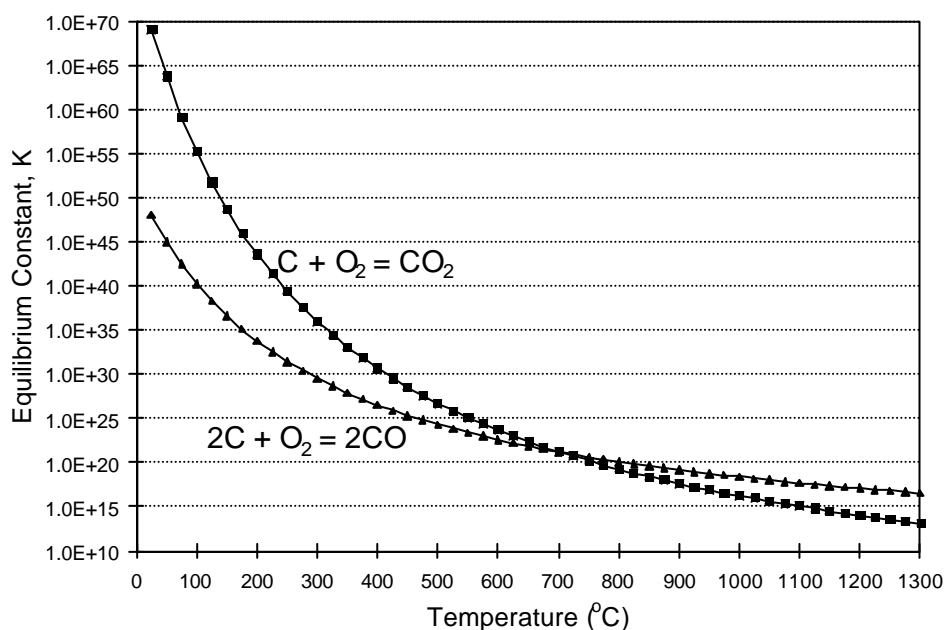
Figure 2.5 *Equilibrium Constant of Airburn Reactions 2.26 and 2.27.*

19

The forward equilibrium is very large for both reactions, although the formation of CO_2 is favoured at temperatures below 700°C. Figure 2.6 illustrates the temperature profile through the anode, and the temperatures in the regions where carbon is exposed to air.
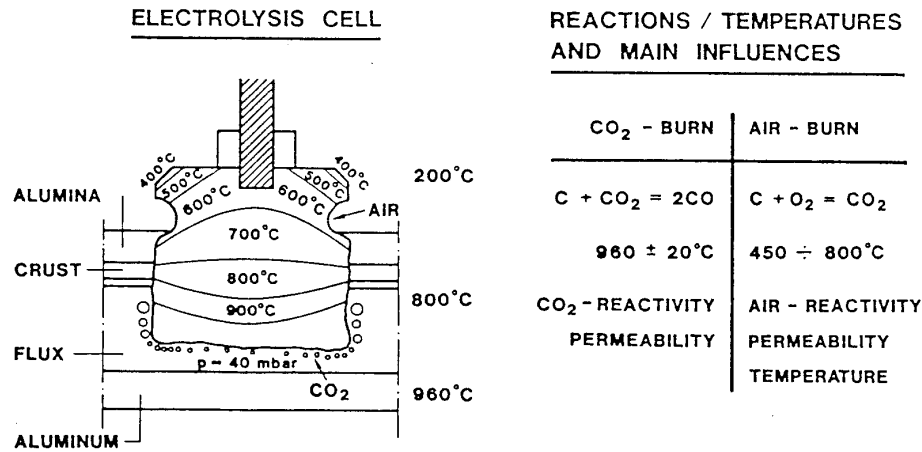
Figure 2.6 *Anode temperature profile and reactions, taken from Fischer and Perruchoud [18].*

The temperature of the submerged carbon is above 800°C, where the Boudouard reaction will be dominant. Carbon above the level of electrolyte ranges in temperature up to 800°C, although the insulating frozen electrolyte crust and alumina cover should ensure that carbon is only exposed to air at temperatures below 600°C. In this zone above the electrolyte only a very small amount of CO will be formed by air-burn (reaction *2.27*) as CO_2 is the favoured product at temperatures below 700°C (reaction *2.26*).

CO formed elsewhere by the Boudouard reaction, direct electrolysis or back reaction and released through cracks and holes in the crust can burn with oxygen via reaction *2.25*. The thermodynamics of this reaction are favourable also, and the combustion flames may cause localised areas to have temperatures of up to 1300°C.

2.4.3.   The Oxygen Balance Method.

An alternative gas analysis approach to current efficiency determination was discussed by Fellner *et al.* [19], who described the production of aluminium by the following reaction:

$$Al_2O_3 + xC \rightarrow 2Al + (3-x)CO_2 + (2x-3)CO \tag{2.28}$$

20

and stated that the current efficiency could be determined from the amount of oxygen evolved bound in CO_2 and CO. According to the authors, it is not necessary to know the reaction mechanism, or to what extent side reactions occur, provided the total amount of gas is determined. However, metal losses due to carbide formation or penetration into the crucible are only partly accounted for by this method.

This pseudo-oxygen balance can be extended to utilise Faraday's law in a manner similar to the traditional metal production measurements. If the main reaction *2.1* is considered as two half reactions, then aluminium metal is deposited at the cathode:

$$Al_2O_{3(dissolved)} + 6e^- = 2Al_{(l)} + 3O^{2-} \tag{2.29}$$

and the sacrificial carbon is oxidised at the anode:

$$3xC_{(s,anode)} + 3O^{2-} = 3C_xO_{(g)} + 6e^- \tag{2.30}$$

Thus the oxygen liberated at the anode is not bound in any particular form. If a mass balance of oxygen can determine the net production of oxygen by the cell, then this can be compared to the theoretical oxygen according to Faraday's law, giving the current efficiency.

Figure 2.7 shows some of the mass balance considerations for a cell. The mass balance must include all sources of oxygen into and out of the cell. This is why the method used by Fellner *et al*. [19] is termed a pseudo-oxygen balance, as only the oxygen from CO and CO_2 was considered. For a true oxygen balance all the other sources of oxygen must be accounted for, however minor.
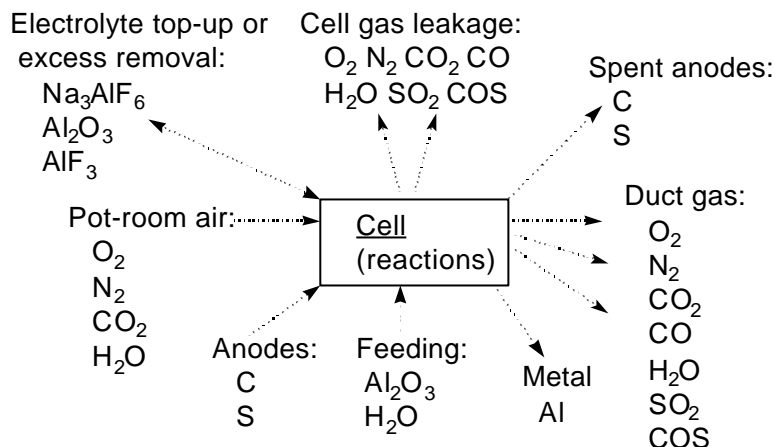
Figure 2.7 *Mass balance considerations around a cell.*

With an industrial cell the largest source of oxygen is that in the pot-room air drafted through the cell into the duct. The anode gases added to this will be low in concentration, as the drafting air flow rate is much larger than the rate of anodic gas evacuation. Any product gas leaving the cell other than in the duct (through hooding inefficiency or open doors and/or hoods) must be accounted for, as must water vapour introduced with the feed alumina. The moisture content of pot-room air must be accurately measured as it can vary over a short time period due to weather conditions such as intermittent rain [20]. The carbon dioxide and carbon monoxide content in pot-room air may also vary as a result of cell gases leaking out into the potroom. The CO_2 and CO concentrations in the pot-room air are also likely to be higher than the atmospheric average.

The oxygen balance eliminates the problems of all the other anode reactions masking the true current efficiency, as happens with the Pearson-Waddington equation and the pseudo-oxygen balance. If the net cell oxygen and cell current can be measured then the current efficiency can be determined irrespective of the reactions occurring in the cell. The focus then shifts from determining the reactions occurring to accurately measuring the gases produced in the cell, as the accuracy of current efficiency determination is directly dependent on this. Rapid and accurate mass spectrometric gas analysis and an oxygen balance are the basis of the current efficiency method used in this thesis. The development of the method and its advantages and disadvantages are given in chapters 3 and 5.

2.5.   Factors Influencing Current Efficiency.

The numerous studies of current efficiency can be classified into three main types, and within each a variety of methods have been used:

- current efficiency modelling,
- measurements on laboratory cells,
- measurements on industrial cells.

Virtually all of the process variables in a cell, such as temperature, alumina concentration, electrolyte composition, anode-cathode spacing and current density, affect the current efficiency. The findings of some of the studies into the effects of these variables are reviewed. In some cases there is good agreement about the conditions required for maximum current efficiency, while in other cases the findings differ.

2.5.1.   Operating Temperature.

In practice cells are normally operated at a temperature 10-15°C above the melting point of the electrolyte, this difference being referred to as "superheat". Superheat is maintained to ensure adequate dissolution of alumina and minimise the formation of undissolved alumina sludge on the cathode. The energy to maintain the cell temperature comes from the ohmic heat generated in the electrolyte between anode and cathode, and also from the back reaction *2.14* which is exothermic. Additives to the electrolyte lower the melting point, allowing better control of the cell temperature for more accurate heat balancing.

The regular process interruptions to the cell such as alumina feeding, anode replacement and setting, anode-cathode spacing alteration, metal tapping and anode effects mean that the temperature may vary considerably. Table 2.2 summarises the findings of several studies on the effect of cell temperature on current efficiency.

Table 2.2 Current Efficiency Dependence on Temperature.

Author		Ref.	$\dfrac{\Delta(CE)}{\Delta T}$ (%/°C)	Comments
Fellner *et al*.	(1969)	19	-0.10 to -0.12	Lab. Cell, gas analysis by chromatography.
Castellano *et al*.	(1979)	21	negative	Lab. Cell, gas analysis by chromatography and absorption.
Lillebuen *et al*.	(1980)	22	-0.06 to -0.11	Back reaction rate calculation
			-0.183 to -0.304	Söderberg cell, gas analysis, P-W equation.
Fellner *et al*.	(1984)	23	-0.075 to -0.35	Lab. cell, gas analysis by chromatography and CO_2 absorption, P-W equation.
Grjotheim *et al*.	(1987)	24	-0.12	Lab. cell, gas chromatography, P-W equation.
Leroy *et al*.	(1987)	25	-0.2 to -0.3	280kA prebaked cell, gas analysis by mass spectrometry, oxygen balance.
Alcorn *et al*.	(1988)	26	-0.174	HS Söderberg cell, gas chromatography, modified P-W equation.
			-0.23	VS Söderberg cell.
			-0.26	Prebake cell.
Dewing	(1991)	27	-0.26	Industrial cells, gas analysis, P-W equation.
Stevens *et al*.	(1992)	28	-0.29	Industrial prebaked cells, radioisotope dilution technique
Paulsen *et al*.	(1993)	29	-0.2 ±0.1	175kA prebake cells, gas analysis by IR spectrophotometer, P-W equation.
Solli *et al*.	(1994)	30	-0.06 to -0.16	Lab. cell, weight gain of metal pad.

All of these studies report a decrease in current efficiency with increasing temperature, and the level of dependence is similar. The trend is discussed by Kvande [31], and further papers were reviewed [32] which covered a range of industrial cells, all with similar findings to those above. Grjotheim *et al*. [33] reviewed several earlier studies on laboratory cells, of which all but one reported temperature having a negative effect on current efficiency. The generally accepted explanation for this behaviour is the effect of temperature on the back reaction between carbon dioxide and aluminium. At constant cell current the rate of the main reaction forming aluminium is not influenced by temperature. However as the solubility of aluminium in

the electrolyte increases with temperature, as shown in Figure 2.8, so does the rate of back reaction. Therefore the ratio of forward to back reactions increases with temperature, lowering the current efficiency.
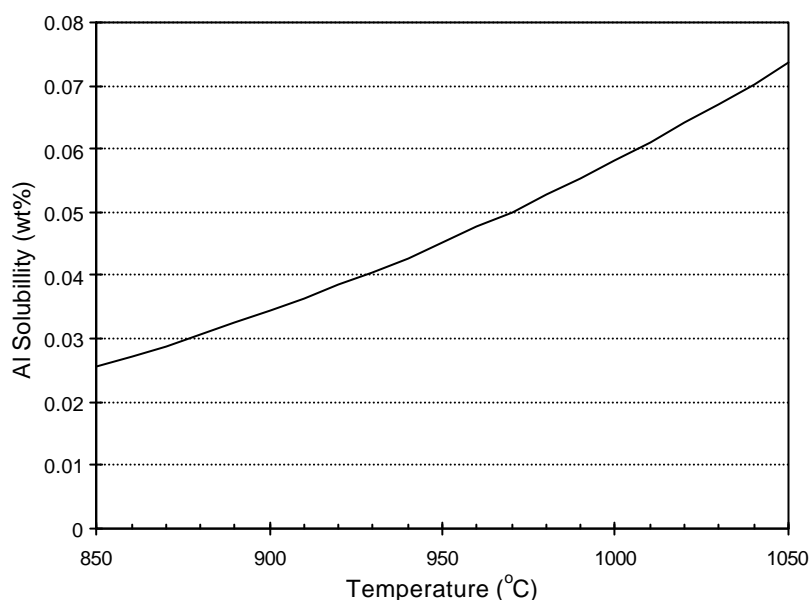
Figure 2.8 *Effect of temperature on Al solubility for a Na_3AlF_6-4wt%Al_2O_3-5wt%CaF_2-9wt%AlF_3 electrolyte.*

2.5.2.   Alumina Concentration.

The ideal situation for feeding alumina would be continuous and at the same rate as the electrolytic reduction. Many improvements to alumina feeding have been made over time, with modern technology allowing frequent (<5 minutes) point feeding of small amounts (<5kg). In the older technology cells are fed at intervals greater than 30 minutes apart. Because of the intermittent nature of alumina feeding, its concentration in the electrolyte varies, with the aim being to keep within certain bounds. At high concentrations, saturation is reached and undissolved alumina settles as sludge on the cathode. At low alumina content, the onset of anode effect can occur. A disadvantage of electrolyte additives (discussed in section 2.5.3) is that they all decrease the alumina solubility, making the operating window for alumina concentration smaller and placing more emphasis on feeding strategy and control.

Because of the variation in alumina concentration caused by the process dynamics, there have been numerous studies to determine the alumina level for optimum cell performance.

Several earlier studies on industrial cells are reviewed by Grjotheim *et al*. [34], with inconsistent results. Several studies showed current efficiency increased when alumina was added, and there were also many findings of a current efficiency minimum, at 5-6 wt% Al_2O_3, 5 wt% , 7 wt% and 10 wt%. Two results showed current efficiency decreasing with increasing alumina content, one showed no effect of alumina and another showed a current efficiency maximum. More recent studies, summarised in Table 2.3, are similarly inconsistent.

Table 2.3 Influence of alumina concentration on current efficiency.

Author	Ref	$\dfrac{\Delta(CE)}{\Delta[Al_2O_3]}$ (%/wt%)	Comments
Grjotheim *et al*. (1972)	35	minimum at 3-7wt% Al_2O_3	Lab. cell, gas analysis by chromatography and adsorption, P-W equation.
Poole and Etheridge (1977)	36	3 (2-4 wt% Al_2O_3) 1 (4-6 wt% Al_2O_3)	130 kA cells, Orsat anode gas analysis, P-W equation, 84-94 %CE.
Lillebuen *et al*. (1980)	22	0.8 0.05 to 0.567	Back reaction rate calculation. Söderberg cell, gas analysis, P-W equation.
Lillebuen and Mellerud (1985)	37	minimum at 4wt% Al_2O_3	Mathematical model of back reaction using physical-chemical electrolyte data.
Leroy *et al*. (1987)	25	-2 (1.2-3.5 wt% Al_2O_3)	280kA prebaked cell, gas analysis by mass spectrometry, oxygen balance.
Alcorn *et al*. (1988)	26	0.42 (2-4 wt% Al_2O_3)	HS Söderberg cell, gas chromatography, modified P-W equation.
		0.64 (2-4 wt% Al_2O_3)	VS Söderberg cell.
		0.25 (2-3 wt% Al_2O_3)	Prebaked cell with centre bar breaker.
		0.19 (2-5 wt% Al_2O_3)	Prebaked cell with point feeders.
		0.375 (2-5 wt% Al_2O_3)	Overall average value, corrected for the effect of temperature.
Stevens *et al*. (1992)	28	-1.3 (with low statistical significance)	Industrial prebaked cells, radioisotope dilution technique.

Paulsen *et al.* (1993)	29	0.7±0.2 (1.5-6 wt% Al_2O_3)	175kA prebake cells, gas analysis by IR spectrophotometer, P-W equation.
Solli *et al.* (1994)	30	0.0±0.2 (1.2-8 wt% Al_2O_3)	Lab. cell, CE by weight gain of metal pad.
		No influence	Mathematical model.

Grjotheim *et al.* [35] used a modified P-W equation with gas samples taken at five minute intervals. The current efficiency was measured after 45 minute start-up periods, but the time period used to determine the average efficiency was not shown, neither was the change in alumina concentration during each experiment. The plot of current efficiency *vs* alumina concentration is reproduced in Figure 2.9, demonstrating the trends found with differing experimental conditions.
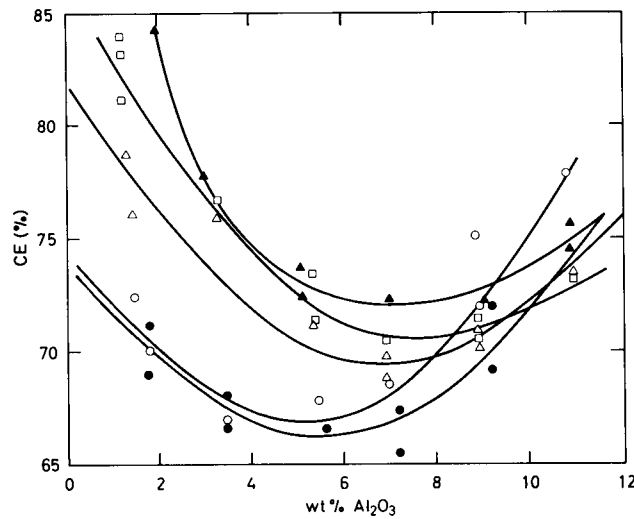
Figure 2.9 *Current efficiency vs alumina concentration, from Grjotheim et al. [35].*

The current efficiency showed a clear minimum, which was shifted to higher alumina contents by the addition of CaF_2. No explanation was given for the shape of the current efficiency curves, only the suggestion that it be somehow related to kinetic effects such as viscosity and surface tension. The current efficiency minima are around 6-7 wt% Al_2O_3, with the curves extending up to nearly 12 wt%. While the electrolyte compositions used in some smelters allowed high alumina contents in the past, modern electrolytes mean the alumina range is restricted to the lower end of the scale. Considering the findings of Grjotheim *et al.* [35] and

27

the earlier researchers [34], the left hand side of the current efficiency minimum curves show a strong negative effect of alumina concentration.

Poole and Etheridge [36] found a definite increase in current efficiency with alumina concentration, and recommended the alumina concentration to be kept high, in the 6-7wt% range. They concluded that there must be a fundamental relationship between current efficiency and alumina content, although no explanation was given.

Lillebuen *et al*. [22] modelled the current efficiency and found a strong positive effect of alumina concentration, although commented that several steps in the modelling contained considerable uncertainty. They discussed the solubilities of metal and gas, with a small increase in the concentration of dissolved aluminium giving a large increase in the dissolution rate of carbon dioxide. This was used as the basis for assuming the dissolution of metal from the cathode is the rate determining step in the back reaction, disregarding metal dispersion in the electrolyte. The current efficiency values determined from industrial cells by gas chromatography using the P-W equation were 2-3% lower than the actual values by metal production. This difference was attributed to the effect of the Boudouard reaction on the gas composition. Only two experimental runs were reported, where current efficiency was averaged over each 0.5 wt% Al_2O_3 range. A definite positive trend was shown by the first run, but the second showed almost no influence, with a coefficient of only 0.05%CE/wt%Al_2O_3.

Lillebuen and Mellerud [37] used the same modelling approach as Lillebuen *et al*. [22] and introduced more recent physical data that included metal and gas solubilities, gas bubble sizes and electrolyte properties. They calculated the dissolved metal concentration to be significantly lower than the metal solubility, and it increased as the alumina concentration decreased. They found a current efficiency minimum around 4 wt% Al_2O_3, shown in Figure 2.10.
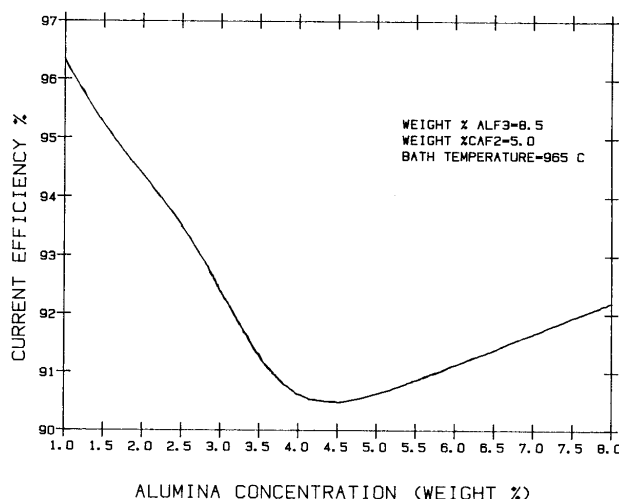
Figure 2.10 *Current Efficiency vs Alumina Concentration [37].*

One explanation for the current efficiency minimum was given by the authors in terms of gas bubble size. The metal solubility increases as the alumina concentration decreases as shown in Figure 2.18, so the current efficiency would be expected to decrease in a corresponding manner. However, as the alumina concentration decreases the bubble size increases, reducing the gas-electrolyte interfacial area to such an extent that the back reaction rate is reduced and the current efficiency increases. The gas bubble retention time under the anodes and bubble coalescence are important factors, with the current efficiency minimum shifted to lower alumina concentrations when the retention time is longer.

Leroy and Pelekis [25] measured the current efficiency on 280kA prebaked anode cells using mass spectrometric gas analysis and the oxygen balance method. They reported a current efficiency decrease of 2% with each wt% increase in alumina, which was determined by changing the feed to cells. Figure 2.11 shows the result of rapidly decreasing the alumina content in the electrolyte, and Figure 2.12 shows the variations in current efficiency with alternating underfeeding and overfeeding. From these figures it is quite clear that there was an immediate response, with current efficiency increasing as the alumina was decreased and vice versa over each short time interval. As these findings directly contradicted those of many other researchers, the authors discussed the difference with reference to the Boudouard reaction.

29
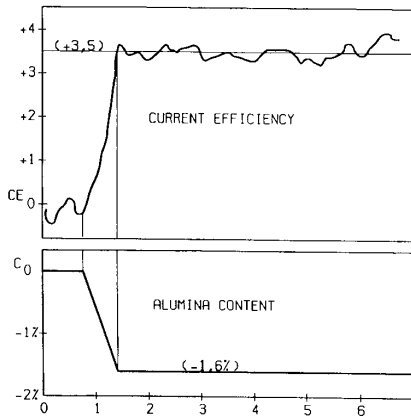
Figure 2.11 *Current efficiency with a rapid decrease in alumina content [25].*
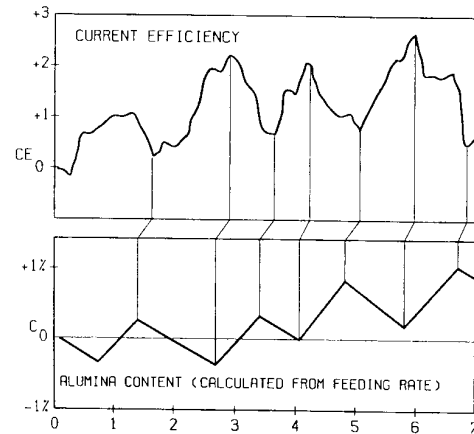
Figure 2.12 *Current efficiency variations with under- and over- feeding of alumina [25].*

They proposed that when the alumina concentration decreases, the contact surface between the anode gas bubbles and the anode underside increases. This allows increased interdiffusion between CO_2 in the anode gas bubbles and the CO produced by the Boudouard reaction in the anode pores. Thus as anode effect is approached the CO content of the product gas will increase. If the P-W equation is used this will translate to a decrease in efficiency, whereas the actual efficiency by the oxygen balance may be different. However no data on the amounts of CO and CO_2 detected was given, and if Figure 2.12 is examined there appears to be a long term trend of increasing current efficiency with increasing alumina content. Thus the current efficiency - alumina concentration relationship is not as simple as the authors suggest, indicating there may be other factors involved. The temperature variations of the cell during alumina feeding were not reported, therefore it is unclear what effect temperature had on the reported current efficiency trends, bringing doubt into the validity of the findings.

Alcorn *et al*. [26] used gas chromatography and a modified P-W equation to measure the current efficiency on industrial horizontal stud and vertical stud Söderberg and prebaked cells. The results for prebaked cells are shown in Figure 2.13, and for Söderberg cells in Figure 2.14. The electrolyte temperature is shown because it increases as the alumina content decreases after each break and feed. The correlations between alumina concentration and current efficiency were corrected for the temperature effect, and in each case the current efficiency increased as the alumina concentration increased.

30

PREBAKE CELL WITH BREAKER BAR PROCESS STUDY

Figure 2.13 *Current efficiency of prebaked cells [26].*

H.S. SODERBERG CELL PROCESS STUDY

V.S. SODERBERG CELL PROCESS STUDY
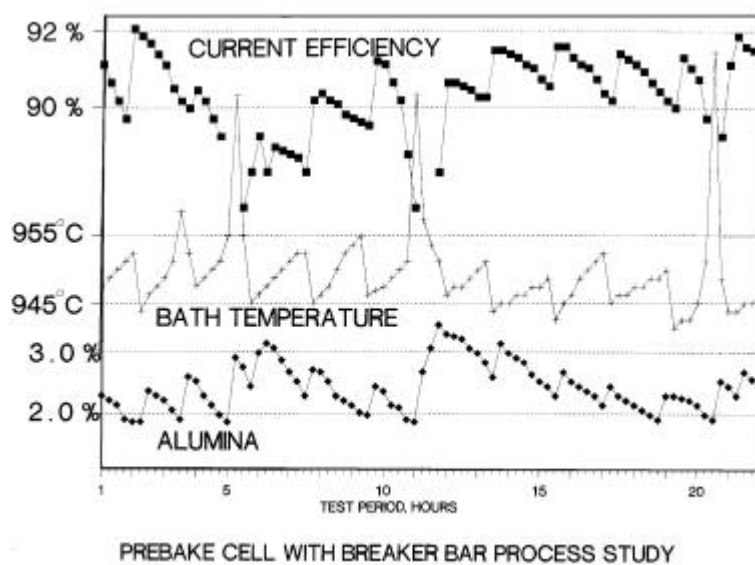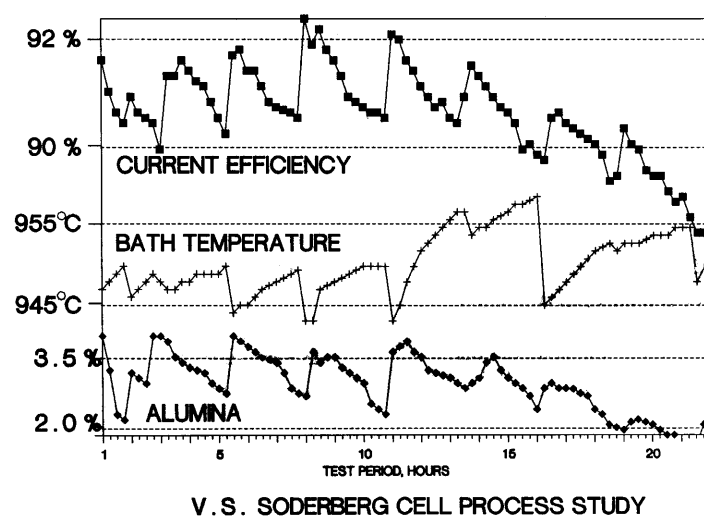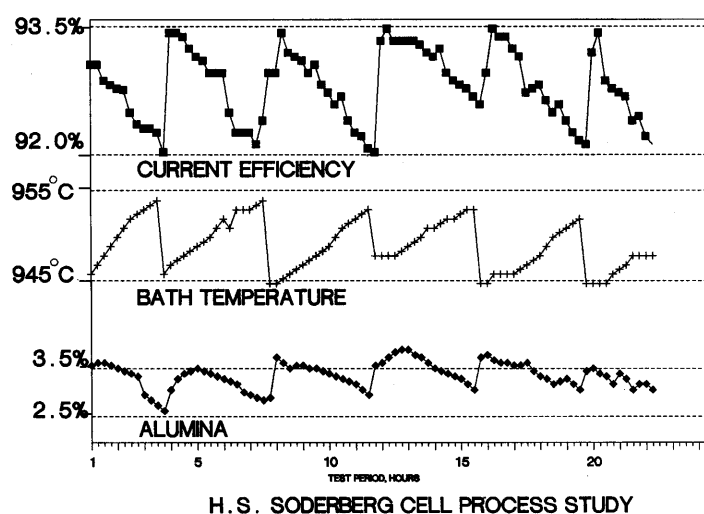
Figure 2.14 *Current efficiency of Söderberg cells [26].*

31

The Boudouard reaction and its effect on the current efficiency values was also discussed. The gas samples were taken through steel pipes through the anodes. When a pipe became partially blocked by frozen electrolyte, then the Boudouard reaction became large and a reduction the current efficiency was noted. However, this is an incorrect assumption introduced by using the P-W equation, because the Boudouard reaction does not affect the current efficiency, only the CO/CO_2 ratio in the product gas.

Stevens *et al*. [28] reported a negative effect of alumina concentration on current efficiency using the radioisotope dilution technique. The correlation has low statistical significance as the electrolyte was only sampled every four hours. The feeding cycle had a frequency of about 30 minutes, so the average alumina concentration was not adequately determined.

Paulsen *et al*. [29] determined the current efficiency on 175kA prebaked anode cells using an IR spectrophotometer and the P-W equation. They made measurements with the alumina concentration both increasing and decreasing, achieved by altering the feeding frequency so the feed rate was above and below the theoretical alumina consumption rate. In some experiments the temperature was allowed to vary, while in others it was kept constant by adjusting the anode-cathode distance. The results are presented in Figure 2.16 and Figure 2.15.
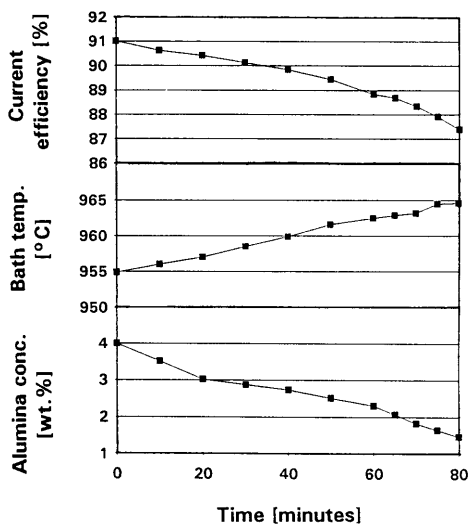
Figure 2.16 *Current efficiency with decreasing alumina, temperature allowed to vary [29].*
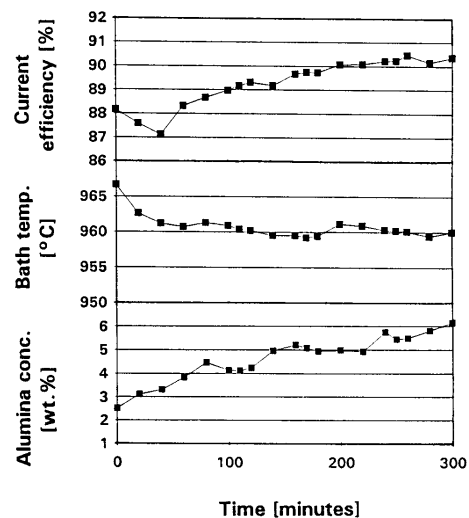
Figure 2.15 *Current efficiency with increasing alumina, temperature kept constant [29].*

The gas samples in this study were also taken through steel pipes through the anodes. The current efficiency values by the gas analysis method were 2 to 5% lower than the values based on the amount of metal tapped, the difference attributed to the Boudouard reaction between anode carbon dust and CO_2. The current efficiency also varied by up to 3% with different anode positions, which was explained by variations in the mass transfer rates and different rates of Boudouard reaction. The findings here were in close agreement with those of Alcorn *et al*. [26], who recommended that gas samples be taken from every anode rather than selected anodes.

Solli *et al*. [30] used a laboratory scale cell to study current efficiency, determined by the weight gain of the cathodic metal pad. The cell was designed to attain good convective conditions and a flat aluminium cathode surface for even current density distribution. Both the experimental measurements and the model indicated no influence of alumina concentration on current efficiency. The authors suggested that this was due to the very slight dependence of the equilibrium activity of dissolved metal on the alumina concentration. Previous alumina concentration - current efficiency correlations were discussed, along with the possibility of the erroneous use of the P-W equation in some of them because of the CO produced by the Boudouard reaction.

Grjotheim *et al*. [38] discussed the loss of current efficiency at higher (above $\approx$6wt%) and lower (below $\approx$3wt%) alumina concentrations. At high alumina levels they propose the loss of current efficiency is controlled by the metal dissolution, because the metal solubility is lower. At low alumina levels the loss of efficiency is controlled by gas dissolution because of the reduced gas bubble surface area. They showed the bubble surface area decreased markedly at around 4 wt% Al_2O_3. Various models were discussed, with most data indicating a metal solubility decrease and bubble surface area increase with increasing alumina concentration. However the overall findings of the models depend on the treatment of the bubble size effect and the metal solubility data used.

Langon and Peyneau [39] supported the negative effect of alumina on current efficiency found by Leroy *et al*. [25], and reported current efficiencies for industrial cells with the alumina concentration maintained at low levels. They described lowering the alumina concentration as

having two effects on the reoxidation mechanism, being decreasing the solubility of CO_2 and decreasing the total bubble surface area which accentuates the first effect also.

Kvande [32] reviewed several papers and made an interesting observation about the contradicting alumina concentration-current efficiency findings. While there are more reports of a positive effect of alumina, the indications are that the effect is only small. The strong negative effect of alumina found by Leroy *et al*. [25] led to cells being operated at low alumina levels. These cells have given very high current efficiencies on a long term basis, although this could be due to the stable cell control, low sludge formation and controlled anode effect frequency of these cells.

The mathematical models show conflicting findings, and it is difficult to evaluate which of the assumptions made best represent the processes inside a cell. Lillebuen *et al*. [22] showed a strong positive influence of alumina concentration, yet when Lillebuen and Mellerud [37] reworked the model with updated physical data they reported a current efficiency minimum. Solli *et al*. [30] showed no influence of alumina concentration.

Only two of the studies reviewed showed a negative influence of alumina concentration on current efficiency. The findings of Stevens *et al*. [28] must be disregarded because of the statistical insignificance, while those of Leroy *et al*. [25] are questionable because of the uncertainty of how the temperature effect was accounted for, and also because of the apparent long term positive influence of alumina concentration on top of the short term negative effect.

The minima found by Grjotheim *et al*. [35] could be interpreted as a negative effect of alumina concentration on current efficiency below 6-7 wt% Al_2O_3, and a positive effect of alumina concentration above this. However the industrial cell studies of Poole and Etheridge [36], Alcorn *et al*. [26] and Paulsen *et al*. [29] contradict this as all found a positive effect of alumina concentration on current efficiency over alumina concentration ranges below 6 wt%. All of these studies used the P-W equation with various gas analysis techniques, and the uncertainty introduced by this draws some doubt on the validity of the findings.

The laboratory study of Solli *et al*. [30] has a very sound experimental technique. While gas analysis was not used and short term changes in current efficiency with alumina concentration

could not be reported, constant alumina concentration was maintained for 4 hour duration experiments. This allowed current efficiency to be determined with a low standard deviation by the weight gain of the metal pad, avoiding the shortcomings of the studies that used the P-W equation. The alumina concentration range was 1.2-8 wt%, which is wide enough to eliminate the possibility of a current efficiency minimum. Although there are contradictions between the different current efficiency models, the model in this study gave results directly supporting the experimental finding of no influence of alumina concentration on current efficiency.

2.5.3. Additives to the Electrolyte.

Aluminium fluoride, calcium fluoride, and sometimes magnesium fluoride and lithium fluoride are the common electrolyte additives. Their role is to lower the melting point of the electrolyte as shown in Figure 2.17, allowing a lower operating temperature which results in lower metal solubility and therefore an expected increase in current efficiency.
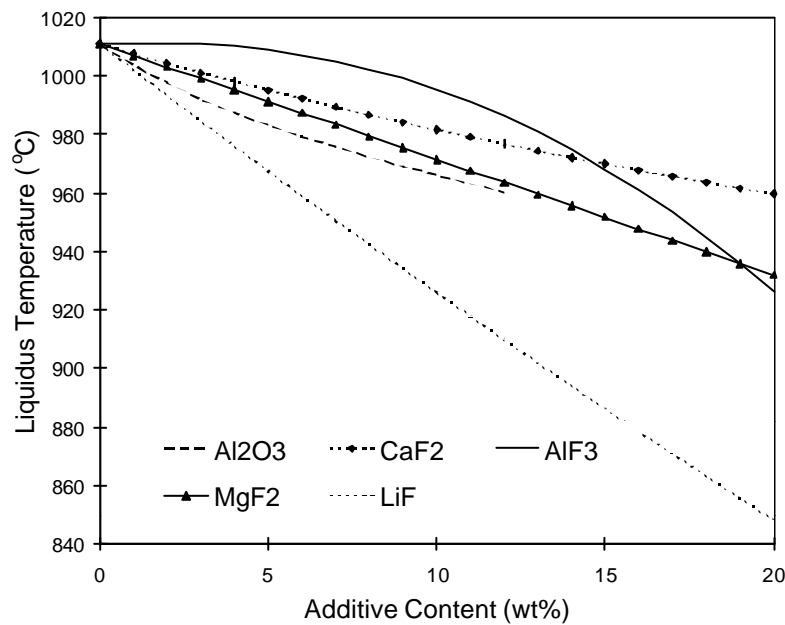
Figure 2.17 *Electrolyte liquidus temperature as a function of additives [40].*

In addition, the presence of the additives themselves lowers the metal solubility further, illustrated in Figure 2.18. The effect of additives on current efficiency cannot be included with temperature because of this dual effect.

35
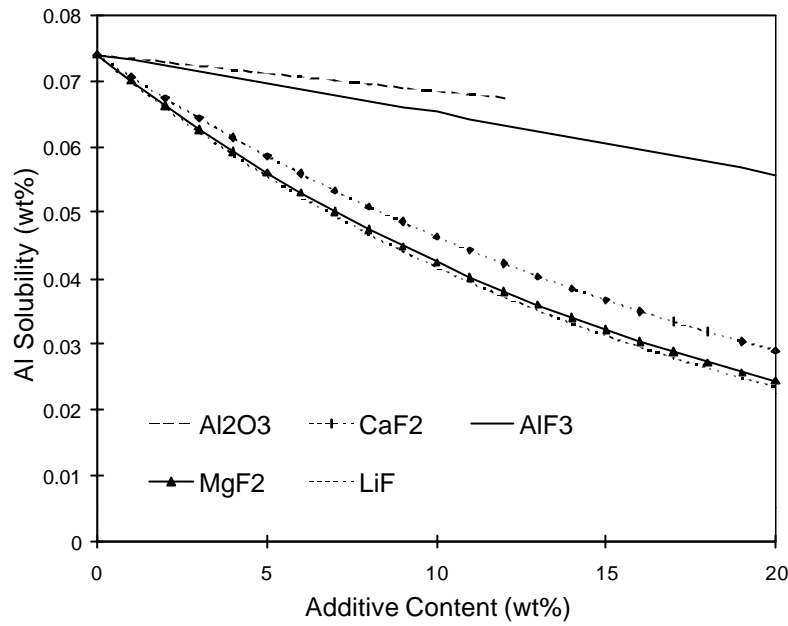
Figure 2.18 *Aluminium solubility in cryolite at 970°C as a function of additives [41].*

Another correlation which gives similar values of metal solubility and includes both temperature and additive content was given by Yoshida and Dewing [42]:

$$Al_{(dissolved)}(wt\%) = \quad -0.288 + 0.0003t + 0.027(BR) - 0.0019[CaF_2]$$
$$-0.0036[LiF] - 0.0029[NaCl] \tag{2.31}$$

where t is the temperature in °C, BR is the electrolyte bath ratio and $[CaF_2]$, $[LiF]$ and $[NaCl]$ are the concentrations of the additives in wt%. The authors included the effect of NaCl, although this is not a common additive. The BR term is the most significant in this correlation. As the BR decreases dissolved aluminium decreases, thus the excess AlF_3 content is a significant factor in current efficiency, because the assumption is made that the back reaction of dissolved Al is the major current efficiency decreasing factor.

Other reasons for using additives include to decrease the vapour pressure and hence vapour losses of the electrolyte, and to increase the electrical conductivity of the electrolyte, improving the energy efficiency [2].

Aluminium Fluoride.

Aluminium fluoride is typically the largest volume additive to the electrolyte in modern smelting cells. Welch [43] outlined some of the reasons behind changes in electrolyte composition as cell technology developed. As alumina feeding became more mechanised the limitations imposed by alumina solubility were relaxed. This allowed higher excess AlF_3 contents, giving lower electrolyte temperatures and higher purity aluminium. Impurities (M) are introduced by the fluoride salts (MF) in the electrolyte by undergoing partial reduction according to reaction *2.32*:

$$3MF_{(electrolyte)} + Al \rightarrow 3M_{(in\ Al)} + AlF_{3(electrolyte)} \tag{2.32}$$

Even the most stable fluorides can introduce impurities above acceptable quality levels. Any further reduction in liquidus temperature or other desired changes to the electrolyte properties without increasing the impurity can be achieved by increasing the aluminium fluoride content.

Some of the studies of the influence of aluminium fluoride on current efficiency are summarised in Table 2.4. For consistency, cryolite ratio is the term used to represent the AlF_3 content of the electrolyte.

Table 2.4 Effect of cryolite ratio on current efficiency.

Author	Ref.	$\dfrac{\Delta(CE)}{\Delta(CR)}$ (%/unit ratio)	Comments
Lewis (1967)	44	-8.25	10kA test cell, CR 2.6 and 3, CE 85-90%.
Fellner *et al*. (1969)	19	negative	Lab. cell, gas analysis by chromatography.
Burck and Fern (1971)	45	-8	47kA cells, CR 2.3 to 2.7, CE 85-88%.
Grjotheim *et al*. (1972)	35	negative	Lab. cell, gas analysis by chromatography and adsorption, P-W equation
Dewing (1991)	27	-8.2 at 86%CE -5.6 at 90%CE -4.7 at 92%CE	Industrial cells, gas analysis, P-W equation.

Stevens *et al.* (1992)	28	-23.7 (1.66%/wt% xsAlF$_3$)	Industrial prebaked cells, radioisotope dilution technique
Solli *et al.* (1994)	30	-4.2 at 980°C -5.2 at CR=3, 90%CE -7.1 at CR=2 to 2.5, CE 96 to 93%	Lab. cell, CE by weight gain of metal pad.
Dorin *et al.* (1994)	46	-11 CR = 3 to 2.2, CE 85-95%	Lab. cell, CE by weight gain of metal pad.
Welch (1997)	43	negative	Long-term smelter data, increased efficiency with increased xsAlF$_3$.

Kvande [31,32] also reviewed several papers, which all showed similar results. The trend of increasing current efficiency with increasing excess aluminium fluoride content is undisputed, and is generally attributed to the decreased solubility of aluminium in lower ratio electrolytes. The magnitude of the relationship varies, although this is likely to be due to the large variation of conditions used in the studies, especially between industrial and laboratory cells.

Lithium Fluoride.

Lithium fluoride has the largest freezing point depression, and along with lithium cryolite has been used in many electrolytes to study cell performance at low temperatures [19,23,24,27,44,47]. The true effect of LiF on current efficiency is not clear as any trend may be masked by the effects of the lower temperature or other changes to the electrolyte composition, however some findings show little or no influence [32,47]. Other results show current efficiency decreasing with LiF content [31], while Grjotheim *et al.* [35] reported an increasing efficiency with LiF additions. As well as lowering the temperature, the other main advantage behind the use of LiF is the increase in electrolyte conductivity [44].

Calcium Fluoride.

Calcium fluoride has been reported on with conflicting results, summarised in Table 2.5. It appears that in laboratory studies there was a definite positive effect of calcium fluoride on current efficiency, whereas in industrial cells there was no measurable influence. Solli [30] suggested that in the industrial cell studies only a narrow range of calcium fluoride

concentrations were considered, and the expected slight positive effect may in practice be difficult to detect.

Table 2.5 Influence of calcium fluoride on current efficiency.

Author		Ref.	$\dfrac{\Delta(CE)}{\Delta[CaF_2]}$ (%/wt%)	Comments
Fellner *et al.*	(1969)	19	positive (0.73)	Lab. cell, gas analysis by chromatography.
Grjotheim *et al.*	(1972)	35	positive	Lab. cell, gas analysis by chromatography and adsorption, P-W equation
Dewing	(1991)	27	no influence	Industrial cells, gas analysis, P-W equation.
Stevens *et al.*	(1992)	28	no influence	Industrial prebaked cells, radioisotope dilution technique
Paulsen *et al.*	(1993)	29	no influence (-0.6 to +0.3)	175kA prebake cells, gas analysis by IR spectrophotometer, P-W equation.
Solli *et al.*	(1994)	30	positive	Lab. cell, weight gain of metal pad.

Magnesium Fluoride.

Magnesium fluoride is rarely used in electrolytes, and there is a correspondingly smaller number of studies on its influences. The results reported are in good agreement, with Fellner *et al.* [19] showing the current efficiency increasing by 0.97% per wt% MgF_2 for a laboratory cell. In a subsequent paper Fellner *et al.* [23] again reported the positive effect of magnesium fluoride on current efficiency in a laboratory cell, which was attributed to the changed physicochemical properties of the electrolyte, particularly the metal solubility. Stevens *et al.* [28] reported a coefficient of 4.8%CE per wt% MgF_2 for industrial prebaked cells. Grjotheim *et al.* [34] reviewed several earlier studies which all confirmed the addition of MgF_2 increasing current efficiency.

2.5.4. Current Density.

The effect of changing the current density is difficult to determine because of the associated changes in other variables of operation. If the cell current is increased the ohmic heat generation will be greater and will result in a melting back of the frozen side ledge, changing the

bath ratio and leading to a larger metal pad area. This can be compensated for by increasing the anode-cathode spacing, but then the effect of current density alone is difficult to isolate. Both Grjotheim *et al*. [33] and Grjotheim and Welch [15] describe the generally accepted view that current efficiency increases as current density increases provided the other variables remain constant. This is because the rate of metal reoxidation is independent of current density, whereas the rate of metal production is directly dependent on it. At higher current densities there is a greater stirring effect of the electrolyte from the greater bubble evolution, which would indicate a loss of efficiency, however this may only become apparent at very high current densities.

Grjotheim [48] presented results for a laboratory cell using Al-Cu cathodes. Gas analysis was by chromatography, and the current efficiency was calculated using the P-W equation. They showed a current efficiency maximum at about current density 1.6 A/cm^2. Below this the current efficiency decreased quite strongly with decreasing current density, agreeing with the general view. The drop in efficiency at the high current densities may be due to excessive electrolyte mixing, as the current densities are very high in comparison to those found industrially.

A slightly different picture was shown by Solli *et al*. [30], who found a small decrease in current efficiency as the current density dropped from 1.4 to 0.3 A/cm2, then a rapid drop in efficiency as the current density was decreased further. The same trend was found by both experimental measurements in a laboratory cell and by a current efficiency model. This shaped curve was similar to some of those reviewed by Grjotheim *et al*. [33].

2.5.5. Anode-Cathode Distance.

The anode cathode spacing or distance (ACD) is regularly adjusted in an industrial cell. As anodes are consumed the ACD increases, but this is reduced by periodically lowering the anodes to maintain a certain gap. From an energy point of view it is advantageous to lower the ACD, as it results in a significant reduction in the ohmic drop through the electrolyte. The influence of anode-cathode distance has been widely investigated with quite reproducible results. The general findings are that above a critical ACD there is little or no influence of

ACD on current efficiency. Below the critical ACD the current efficiency drops away. This was shown by the papers reviewed by Grjotheim *et al*. [33], by Fellner *et al*. [23] for a laboratory cell, Dorin and Frazer [49] for a laboratory cell with wettable cathodes, and by Fellner *et al*. [19] for a laboratory cell with low temperature electrolyte. The findings of Dorin and Frazer [49] are shown in Figure 2.19, indicating the nature of the rapid drop in efficiency below the critical ACD.
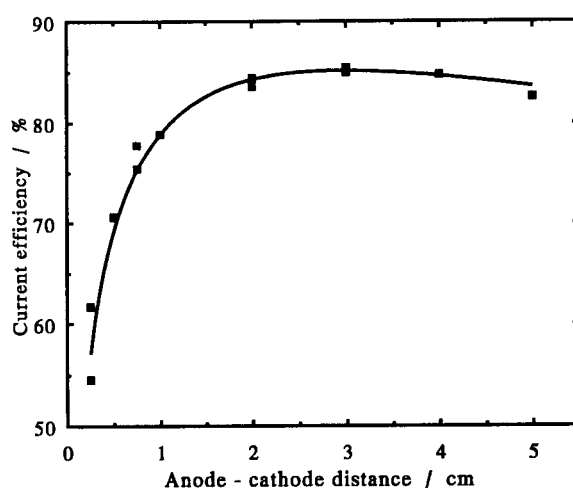
Figure 2.19 *Current efficiency with anode-cathode distance [49]*.

Grjotheim *et al*. [48] showed the current efficiency increasing slightly with ACD in laboratory cells with Al-Cu cathodes. Lillebuen *et al*. [22] showed a general decrease in current efficiency with decreasing ACD from a current efficiency -back reaction model. They gave no evidence of a critical ACD or a rapid drop off in efficiency. Solli *et al*. [30] showed no influence of ACD above the critical ACD. One data point, at the lowest ACD, was at a significantly lower current efficiency, and was defined as being below the critical ACD. It was highlighted that the critical ACD for a laboratory cell, as in this case, is more defined and smaller than for an industrial cell. This is because of the metal instability due to metal pad waves and the thicker anode gas bubbles present. Leroy *et al*. [25] and Alcorn *et al*. [26] showed very similar results for industrial cells. Leroy *et al*. showed the current efficiency decreasing by about 0.7% per millimetre of ACD decrease below a critical distance. Alcorn *et al*. showed a strong decrease in current efficiency below 1.5 inch ACD, and a nearly

constant current efficiency above 1.75 inch ACD. The findings of these two studies are shown in Figure 2.20. The curve generated by Alcorn is described by equation *2.33*.

$$CE\% = 95\left[1 - 4\exp(-3.772 \times ACD)\right] \tag{2.33}$$
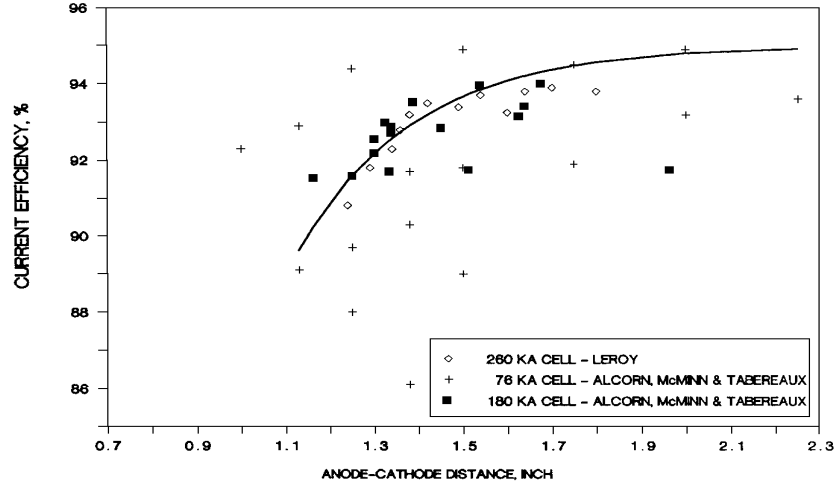
Figure 2.20 *Current efficiency with ACD, taken from Alcorn et al. [26].*

While reducing the ACD has energy advantages, it is limited by the loss in current efficiency and also by cell control implications at low ACD values.

2.6. Carbon Consumption.

In the main reaction producing aluminium *(2.1)*, the molar ratio of aluminium produced to carbon consumed is 4:3. Therefore the theoretical minimum carbon consumption per unit of aluminium is given by:

$$Carbon\ consumption = \frac{mw_C}{mw_{Al}}\frac{3}{4} = \frac{12.011}{26.9815} \times \frac{3}{4} = 0.3339\,kgC\,/\,kgAl \tag{2.34}$$

There are four mechanisms which increase the carbon consumption above this minimum. They are:

1. Electrolytic production of carbon monoxide as shown in reaction *2.17*,
2. Carbon dioxide burn of the anode carbon by the Boudouard reaction *2.24*,

42

3. Air burn of the exposed areas of the anode carbon by reactions *2.26* (and possibly to a very minor extent *2.27*),

4. Carbon dusting through erosion of the anode.

It has been shown [50] that the predominant reactions in the cell, being the main reaction *2.1*, electrolytic formation of CO, reaction *2.17*, and the main back reaction, *2.14*, can be combined as:

$$\frac{1}{2}Al_2O_{3(dissolved)} + \frac{3}{4x}(1+p)C_{(s,anode)} \rightarrow Al_{(l)} + \frac{3}{4x}(2x-p-1)CO_{2(g)} + \frac{3}{2x}(1+p-x)CO_{(g)}$$

(2.35)
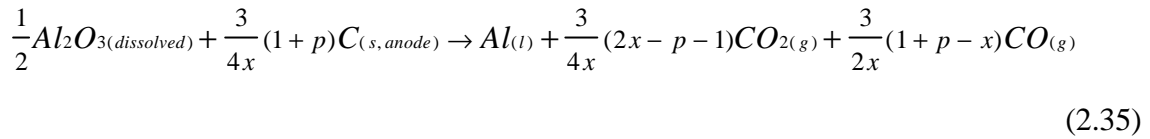
where x is the fractional current efficiency from reaction *2.16*, and p is the fraction of current carried by the electrolytic formation of CO according to reaction *2.17*. This allows equation *2.34* to be rewritten as:

$$Electrolytic\ carbon\ consumption = \frac{0.3339}{x}\left(1+p\right)$$

(2.36)

In other words, as the current efficiency drops and some of the current produces carbon monoxide directly, the carbon consumption increases from the minimum.

Carbon dusting occurs due to differential reactivity of the anode carbon. The anodes are made up of a mixture of grains of coke and recycled anodes butts, held together in a binder matrix of coked pitch and coke dust. Carbon dioxide and air predominantly attack the binder matrix, as seen in Figure 2.21.
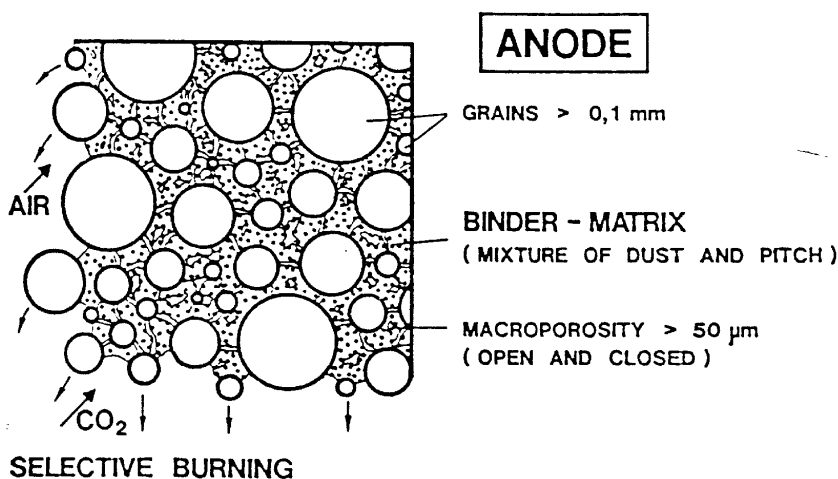
Figure 2.21 *Anode composition and burning, from Fischer and Perruchoud [18].*

As the binder matrix is eroded away the grains may become detached, usually collecting as carbon dust floating on the electrolyte surface. Once there the carbon may react with any air or with CO_2 as it emerges as bubbles from under the anodes.

The four main mechanisms of excess carbon consumption cause the actual consumption for modern industrial cells to be 0.4 to 0.5 kg C per kg Al. The contributions of these four mechanisms, as well as that of the main reaction, *2.1*, to the total carbon consumption, is shown in Table 2.6, from Grjotheim and Welch [51].

Table 2.6 The overall consumption of an anode.

Reaction	kg C per kg Al (88% CE)	kg C per kg Al (94% CE)
Electrolytic CO_2	0.374 - 0.372	0.353 - 0.350
Electrolytic CO	0.003 - 0.006	0.002 - 0.005
CO_2 burn (Boudouard)	0.015 - 0.030	0.014 - 0.028
Dusting	0.002 - 0.015	0.002 - 0.014
Air burn	0.030 - 0.080	0.028 - 0.075
Total	0.424 - 0.503	0.394 - 0.468

2.7.   Anode Effect.

The electrode potential required for the electrolytic production of carbon monoxide by reaction *2.17* is 1.06V. While this is thermodynamically preferred, in practice the anode polarisation discussed in section 2.2 raises the electrode potential above the 1.18V required for the main reaction *2.1*. Carbon monoxide formation becomes important in regions of low current density such as the sides of the anodes.

As electrolysis proceeds and the alumina concentration decreases, the anode polarisation increases. Once the alumina concentration decreases below a certain level, the concentration of oxygen containing ions decreases and there is a subsequent increase in the concentration of fluoride ions near the anode. As the anode polarisation increases beyond a certain level, the anode critical current density for discharge of only oxygen containing anions is exceeded, and eventually fluorine is discharged at the anode from the decomposition of cryolite [52]. Carbon tetrafluoride is evolved by reaction *2.37* at an electrode potential of 2.54V:

$$4\ Na_3AlF_6 + 3C = 12NaF + 4Al + 3CF_4 \qquad\qquad E° = -2.54V \quad (2.37)$$

and hexafluoroethane is evolved at 2.78V by reaction *2.38*:

$$2Na_3AlF_6 + 2C = 6NaF + 2Al + C_2F_6 \qquad\qquad E° = -2.78V \quad (2.38)$$

The presence of the non-wetting fluoride gas film on the anodes increases the cell resistance, and as the current arcs across the gas layer the cell voltage fluctuates wildly. The evolution of CF_4 and C_2F_6 and the associated disruption to the cell is known as "anode effect". Anode effect normally arises at alumina concentrations between 0.5 and 2.2 wt%, with values between 1 and 2 wt% being most common [53].

The occurrence of an anode effect is generally defined by a sudden increase in cell voltage, unstable conditions in the cell with oscillating voltage and current arcing, and evolution of CF_4 as well as the carbon oxides [51]. For this study the onset of anode effect was defined as the point in time when the cell voltage increased suddenly. The formation of perfluorocarbons at

the beginning of anode effect, and the changing cell voltage during this period, are discussed in chapter 8.

The exact mechanism at the onset of anode effect is the subject of debate. One possibility is the production of carbonyl fluoride by reaction *2.39* at an electrode potential of 1.86V:

$$2Na_3AlF_6 + Al_2O_3 + 3C = 3COF_2 + 6NaF + 4Al \qquad\qquad E° = -1.86V \quad (2.39)$$
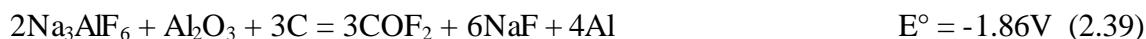
While COF_2 has not been positively identified in anode gas, an observed voltametric peak has been assigned to the formation of this compound [54,55,56]. If COF_2 is formed it can react with carbon giving CO and CF_4 by reaction *2.40*, which has an equilibrium constant K of 86.4 at 970°C.

$$2COF_2 + C = 2CO + CF_4 \qquad\qquad\qquad\qquad (2.40)$$

Therefore the formation and subsequent decomposition of COF_2 could be a precursor to anode effect by providing the initial CF_4 gas film. The difficulty in identifying this gas may be due to decomposition of COF_2 to C_2F_6 (reaction *2.41*), which has an equilibrium constant at 970°C of 1.17E-03.

$$3COF_2 + 2C = 3CO + C_2F_6 \qquad\qquad\qquad\qquad (2.41)$$

It may also decompose by hydrolysis to form HF and CO_2 [57,58]:

$$COF_2 + H_2O = CO_2 + 2HF \qquad\qquad\qquad\qquad (2.42)$$

The equilibrium constant for reaction *2.42* is 4.15E+08 at 970°C, which increases to 1.18E+16 at 25°C. According to Øygård *et al.* [59] COF_2 may also decompose into CO_2 and CF_4 by reaction *2.43*, however the equilibrium constant at 970°C is only 0.952, and Amphlett *et al.* [60] reported the reaction taking 1 day at 1200°C with a nickel/platinum catalyst.

$$2COF_2 = CO_2 + CF_4 \qquad\qquad\qquad\qquad (2.43)$$

The formation of CF_4 was recognised as early as 1926 [61], and quantification of the product gas composition during normal electrolysis and anode effect was made by Henry and Holliday [62,63]. They showed that CF_4 and C_2F_6 were only found in the product gas during anode effect, none was present during normal electrolysis, and the amount of C_2F_6 was very minor.

The awareness of the environmental effects of CF_4 and other perfluorocarbons has spawned a number of more recent studies on their emission from aluminium smelting cells [52, 64-68]. These studies have variously looked at Söderberg, prebake and laboratory cells. All confirm that under normal operating conditions CF_4 and C_2F_6 are only emitted during anode effect.

This was shown clearly by Tabereaux and co-workers [52,64], who sampled gas from pipes inserted into holes in individual anodes in prebaked cells and into wet paste in Söderberg cells. Gas analysis was made with a gas chromatograph and a gas chromatograph/mass spectrometer in single ion monitoring mode. The comparison of product gas compositions from periods of normal cell operating conditions and anode effects showed the following trends:

Normal conditions (prior to anode effect):

1. No PFCs (CF_4 or C_2F_6) were detected being emitted in product gases preceding the anode effects.

2. The average CO concentration was $17.9 \pm 6.7\%$ and CO_2 concentration was $68.6 \pm 2.6\%$.

During anode effects:

1. The average CF_4 concentration level was $8.8 \pm 1.4\%$.

2. The average C_2F_6 concentration level was $1.2 \pm 1.2\%$.

3. The average CO content increased to $56.0 \pm 7.1\%$ and CO_2 content decreased to $19.3 \pm 7.5\%$.

The change in product gas composition for an individual anode effect is shown in Figure 2.22. The anode effect was allowed to continue without termination. The upper plot shows the anode gas with a 100% scale, demonstrating the decrease in CO_2 and increase in CO at the start of anode effect. The lower plot shows an expanded anode gas composition range, demonstrating the rise in CF_4 concentration to a steady level, and the rise and subsequent fall in C_2F_6 concentration after only 3 minutes.
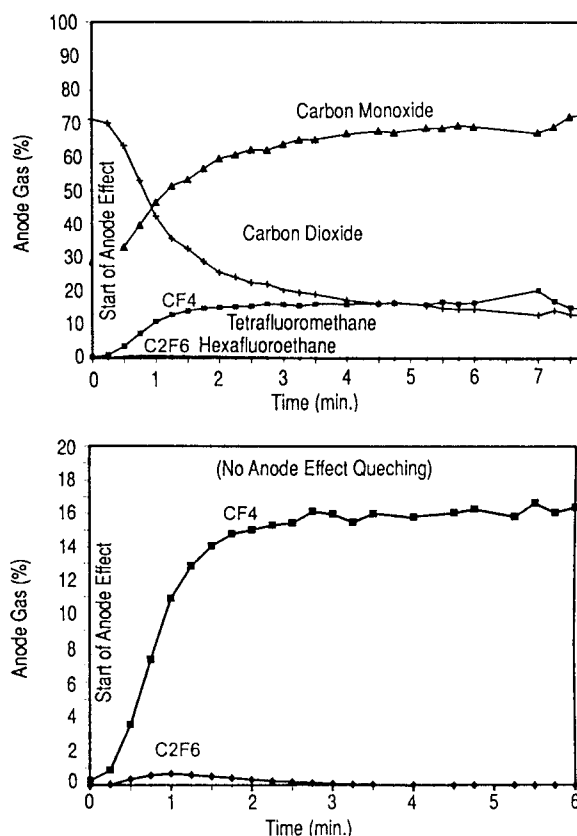
Figure 2.22 *Product gas composition changes during anode effect [52].*

Tabereaux [52] also investigated the effect of anode shorting on PFC generation during anode effect. Figure 2.23 shows the production of CF_4 and C_2F_6 during an anode effect as the anodes were raised and lowered until the anode effect was terminated. The generation of C_2F_6 was similar to that in Figure 2.22, with the maximum concentration reached after 1 minute, then the concentration falling quickly. The CF_4 concentration clearly decreased as the anodes were lowered, and increased as the anodes were raised. The author stated that if the cell voltage during anode effect remains almost constant at about 30-40V, then short circuiting does not occur indicating a stable resistive film barrier on anodes. When this is the case the generation of CF_4 is at a nearly constant rate. When the voltage fluctuates erratically (from 3 to 35V) the resistive film barrier is unstable and metal shorting to the anode occurs. Metal shorting was suggested as the reason why there are such differing CF_4 emissions from different anode effects, and in measurements made by different workers in other aluminium smelters.
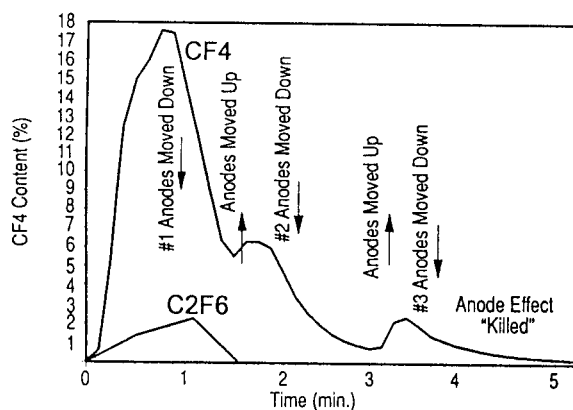
Figure 2.23 *PFC generation with metal shorting during anode effect [52].*

Similar results, if not quite as conclusive, were found by Berge *et al*. [65], who sampled duct gas from both Söderberg and prebaked cells, and used a photo acoustic gas monitor for the gas analysis. CF_4 evolution began immediately at the start of anode effect, when the cell voltage increased from the normal 4-5V to 10-40V. The CF_4 concentration peaked shortly after anode effect started, then decreased as the anode effect proceeded. When normal cell operation resumed the CF_4 concentration fell rapidly back towards zero. The relative amount of C_2F_6 to CF_4 for Söderberg cells was 5%, and for prebaked cells was 16%.

Roberts and Ramsey [66] characterised the emissions of CF_4 and C_2F_6 from the common exhaust duct of 40 cells in an industrial potline using a process mass spectrometer. The average emission rates were 0.2 kg CF_4/tonne Al and 0.02 kg C_2F_6/tonne Al, with very good statistical significance. Once again tests showed that perfluorocarbons were not produced during normal steady-state operation, only during anode effect.

Kimmerle *et al*. [67] analysed industrial cell exhaust duct gas samples with a tunable diode laser absorption spectrometer to determine the concentration of CF_4 and C_2F_6. Two sampling points covered groups of cells operating with newer and older control technology. This enabled comparison of specific PFC emissions between cells with variable anode effect frequencies. For the older control technology the emission rates were 0.54 kg CF_4/tonne Al and 0.053 kg C_2F_6/tonne Al, with the ratio of CF_4/C_2F_6 being 10.3. The emission rates for the cells with new control technology were significantly lower at 0.076 kgCF_4/tonne Al and 0.0085 kgC_2F_6/tonne Al, although the ratio of CF_4/C_2F_6 was similar at 8.9. The new cell control technology reduced the number of anode effects by a factor of 3.5 through more

49

frequent scanning of the cell voltage. The duration of anode effects was reduced by a factor of about 2.3 through faster corrective action once an anode effect was detected. The CF_4 emissions were reduced by a factor of 7 and C_2F_6 emissions by a factor of 6, a smaller reduction because C_2F_6 is only emitted in the early stages of an anode effect.

Nissen and Sadoway [68] studied the generation of PFC's in a laboratory scale cell. Gas from around the anode was collected under a boron nitride hood and flushed from the cell with argon or helium to an on-line gas chromatograph for analysis. The results showed the presence of a critical current density above which the cell voltage rose sharply and the cell went into anode effect. When the cell current was maintained during anode effect the PFC level was relatively stable. With a normal electrolyte composition PFC's were only emitted when the cell was on anode effect, however when a bath ratio of 0.56 was used CF_4 was measured at low levels at normal cell voltage *i.e.* in a cell not on anode effect. The measured PFC level varied linearly with current density, and PFC generation was continuous even at a current density as low as 0.25 A/cm^2. The generation of PFC's at normal cell voltage with the low ratio electrolyte was rationalised by the higher fluoride activity than in conventional electrolytes.

Some of the environmental considerations regarding CF_4 and C_2F_6 are discussed by Tabereaux [52] and Nissen and Sadoway [68]. These PFC's have been implicated in climate change due to their high global warming potential (GWP), which is a combined measure of their expected life in the atmosphere and their infrared absorbing capacity.

Table 2.7 Global warming potential of PFC's referenced to CO_2 [68].

Compound	Lifetime (years)	Global warming potential (referenced against CO_2)		
		Time horizon (years)		
		20	100	500
CO_2	200	1	1	1
CF_4	50,000	4,100	6,300	9,800
C_2F_6	10,000	8,200	12,500	19,100

According to Tabereaux [52] the atmospheric concentration of CO_2 is 350,000 parts per billion, while for CF_4 it is 0.07 ppb and for C_2F_6 it is 0.002 ppb. Thus CO_2 is by far the larger contributor to global warming, and although the global warming potentials of CF_4 and C_2F_6 are so much larger than that of CO_2, as seen in Table 2.7, their overall impact toward global warming is small. However, the primary aluminium industry is still a significant source of global warming gases, and efforts are being made to reduce PFC emissions. In the U.S., the Environmental Protection Agency has teamed up with a number of aluminium companies to form the Voluntary Aluminum Industrial Partnership (VAIP) Program. The VAIP is expected to reduce the annual U.S. PFC emissions from aluminium smelting by 45% from the 1990 level by the year 2000 [69].

2.8. Sulfur Containing Emissions.

The typical sulfur content in calcined coke is 0.25 to 5.0 wt% [70], and the sulfur content in modern anodes typically ranges from 2 to 4 wt%. The diminishing availability of low sulfur feedstocks and the higher sulfur content of petroleum coke from some of the newer oilfields mean that the anode sulfur content is increasing. While the presence of sulfur in anodes does not cause a serious problem to the electrochemical operation of cells, it is of major concern in fume collection and scrubbing and environmental pollution.

Grjotheim *et al*. [71] described reports that the sulfur in the anode carbon is in the form of thiophene, C_4H_4S, which can directly take part in the electrochemical reduction of alumina by several reactions, forming COS, SO_2 and SO_3.

If sulfur is considered chemically equivalent to carbon then the electrochemical formation of COS theoretically would occur at a potential below that for the formation of either CO or CO_2, according to reaction *2.44*:

$$Al_2O_3 + 3C + 3S = 3COS + 2Al \qquad\qquad E°(970°C) = -1.04V \quad (2.44)$$

If COS does not form by an electrochemical mechanism, then it can be formed chemically because of the strongly favoured chemical equilibria of reactions *2.45* and *2.46*:

$$S + CO_2 + C = COS + CO \qquad\qquad K(970°C) = 4.44E+02 \quad (2.45)$$

$$CO + S = COS \qquad\qquad K(970°C) = 4.57E+00 \quad (2.46)$$

Although carbon dioxide is in contact with the anode, the reaction of sulfur with CO_2 to form SO_2 and CO is not expected:

$$S + 2CO_2 = SO_2 + 2CO \qquad\qquad K(970°C) = 3.84E-03 \quad (2.47)$$

If SO_2 and SO_3 are formed electrochemically, they are likely to react with carbon, forming COS:

$$SO_2 + 2C = COS + CO \qquad\qquad K(970°C) = 8.98E+06 \quad (2.48)$$

$$SO_3 + 2C = COS + CO_2 \qquad\qquad K(970°C) = 1.06E+15 \quad (2.49)$$

According to Henry and Holliday [62], carbon disulfide may form from COS by reaction *2.50*, although the equilibrium constant is 0.237 at 970°C.

$$2COS = CO_2 + CS_2 \qquad\qquad K(970°C) = 2.37E-01 \quad (2.50)$$

Sulfur dioxide is another sulfurous compound that is likely to be formed, especially if COS reacts with oxygen according to reaction *2.51*:

$$COS + O_2 = SO_2 + CO \qquad\qquad\qquad (2.51)$$

The equilibrium constant at 970°C is 4.55E+11, which increases as the temperature drops. Therefore at the temperatures likely to be encountered when COS emerges from the electrolyte and crust, if oxygen is present the formation of SO_2 is strongly favoured. CS_2, formed by reaction *2.50*, is also likely to be similarly oxidised to SO_2 by reaction *2.52*, with an equilibrium constant of 4.16E+38 at 970°C, which increases as the temperature decreases.

$$CS_2 + 3O_2 = 2SO_2 + CO_2 \qquad\qquad\qquad (2.52)$$

Henry and Holliday [62] took gas samples from both Söderberg and prebaked anode cells during normal electrolysis and anode effect, and made qualitative and quantitative analysis with a mass spectrometer. One set of samples were taken from within a steel can mounted over a hole in the frozen electrolyte crust, and were designated 'slightly burned gas' as there was very little exposure to oxygen. The second set of samples were taken from above open holes in the crust, and were designated 'nearly completely burned gas' as there was significant exposure to oxygen. For both cell types, COS was the only sulfurous species in the slightly burned gas during normal electrolysis, and when the gas became burned SO_2 became dominant. During anode effect COS and CS_2 were present in similar concentrations in the slightly burned gas, whereas in the nearly completely burned gas SO_2 was the main sulfurous species. During normal electrolysis the concentration of CO_2 is high and causes the formation of COS through reaction *2.50*, while during anode effect the CO_2 concentration is lower and causes CS_2 to be formed. Sulfur dioxide is the dominant sulfurous species in the burned gas through the oxidation of COS and CS_2 as seen in reactions *2.51* and *2.52*.

Oedegard *et al*. [72] analysed the COS, CS_2 and SO_2 emissions from a laboratory cell using a gas chromatograph equipped with a flame emission detector. Thermodynamic predictions were also made based on a series of reactions involving various sulfurous species. The laboratory cell showed the gas production in the order of COS > SO_2 > CS_2, which is expected as the cell was maintained with an inert atmosphere so oxidation of COS to SO_2 was not favoured, and was not run on anode effect so CS_2 was not favoured. The thermodynamic predictions showed SO_2 preferred at 1250K and higher CO_2/CO ratios, otherwise COS was the major sulfur containing gas.

While the research described above showed the presence of COS in the cell product gas, generally it was considered unimportant relative to SO_2, the dominant sulfurous species in oxygen rich gas. However in 1995 Harnisch et al. [73] put forward evidence to suggest that aluminium smelting is a significant source of atmospheric carbonyl sulfide. This is important as COS has a long atmospheric life and reacts with water to form sulfuric acid which catalyses reactions of ozone destruction. In a subsequent publication [74], an estimate was made of the global average emissions of environmentally harmful gases from aluminium smelting. It was also estimated that in 1995 aluminium production was responsible for about 6% of all COS

emissions and about 20% of the anthropogenic share. Therefore, besides the photochemical conversion of anthropogenic CS_2, aluminium production is established as the second major industrial source of COS, probably exceeding the contributions of automotive tyre wear and coal combustion.

The publications of Harnisch *et al*. [73,74] have raised the awareness of the importance of sulfur behaviour in aluminium smelting. Kimmerle *et al*. [75] measured COS, CS_2 and SO_2 emissions from prebaked anode cells. A gas chromatograph-mass spectrometer was used for the COS and CS_2 analyses, while ion chromatography was used for the SO_2, for samples taken from holes drilled in anodes. COS and SO_2 emissions were confirmed using tuneable diode laser absorption spectrometry on samples taken from the common exhaust duct of 64 cells. The results were similar to those of Oedegard *et al*. [72], and showed that about 96% of the sulfur in the anodes was emitted as SO_2 and only about 4% as COS. The gas sampled directly from the anode had similar levels of COS and CS_2, but the gas sampled from the exhaust duct had a COS/CS_2 ratio of 50:1, indicating the CS_2 being oxidised by air as it moved from anode to duct.

The effect of anode sulfur content on electrolytic carbon consumption has been studied over the sulfur range found in typical anodes. Sørlie *et al*. [76] reported no significant influence of sulfur on carbon consumption, as seen in Figure 2.24, however in a later publication Kuang *et al*. [77] found a very small decrease in electrolytic carbon consumption with increasing anode sulfur content. Therefore any benefit of increased sulfur content by reducing the carbon consumption must be weighed up against the harmful effects of the increased sulfurous emissions created by the higher anode sulfur content.
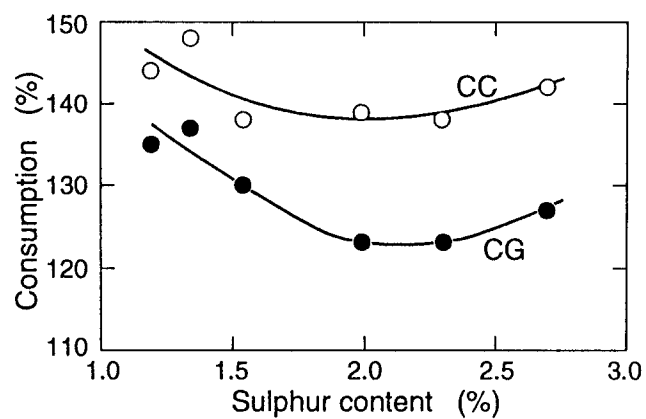
Figure 2.24 *Total electrolytic carbon consumption (CC) and carbon gasification (CG) as a function of anode sulfur content [76].*

3. Theory and Development of the Gas Analysis System.

The experimental basis behind most of the findings reported in this thesis is the use of a reliable gas analysis technique. This section describes some of the different techniques available, the rationale for selection of a quadrupole mass spectrometer, the theory of the technique used, and the development of the overall gas sampling and analysis system.

3.1. Gas Analysis.

A gas analysis technique was required that could provide both qualitative and quantitative analysis. Qualitative analysis was necessary to determine the various species present in the cell gas when the cell was under various conditions. Once the gas species were identified, the analysis technique had to provide quantitative analysis so those gas concentrations could be tracked. The technique had to also allow for quantification of several gas species simultaneously, as at the least carbon dioxide, carbon monoxide and a purging carrier gas would need to be analysed at the same time. This adds a further demand on the technique, because when multiple gas species are being quantified, the technique must differentiate between them. Another key feature required of the gas analysis was a fast response time, so that particular events occurring in the cell could be observed.

There are numerous gas analysis techniques available which are appropriate for analysis of smelter off-gas. Berge *et al*. [65] summarised the advantages and disadvantages of several gas analysis instruments, with particular focus on the ability to analyse perfluorocarbons. However the general characteristics are shown in Table 3.1, indicating the importance of choosing an instrument that suits the intended application.

Table 3.1 Advantages and disadvantages of different gas analysis instruments [65].

Instrument:	Advantages:	Disadvantages:
Infrared spectrometer		Interferences in the spectrum. Large and heavy FTIR-spectrometer has long response time. High price
Photo acoustic spectrometer (B&K 1301)	Low weight. Easy to transport. Large data storage capacity. Scans entire IR-spectrum. Measures all IR-active gases.	Has interference difficulties. Response time 2mins. Influenced by magnetic fields.
Photo acoustic gas monitor (B&K 1302)	Low weight. Easy to transport. Large data storage capacity. Not influenced by magnetic fields. Response time 1 min.	Has interference difficulties. Needs one optical filter to measure each gas.
Mass spectrometer (magnetic sector)	Analyses many gases in the same sample. Low detection limit. Response time 30 sec.	Molecular masses can overlap. Large and heavy. High price.
Gas chromatograph	Separates the gases before measuring.	High detection limit. Long response time 15 mins.
Micro gas chromatograph (MTI-M200)	Separates the gases before measuring. No interferences. Response time 1 min.	High detection limit.
Gas chromatograph/mass spectrometer	Separates the gases before measuring. Low detection limit.	Long response time 15 min. Large and heavy. High price.

Mass Spectrometer (portable)	Many gas species analysed. Relatively inexpensive. Small, light and portable.	Overlap of molecular masses. Susceptible to magnetic interference.

A small size and ease of transport is important if measurements are to be made in the potroom environment, whereas this is less important in the laboratory. Magnetic sector mass spectrometers are large and heavy, and although smaller, more portable models are available, the extremely high resolution of ions is sacrificed in the smaller models. Obviously any instrument to be used in a potroom must not be affected by magnetic fields.

The gas analysis technique selected for use in this study was quadrupole mass spectrometry, because this method best suited the requirements and had the least drawbacks. Some advantages and disadvantages of the instrument are shown in Table 3.1. The quadrupole mass spectrometer suited the requirements of being able to analyse many gases in the same sample with a fast response time. This is important as the ability to measure current efficiency and compare this to the variables in the cell relies on frequent gas analysis, because as the frequency of sampling increases the uncertainty in current efficiency decreases. Although a disadvantage of mass spectrometers is that there can be overlap of molecular masses, the technique has sufficient mass resolution to utilise the fragmentation patterns to differentiate between gases. Another disadvantage with the particular instrument chosen is the limited mass range of 1-100 atomic mass units. This precludes direct analysis of gases with a molecular mass above this, such as heavy hydrocarbons, however the fragmentation patterns of such species usually mean they can be successfully analysed within the limited range. While some quadrupole mass spectrometers such as magnetic sector instruments are large, heavy and expensive, in this case a small, portable unit was chosen. This provided suitable analysis in the laboratory, and also satisfied the long term goal which is able to be used in a smelter for analysis on a real cell. The characteristics of quadrupole mass spectrometry are discussed further in section 3.2.

3.2. Quadrupole Mass Spectrometry.

The composition of a gas stream can be determined by residual gas analysis (RGA) using a quadrupole mass spectrometer. With RGA a small trace of the total gas stream is leaked into

a vacuum chamber where the analysis takes place at high vacuum. The fundamentals of the technique and instrumentation are described in this section.

3.2.1. Principal of Operation.

The quadrupole mass spectrometer (QMS) used here, as with all mass spectrometers, has three stages of analysis. The stages of ionisation, separation and detection are illusrated in Figure 3.1.
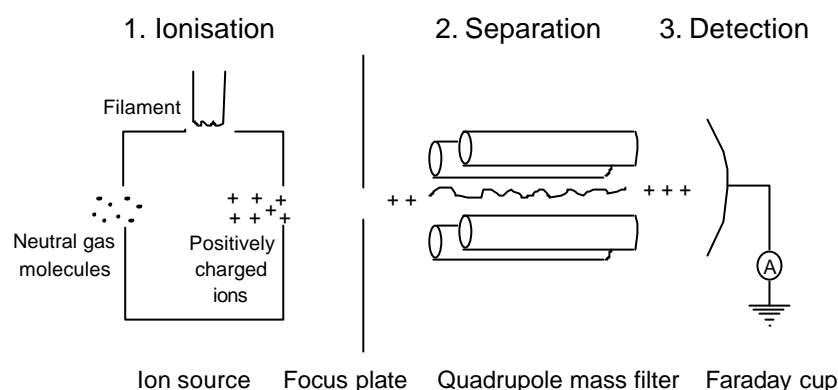
Figure 3.1 *Schematic of the ionisation, separation and detection stages of a quadrupole mass spectrometer.*

In the ionisation stage, electrons from a heated filament source are drawn across the chamber by a voltage, and at the low pressure some of the electrons collide with gas molecules. The impact of a high energy electron may cause one or more electrons to be ejected from a molecule, leaving a positive ion. The ion may subsequently fragment giving a characteristic pattern of smaller ions.

The focus plate arrangement prevents the ions from being collected at the surface of the vacuum chamber by focussing and accelerating them into the quadrupole mass filter. Here, opposing pairs of parallel rods act as high pass and low pass filters, combining to form a band pass filter. When a certain potential is applied across the rods, only ions of a particular mass range can pass through with a stable oscillating pattern. All other ions will either escape between the rods or be collected on them. The ion mass range can be made sufficiently narrow to only transmit ions of the same mass/charge (m/e) value. Generally, the larger the instrument the smaller the resolution between ions, in some cases down to fractions of an

atomic mass unit. The portable instrument chosen here had a resolution of 1 atomic mass unit. By varying the applied voltage, the entire m/e range is scanned, enabling separation of the ions by mass.

The ions passing through the mass filter are detected as an ion current by the Faraday cup, and, because the ion current is small, a high gain amplifier and an electron multiplier are used to magnify the signal. Løver [78] showed that for the instrument used, the ion current is linearly proportional to the partial pressure of the parent molecule at constant total pressure; the constant of proportionality being the instrument sensitivity. The mass spectrometer, through an internal calculation, converts the ion current to a partial pressure value at each mass/charge ratio.

A detailed description of the three stages is given by Løver [78] for a Ametek Dycor MA200M model quadrupole mass spectrometer. The residual gas analyser used for this study was a Ametek Dycor MA100M quadrupole mass spectrometer [79], which differed from the model described by Løver [78] in that it covered the range of 1-100 atomic mass units rather than 1-200 units. The smaller mass range was sufficient for the analysis required in this study because only small, low molecular weight species were being investigated.

3.2.2. Gas Ionisation and Fragmentation.

The gas molecules in the ionisation stage may become ionised with different charges, and may fragment into smaller ions. For example, the ionisation of carbon dioxide can yield ions of CO_2^+ (m/e = 44), CO_2^{2+} (m/e = 22), CO^+ (m/e = 28), O^+ (m/e = 16) and C^+ (m/e = 12). Elements with natural isotopes will also produce the corresponding ions, such as argon, which has ions at m/e = 40 (Ar^+), m/e = 20 (Ar^{2+}), as well as at m/e = 36 and m/e = 38 from the isotopes. Molecule ionisation depends on particle density, electron emission current, electron energy, material and temperature of the filament, cross-section and path length for molecule ionisation. Because of these factors, the relative intensities of the different ions from a particular compound may vary by ±15% [80]. Any fragmentation data in the literature must therefore be treated with caution and used only as approximate because they are strongly instrument dependent [81]. Table **3.2** gives the fragment ion relative intensities, expressed as a

percentage of the most intense peak, of the gases of interest to this study. This demonstrates the different ion patterns from different instruments. For example the main peak of argon is at m/e = 40, and the fragment ions at m/e = 20 vary from 11 to 20% in intensity relative to the main peak. Therefore the fragmentation patterns of the gases studied must be characterised on the particular instrument to be used. Table 3.2 also demonstrates the problem of overlapping peaks in mass spectrometry. For example both carbon monoxide and nitrogen have their main ion peak at m/e = 28. Therefore in a mixture containing both of these gases, the peak at m/e = 28 will contain contributions from both species, which can make quantification difficult.

Quantitative analysis can be made with a mass spectrometer by way of calibration. As the ion current, and hence partial pressure, at a certain mass/charge ratio is related to the gas concentration, then the height of the partial pressure peak will vary with gas concentration. Gases of known concentration can be sampled, and the resulting partial pressure peak heights used to generate calibration curves of mass spectrometer partial pressure *vs* actual gas concentration. The calibration equations can then be used to relate measured partial pressure to gas concentration for gases sampled from the electrolytic cell. As the ion current is linearly proportional to partial pressure at constant total mass spectrometer chamber pressure, the instrument must be operated at constant pressure. Therefore calibration must also be made at the beginning and conclusion of each experiment to ensure that any drift in total pressure during the experiment is accounted for.

An inert atmosphere was maintained in the laboratory cell to avoid oxidation of the exposed carbon at the high temperatures encountered. Nitrogen is the usual choice for the flushing or carrier gas to maintain inert conditions because of its relatively low cost. However, as one of the main gases of interest in this study was CO, nitrogen was unsuitable because of the interference problem discussed above. Argon was chosen as the inert carrier gas as it has peaks at m/e = 40 and 20, avoiding interference with any of the gases of interest.

Table 3.2 Fragment ion pattern coefficients in quadrupole mass spectrometry.

Gas	Mass	m/e	12	14	16	17	18	19	20	25	28	29	31	32	34	40	44	50	60	69
		Ref.																		
O_2	32	80			25.7									100						
		82			7.1									100						
		83			5						3			100						
		79			11									100						
N_2	28	80		13.2							100	1								
		82		5.5							100									
		83		5							100	1								
		79		7							100	1								
Air		80		12	3.6	0.2	0.8		0.2		100	0.9		20		1.3	0.2			
		79		6	3						100			27		1				
CO	28	80	6.6	1.3	2.8						100	1.3		0.3						
		82	2	0.8	1						100	1								
		83	5	1	2						100	1								
		79	5	1	1						100	1								
CO_2	44	80	11.8		17.4						17.5						100			
		82	1.7		4.8						13						100			
		83	2		6						7						100			
		79	6		9						11						100			
Ar	40	80							20							100				
		82							20							100				
		83							16							100				
		79							11							100				

Gas	Mass	m/e Ref.	12	14	16	17	18	19	20	25	28	29	31	32	34	40	44	50	60	69
CF_4	88	83						7		4			5		1			12		100
		84											4.9					11.8		100
COS	60	83	6								8				59		3		100	

Gas	Mass	m/e Ref	10	11	16	19	28	31	32	38	44	47	48	49	50	64	66	68	76	78
COF_2	66	85					14	5				100					55			
CS_2	76	83					5		22	6	17								100	9
		79					5		22	6	17								100	9
SO_2	64	83			5				10				49		2	100	5			
		79			5				10				49		2	100	5			
BF_3	68	83	1	5		3							27	100				5		

Gas	Mass	m/e Ref	12	19	24	31	32	39	48	50	64	67	69	83	86	89	100	102	105	107	119	138
C_2F_6	138	83	1	1				18		10			100								41	
		84				18.3				10.1			100				0.6				41.3	0.2
SOF_2	86	83			4		8		23			100	5		56							
SO_2F_2	102	83					13		8		8	29		100				74				
SOF_4	124	83					5					9			13	4			100	5		

3.3.   The Mass Spectrometer and Sample Inlet.

The residual gas analyser used for this study was a Ametek Dycor MA100M quadrupole mass spectrometer [79]. This instrument may be operated in either tabular or analogue mode. In analogue mode the entire mass spectrum or a certain span within the mass spectrum is scanned, and the partial pressure of the ions at each m/e ratio is displayed graphically. Analogue mode is useful for identifying the various species present in a total gas sample, by identifying the various peaks of a particular compound. In tabular mode, up to twelve m/e ratios can be targeted and the partial pressure of those peaks are tabulated. Tabular mode is useful for following the concentrations of particular gas species by recording the partial pressure of known m/e peaks. The dwell time, the time the mass spectrometer measures ion current at each m/e ratio, can be varied. Different dwell times give different relative errors in gas concentration. As dwell time is increased the noise in ion current decreases, however a longer dwell time increases the scan time so the drift of total chamber pressure becomes significant. As the ion current to partial pressure relationship is only linear at constant total pressure, any pressure drift introduces an error. There is a balance between the errors from ion current noise and pressure drift, and Clover [20] determined that the minimum relative error occurs with a dwell time of 250ms. With twelve channels used in tabular mode and a dwell time of 250ms, each scan through all channels takes approximately 35 seconds. Thus the current efficiency, via gas analysis, could be determined at a frequency of nearly twice per minute, much faster than many of the previous studies into current efficiency discussed in section 2.5.

It is an operational requirement that the filament in a mass spectrometer needs a low pressure to minimise burn-out. Therefore the mass spectrometer needed a supporting vacuum pumping system to achieve and maintain a high vacuum. Also, the higher the vacuum achieved, the lower the baseline of residual gas in the vacuum chamber, and the higher the accuracy of analysis. A schematic of the vacuum system is shown in Figure 3.2.
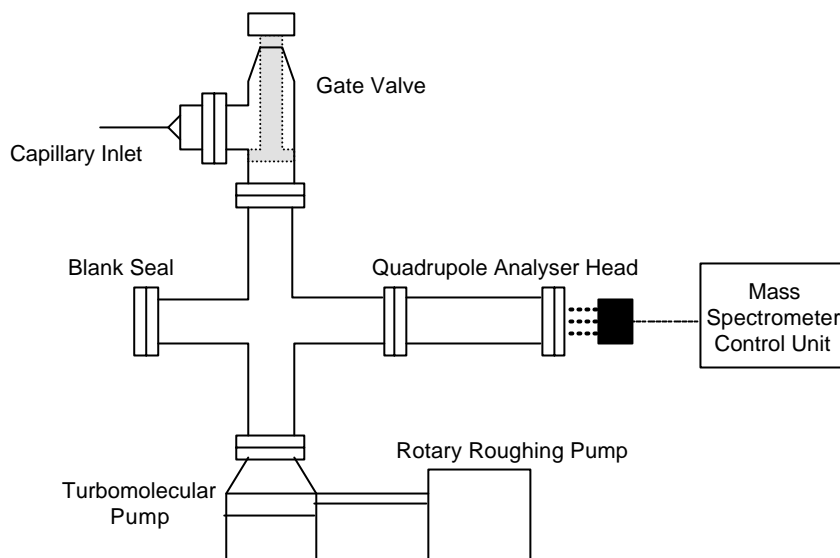
Figure 3.2 *Schematic of the vacuum system*.

The pumping system used was an Alcatel combined rotary backing vacuum pump and turbomolecular pump. This unit utilised an internal pressure sensor to automatically switch from rough pumping to turbo-molecular pumping when the pressure became low enough. If the pressure then increased above the level suitable for turbo-molecular pumping, a warning indicator was triggered. The gate valve was again used so the vacuum chamber could be isolated from the gas inlet when analysis was not being performed. This allowed a much lower pressure during the "off" times, resulting in less wear on the mass spectrometer filament. When gas analysis was performed the valve was opened to allow the gas sample into the chamber.

The gas inlet to the chamber was made with a capillary tube of small internal diameter. This gave an adequate pressure drop, ensuring the pressure inside the chamber remained at a suitably low level for mass spectrometric analysis while allowing continual sampling of process gas. Initially a 50μm glass capillary tube was used, but it soon became apparent that the glass was damaged by the fluoride gases from the electrolysis cell. The glass capillary was then replaced with a 64μm PEEK capillary tube, which proved successful as this polymer was unaffected by the gases encountered. The cell gases were also filtered, a discussion of this is given in the following section 3.4.

The capillary was sealed with graphite ferrules inside a custom made fitting. When the fitting was tightened, the graphite ferrules were compressed around the capillary tube, providing a gas tight seal. Caution was needed as if the fitting was tightened too far, the PEEK capillary could be crushed by the ferrules. To ensure the fitting was tight enough and air could not leak through between the graphite ferrules and the capillary, the system was leak tested with helium. If a leak was present the system was tightened until the leak ceased.

Figure 3.2 demonstrates the gate valve in the closed position, sealing the chamber. When opened, a small volume of the total gas flow is continuously sampled through the capillary into the vacuum chamber and the mass spectrometer.

3.4. Gas Flowrate Control and Determination.

To ensure accurate current efficiency determination, the mass spectrometer had to be rigorously calibrated, and the gas flow rate through the cell had to be determined accurately. This was achieved through the use of two MKS type 1459C flow controllers, connected to a MKS type 247C 4 channel readout unit.

The mass spectrometer was calibrated for carbon dioxide and carbon monoxide as these were the gases that needed to be quantified for current efficiency determination. The calibration gases used were a CO_2/Ar mix, a CO/Ar mix and pure Ar. The calibration procedure involved using the two flow controllers to vary the flows of both pure argon and the CO_2/Ar mixture, which were then mixed prior to analysis by the mass spectrometer. Following the CO_2 calibration the routine was repeated using the CO/Ar mixture.

After calibration, the gas from the reduction cell was analysed as electrolysis proceeded. However another problem occurred with the PEEK capillary becoming blocked after exposure to the cell gas. Upon observation the gas appeared to be slightly smoky, and solid deposits of condensed electrolyte volatiles were left on the inside surface of the tubes carrying the gas.

The cell gas was filtered passing it through a small fluidised bed of alumina, which provided a high contact surface area, effectively removing condensed fines and HF from the gas stream.

Only +106μm screened alumina was used so fines were not carried over to the following gas tube and capillary inlet to the mass spectrometer. The alumina bed was supported on a packed bed of 2-3 mm diameter alumina spheres, which acted as the gas distribution for the filter. A second packed bed of alumina spheres was held above the alumina to act as a preliminary knock-out device in case of any surges or spouting. A small knock-out pot was also placed directly after the fluid bed filter to collect any fine alumina particles formed by attrition and any solid material knocked off the alumina. The alumina was oven dried before use so there was no possible reaction between moisture in the alumina and the cell gases, and fresh alumina was used for each experiment.

The fluidised bed filter appeared to remove all trace of the volatile matter from the gas stream, resulting in a cleaner gas downstream and eliminating capillary blocking. The presence of the alumina bed had no apparent effect on the detection of any of the gases of primary interest. Roberts and Ramsey [66] showed conclusively that CF_4 and C_2F_6 do not undergo reactions with alumina, by passing the gases through a fluidised bed of alumina and measuring the gas concentrations before and after the bed with a mass spectrometer. Sulfur dioxide is adsorbed onto alumina in dry scrubbers [86-89], however it will desorb and be replaced on the surface of the alumina by the preferential adsorption of hydrogen fluoride. There are conflicting reports on the reaction of carbonyl sulfide with alumina. Kimmele *et al*. [75] stated that there was no decomposition of COS when smelter duct gas was passed through a dry scrubber, whereas Utne *et al*. [90] reported an apparent decrease in the COS content of duct gas after passing through the dry scrubber. The decrease was small and the samples before and after the scrubber were not taken simultaneously, so doubt is drawn on the finding. Therefore if there is any reaction of SO_2 and COS with scrubbing alumina, it is very small indeed, and not of significance to the qualitative findings regarding sulfurous gases in this study.

The flow of the carrier argon into the cell was controlled with one of the flow controllers. The flowrate of the gas from the cell could not be measured directly with the flow meters, as the devices would not respond when looped together because of pressure drop difficulties. Also, the flow meter method of operation requires knowledge of the gas composition, which was continuously changing. However as the flow of argon into the cell was accurately metered, and the concentration of the argon in the gas from the cell could be determined, the total flow

from the cell could be calculated. If the flow was measured directly, and some of the gas escaped prior to the measurement point, the gas leaking would not be accounted for. An advantage of back-calculating the cell gas flow from the composition was that any gas leaking was accounted for. By determining the flow indirectly, the assumption was made that any gas lost had the same composition as the total gas flow. Therefore the gas analysed was entirely representative of the total gas flow, and 100% gas recovery was not necessary. However the equipment was still designed to eliminate all possible sources of gas leakage.

A schematic of the gas flow system is shown in Figure 3.3. The mass flow controllers were connected to the readout display unit, from where the calibration factors for the various gases and the desired flows could be dialled in and verified on the display. Calibration factors were needed because of the different heat capacities of the gases relative to pure nitrogen. For argon the factor was 2.78, for the Ar/CO_2 mixture it was 2.482 and for the Ar/CO mix it was 2.664. The end of the mass spectrometer inlet capillary was placed inside the gas tube to sample a small trace of the gas flow, the unsampled stream was collected by a fume extraction system.
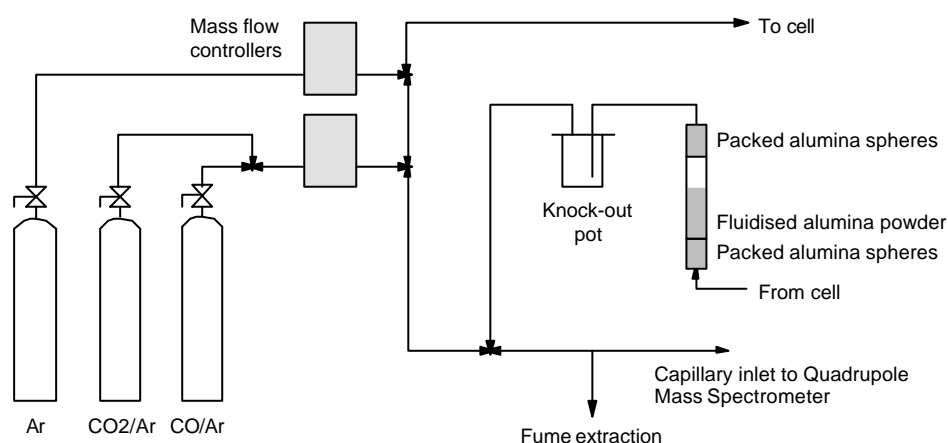
Figure 3.3 *Schematic of the gas metering and filtering system.*

3.5. Improvements to the Accuracy of Gas Analysis.

There were several aspects of the gas analysis that were altered to give an improvement to the overall accuracy of analysis. The first of these was the level of sealing in the vacuum system.

As seen in Figure 3.2 there are many connections between the various fittings and pumps that make up the vacuum system. All of these are a possible source of leaking into the chamber. If any of the connections are not sealed properly, then a small leak of air into the chamber will result. This means that the background level of all the peaks where air appears, especially at m/e = 28 (N_2) and m/e = 32 (O_2), will be elevated. Figure 3.4 demonstrates the calibration of the mass spectrometer with poor sealing. CO_2 was calibrated for between scans 50 and 100, and CO between scans 110 and 150. Up to scan 50 pure argon was sampled, and the traces at m/e = 28 and 44 were at their baseline levels. When the CO_2 calibration was started at scan 50, the trace at m/e = 44 rose correspondingly, and showed step increases as the gas concentration was stepped up. When the CO_2 calibration was completed the partial pressure decreased back to a baseline level. The CO_2 calibration demonstrates the difficulty introduced by fragmentation. There was no CO in the CO_2 calibration gas, however there was a response of the peak at m/e = 28, due to the CO^+ fragment from CO_2. During the CO calibration the trace of m/e = 28 showed step increases in a similar way to CO_2. The poor sealing is illustrated by the high baseline of the m/e = 28 peak. As can be seen after scan 50, it is difficult to resolve the increase in the partial pressure above the baseline. The accuracy of analysis is diminished as small changes in the partial pressure are masked by the large baseline value.
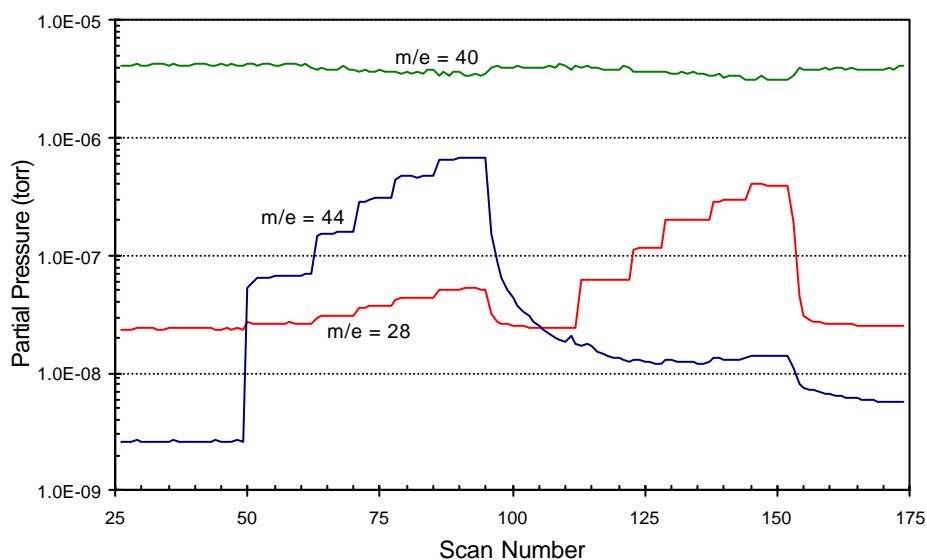
Figure 3.4 *Mass spectrometer calibration with poor vacuum sealing.*

To ensure that all leaks were found and sealed, the vacuum system was leak tested with helium. The contrast between poor and good vacuum sealing is demonstrated in Figure 3.5.
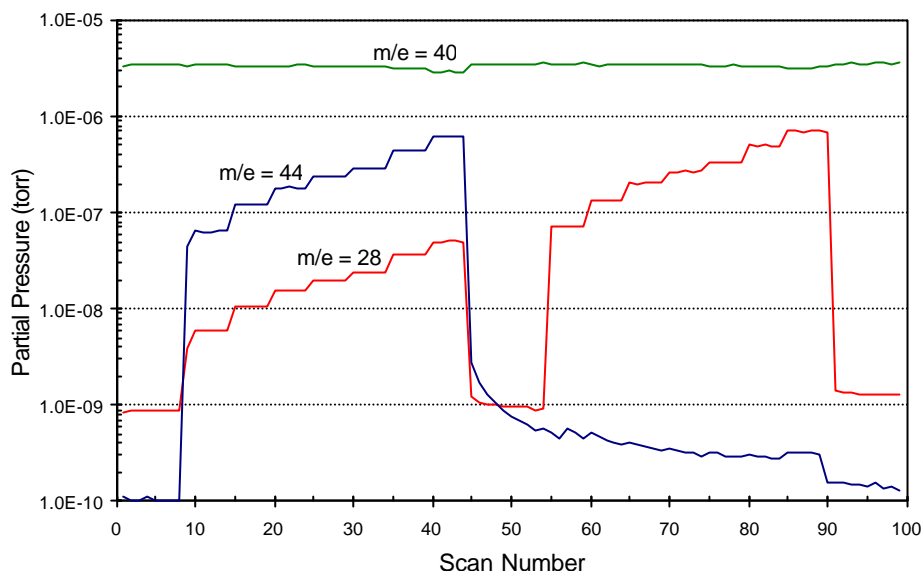
Figure 3.5 *Mass spectrometer calibration with good vacuum sealing*.

The calibration was again performed in the same order, with CO_2 first, then CO. In this case the baseline level of m/e = 28 was significantly more than an order of magnitude lower than seen in Figure 3.4. The increase in the partial pressure at m/e = 28 when the calibration was started is clearly definable, and the ratio of signal intensity to baseline intensity was much larger. There is also a very small response at m/e = 44 during the CO calibration, due to a very minor CO_2 impurity in the CO calibration gas mixture. This had no influence on the CO calibration, so was disregarded.

Figure 3.4 and Figure 3.5 demonstrate the fragmentation of CO_2, providing a reading at m/e = 28. When only CO_2 was present, as with calibration, this was not a problem. However when both CO_2 and CO were present, as during the cell gas analysis during electrolysis, the signal had to be resolved into the true contribution from CO and the extra contribution from fragmented CO_2.

The calibration algorithm developed firstly determined the equation of a polynomial calibration curve fitted to the CO_2 partial pressure *vs* concentration data, and did the same for CO. It also determined the fragmentation CO partial pressure "CO" at each CO_2 concentration, and

the ratio of "CO"/CO_2. These curves are illustrated in Figure 3.6. The algorithm proceeded to calculate the CO_2 concentration during electrolysis. The next step used the "CO"/CO_2 ratio to determine the "CO" value, which was then subtracted from the apparent CO partial pressure, giving a corrected value. The final step calculated the CO concentration. The calibration algorithm and calculations are discussed in more detail in chapter 5.
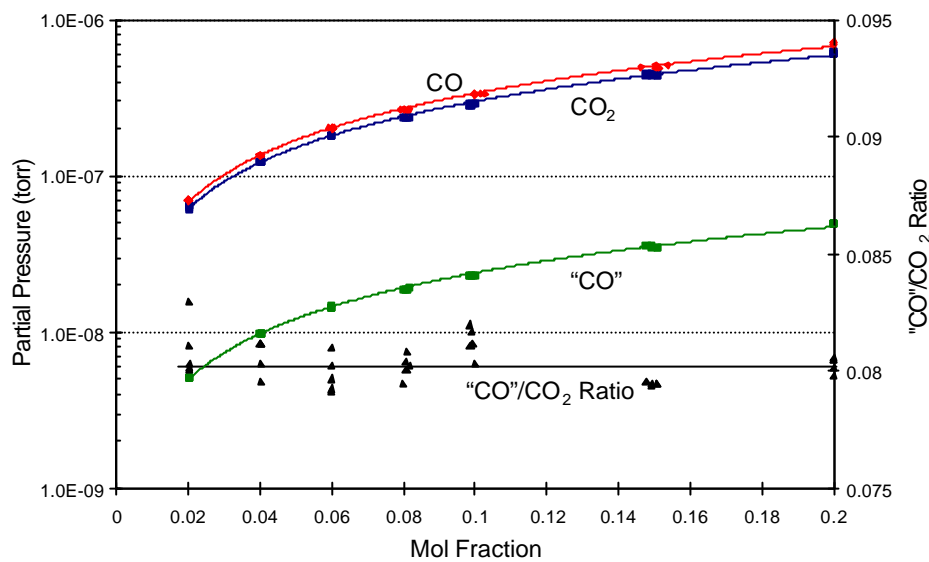
Figure 3.6 *Calibration curves for the data displayed in Figure 3.5*.

Initially the ratio of "CO" to CO_2 partial pressures appeared to be non-linear, although investigation found this was due to the baseline level of the signal at m/e = 28. At the lower CO_2 concentrations, the relative amount of signal that is baseline was larger, creating a false trend. To account for this, the algorithm was refined to subtract the baseline values from the signals at m/e = 28 and 44 before calibration curves were plotted. The "CO"/CO_2 ratio, when determined with the baselines being subtracted, was constant across the concentration range used, and was always approximately 0.08. This is in comparison to the values seen in Table 3.2, with the m/e = 28 fragment from CO_2 having an intensity ranging from 7 to 18% relative to m/e = 44.

Another advantage of subtracting the baselines was that this took into account any variation in the baselines during the experiment. This was important because the baseline at m/e = 28 was found to be different during calibration and analysis of gas from the cell.

71

To further take account of any drift by the mass spectrometer during each experiment, the calibration algorithm was extended to include calibrations at both the start and end of the experiment. After the baselines were subtracted the two calibrations were expected to be very close, and if there was a large discrepancy this was investigated. The gas concentrations during the electrolysis period were calculated with both the starting and ending calibration equations, and then the concentration was interpolated from these.

It was noted that the baseline at m/e = 28 was often higher at the end of an experiment than at the start. It was suspected that CO may have been adsorbing onto the surface of the metal inside the mass spectrometer chamber over the duration of each experiment. To limit any adsorption and make it constant, an external heating coil was placed around the mass spectrometer vacuum chamber, which maintained a temperature of approximately 70°C.

Experimental data which displays the problems of different baselines and a significant difference between calibrations is shown in Figure 3.7. The baseline at m/e = 28 was stable during the first calibrations up to scan 150, but had increased by the time the second CO_2 calibration was performed. Then during the second CO calibration, started at scan 350, there was a huge increase in the baseline, and the calibration was at partial pressures significantly higher than at the start of the experiment. This was indicative of a major leak developing in the vacuum system during the experiment, as the partial pressure of the Ar ion also showed a step increase.
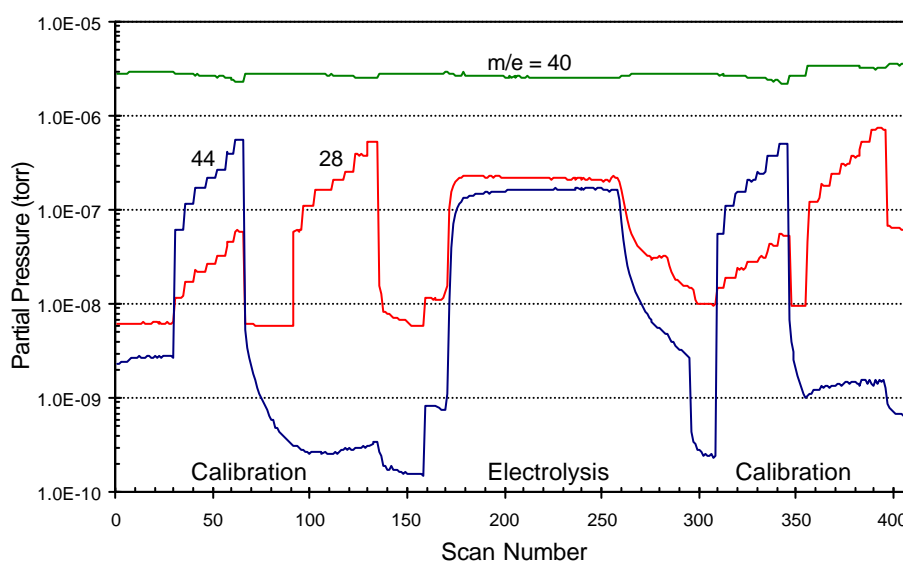
Figure 3.7 *Mass spectrometer data with varying baseline values.*

Figure 3.8 shows the same data as Figure 3.5, although it is extended to cover the entire experiment. The first calibration was between scans 10 and 90, and the second was between scans 250 and 330. Gas from through the cell was analysed starting at scan 100, and electrolysis was performed from scan 120 until anode effect occurred at scan 200.

The stability of the mass spectrometer is demonstrated by the similarity between the first and second calibrations. Although the second calibration was made to ensure that if the mass spectrometer had drifted it could be accounted for, the calibration curves were almost identical. Also the baseline values remained at almost the same levels throughout the experiment, indicating the success of heating the mass spectrometer to ensure this. When comparison is made with the data in Figure 3.7 it can be seen that the mass spectrometer is much more stable in its operation and analysis.
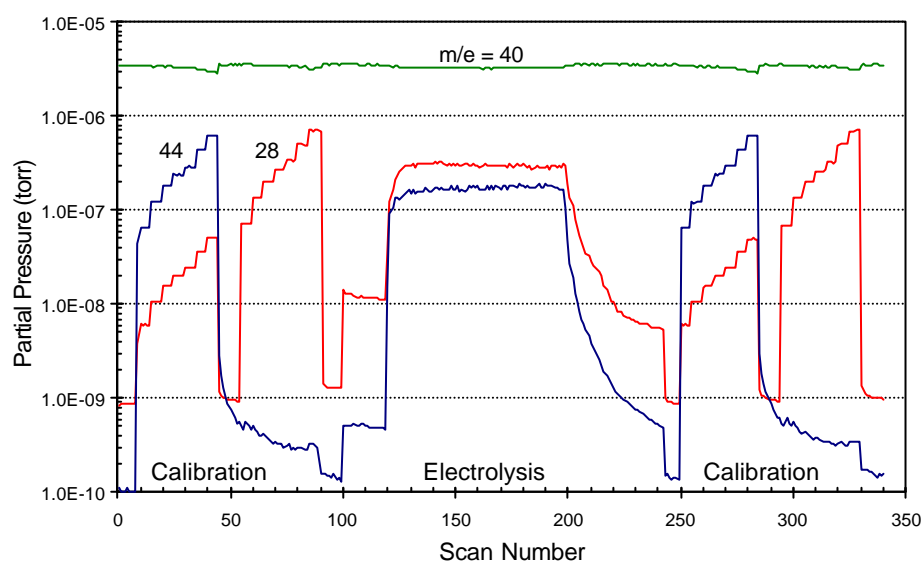
Figure 3.8 *Mass spectrometer data for an entire experiment.*

This chapter has described the desired gas analysis properties, and how a quadrupole mass spectrometer was chosen to meet them. The gas analysis system was designed to allow sampling with a fast response time and frequent analysis. Rigorous calibration and easy changing between calibration and analysis were possible. The system was refined to improve the analysis by altering the physical components and by changing the mass spectrometer data manipulation algorithm.

4. Design and Operation of the Experimental System.

An experimental system was designed to allow electrolysis with suitable control of variables such as current density and anode-cathode spacing. The system had to allow for capture of the cell product gas, and access to the electrolyte for samples to be taken. Data acquisition was incorporated to collect the desired measurements such as temperature, cell voltage and current, and the mass spectrometric readings from the gas analysis.

4.1. Experimental Cell.

The cell consisted of a graphite crucible and a carbon anode, housed in an inconel container placed inside a furnace.

The graphite crucible (Donald Brown and Co. Auckland, NZ) was used to contain the electrolyte and act as the cathode. A new anode was used for each experiment to ensure the condition of the anode was not a variable that could affect the current efficiency. The anodes were machined from a spent anode butt obtained from New Zealand Aluminium Smelters Ltd (Tiwai Point, NZ), and were suspended into the electrolyte from above. A cylindrical boron nitride shield (Boride Ceramics and Composites Ltd, Kent, UK) was placed inside the crucible to shield the side walls, defining the cathode area to the base of the crucible only. This made the geometry closer to that of a real cell, and also increased the cathode current density. Another piece of boron nitride (from the same suppliers) was placed over the top and sides of the anode. This limited the amount of vertical anode area exposed to the electrolyte, increasing the anode current density, and also limited reaction between the anode gases formed and the exposed anode carbon. The dimensions of the crucible, anode and boron nitride pieces are given in Figure 4.1.

The significant difference between the cell from this laboratory and those used in many previous studies is the larger size [19,21,30,35,91]. The larger crucible allowed a greater volume of electrolyte to be contained, so longer electrolysis times before anode effect were possible. With an effective cathode diameter of 110 mm and the large anode, much higher currents could be used than in the past without giving excessive current densities. For example, a current of 75 amps gave an anode current density of 1.107 A/cm^2 and a cathode current density of 0.789 A/cm^2. This lies within the typical range of anode current density found in prebaked anode industrial cells of 0.7 to 1.2 A/cm^2 [92]. The higher current meant that larger volumes of off-gases were produced, which improved the gas analysis.

The current was supplied by a Hewlett Packard DC Power Supply System 6672A. This was a digital, programmable DC power supply, capable of 0-20 V and 0-100 A. The power supply had a programming accuracy of 20 mV and 60 mA, and a resolution of 5 mV and 25 mA. Two identical power supplies were connected in series, giving a capability of 0-40 V and 0-100 A. This allowed a higher voltage during anode effect, so the anode effects would be more similar to the occurrence in real cells.

Figure 4.1 *Dimensions of the crucible, anode and boron nitride inserts.*

The anode boron nitride cap had a small angled section where it overhung the edge of the anode. This allowed bubbles to be released without being trapped under the boron nitride, which could have resulted in reaction between the gas and anode carbon. The anode cap was very durable as only a small part was placed into the molten electrolyte. The majority of the cap only exposed to the high temperature inert gaseous atmosphere above the electrolyte. The cathode boron nitride shield, although mostly submerged into the molten electrolyte, was also very durable. It was used for more than thirty five experiments before it failed by cracking in a circular nature around the level of the electrolyte surface. Both pieces of boron nitride were heated very slowly to 1000°C in an inert atmosphere to prevent thermal cracking, before being used in contact with molten electrolyte.

The crucible had two holes through the walls, near the top and on opposite sides. This allowed it to be picked up from inside the furnace container with a pair of tongs while at the cell operating temperature. The cathode boron nitride insert could then be retrieved and the molten electrolyte poured out at the conclusion of each experiment, preventing the boron nitride from being frozen into the crucible and allowing it to be re-used.

The cell was housed in a metal container (inconel alloy 600, Sandvik Australia) that fitted into the heating chamber of the furnace. This alloy was used as it is resistant to corrosion at the high temperatures and corrosive gases generated. The furnace container was closed with a lid, and a gas tight seal was made with a high temperature silicone o-ring. Water cooling was provided on the top of the lid and on the underside of the container flange to ensure the o-ring was not overheated and the seal remained intact.

The anode was suspended into the electrolyte from the lid above, which also had fittings for a thermocouple (measurement of electrolyte temperatures), the electrical connection to the cathode, and an access port for electrolyte sampling. The anode and cathode connecting tubes also had thermocouples placed down the inside, providing temperature measurement from near the centre of the anode and at the top of the crucible wall, as seen in Figure 4.1.

The underside of the furnace lid was insulated with refractory to reduce heat losses through the lid, and also to reduce the outer surface temperature of the lid for safer handling. The anode,

cathode and thermocouple fittings through the lid were swagelock fittings with teflon inserts, which meant the anode and cathode shafts and the thermocouple could be moved up and down while maintaining a gas tight seal. The gas in and gas out fittings were swagelock fittings with metal inserts which provided a gas tight seal in a fixed position. The gas inlet pipe extended down to just above the top of the crucible, whereas the gas outlet pipe only just protruded through the lid, as seen schematically in Figure 4.2. This was to ensure that the gases produced by reaction at the anode were not trapped at the bottom of the furnace container and that the argon flushing gas did collect and remove them. The port for electrolyte sampling was sealed with a rubber o-ring, and could be opened and closed when required.
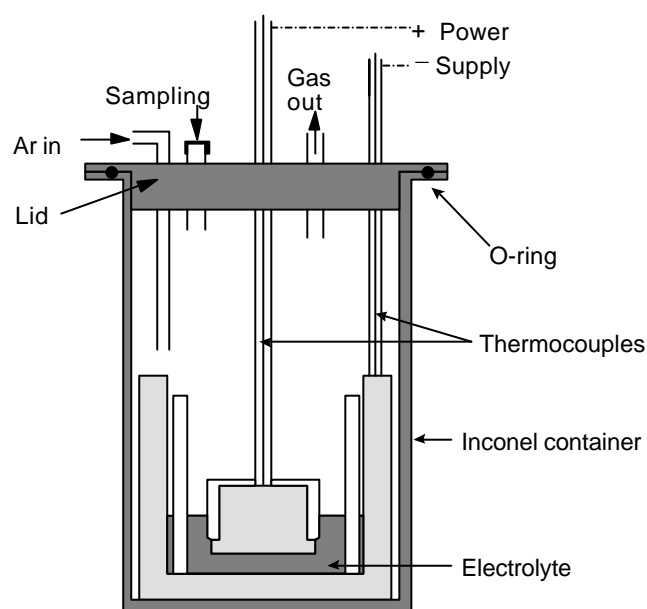
Figure 4.2 *Schematic of the furnace container, lid, anode and crucible.*

A top view of the lid is shown in Figure 4.3. The anode fitting was placed in the centre of the lid, and the cathode fitting was placed at the correct spacing to drop into the hole in the middle of the crucible wall. Both the thermocouple fitting and the sampling port were placed to be above the middle of the gap between the two pieces of boron nitride, so the electrolyte was accessible.

Cooling water flowed through a copper pipe which was brazed onto the lid, ensuring good contact and heat transfer. The pipe passed around the centre of the lid to help keep the temperature to a safe level. There were two handles on the outside of the lid to allow easy

removal from the furnace container, especially when the cell was at operating temperature. The lid was fastened on the furnace container through holes around the perimeter, which made certain that the o-ring was sealed around the whole lid. There was also a earth lead attached to the lid, so that it was electrically safe in case of any short circuit from the furnace.
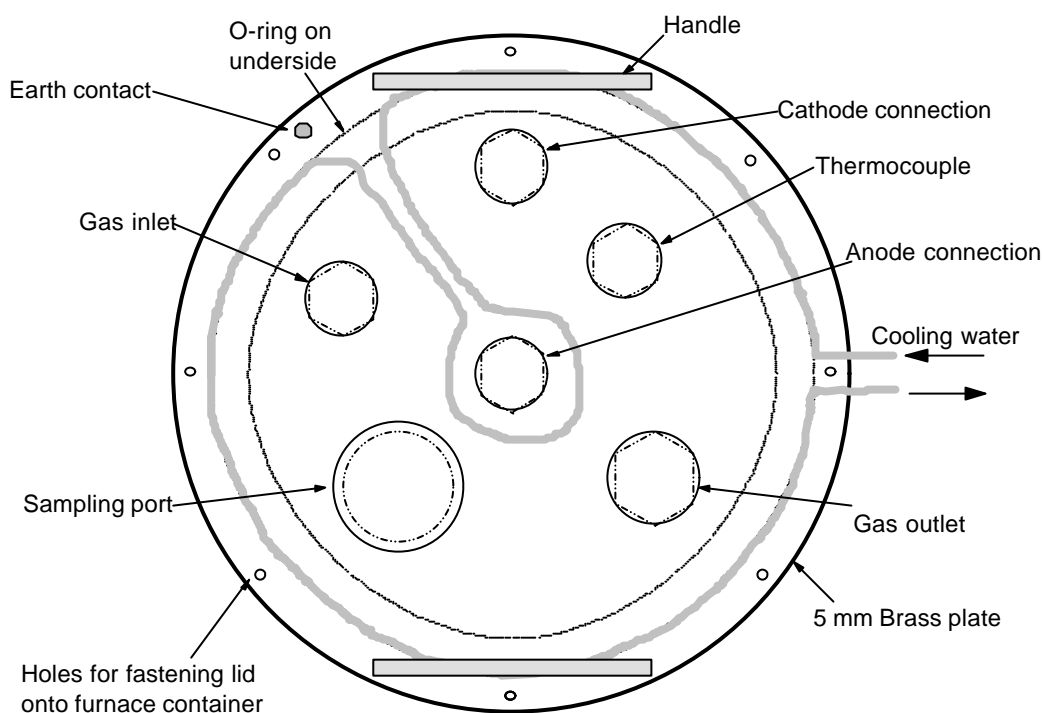
Figure 4.3 *Top view of the furnace lid.*

The experimental cell was heated in a custom-built stand alone furnace, shown schematically in Figure 4.4 (Engineering Workshop, The University of Auckland). The furnace was electrically powered and consisted of eight silicon carbide resistance heating glo-bars (Kanthal Corporation, Perth, Scotland) oriented vertically around a cylindrical chamber. The chamber was built of refractory bricks, surrounded by a layer of insulating glass wool, and was contained in a steel frame. The furnace had cooling water pipes around the sides of the frame, and around the electrical connections to the heating elements at both the top and base of the chamber. The furnace container was placed inside the chamber upon a layer of refractory brick.

The temperature was measured with a thermocouple which was placed through the furnace wall to the outside of the base of the furnace container. The furnace was controlled with an

EMC type 483 programmable controller. This allowed programs of up to six consecutive stages, each stage consisting of a temperature ramping speed, a desired target temperature and a holding time at that temperature.

In normal operation, only one stage of programming was used. The furnace was heated slowly to operating temperature over a period of more than twelve hours, was held at the operating temperature until the experiment was completed, and was then switched off and allowed to cool down slowly to room temperature.
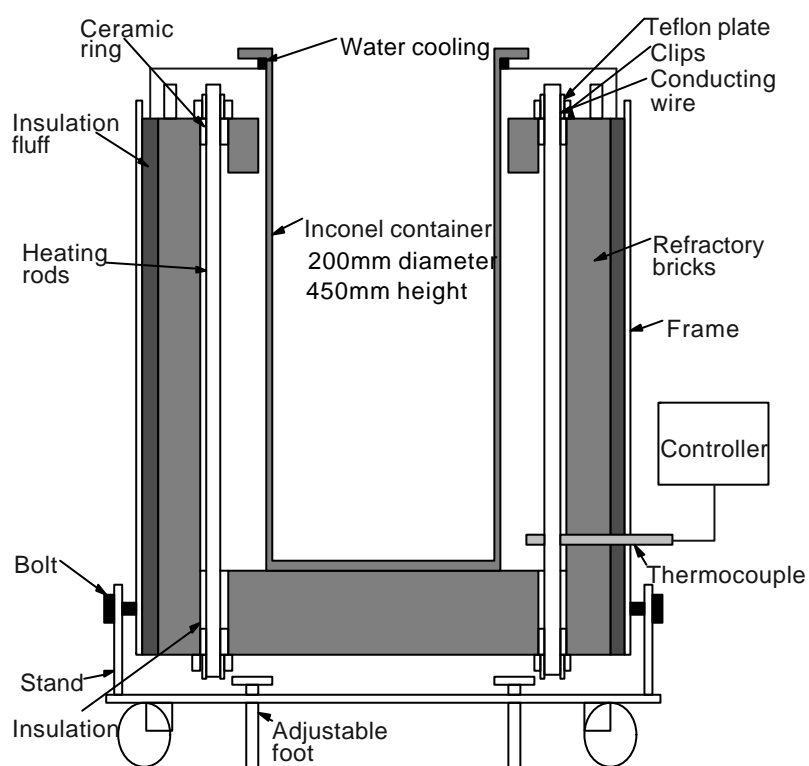
Figure 4.4 *The furnace and inconel container.*

4.2. Data Acquisition.

The data acquisition was made with the use of two computers, one to record the mass spectrometer data and the other to record the other data from the gas flow controllers and the electrolysis cell. A schematic of the data acquisition is given in Figure 4.5.
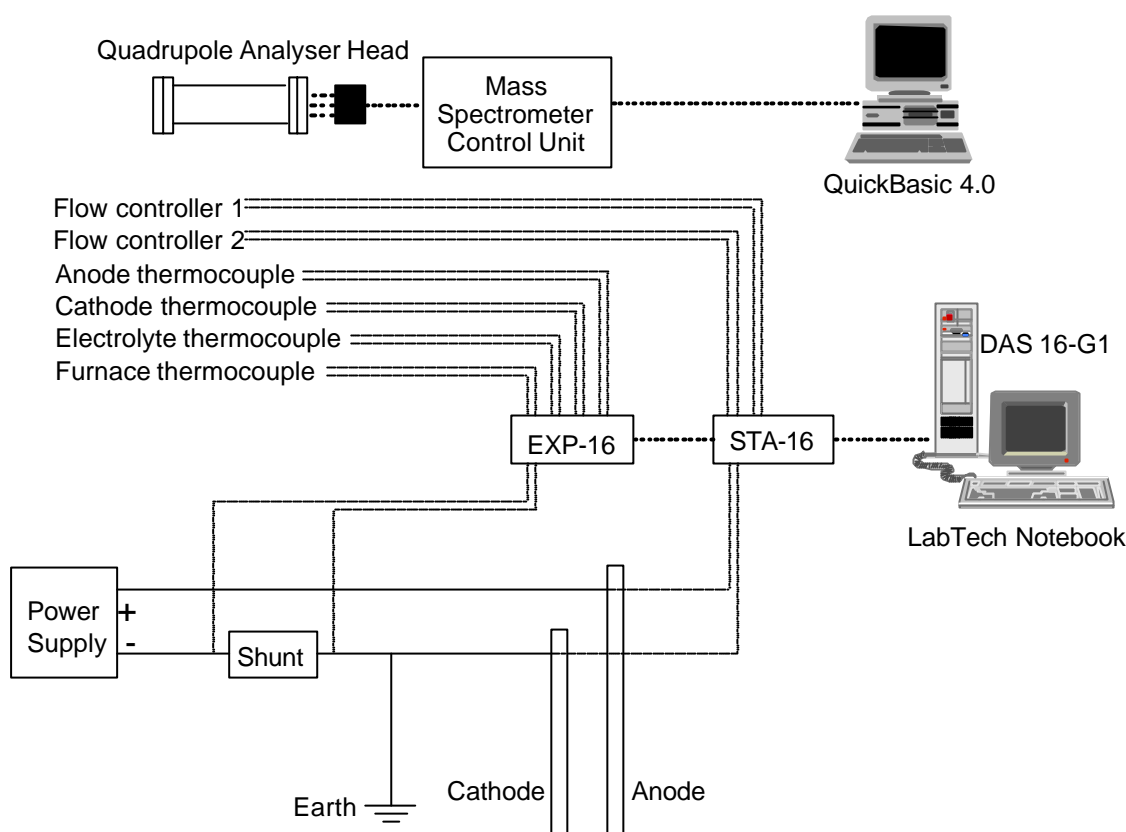
Figure 4.5 *Schematic of the data acquisition.*

The mass spectrometer was controlled by, and the data recorded by, a program custom written for the Quick BASIC Version 4 program language [20]. Communication between the computer and mass spectrometer was via the RS-232C interface. The program was used to check the on/off state of the mass spectrometer filament, specify the m/e ratios to be analysed, the dwell time for the analysis, and the starting and ending times of the analysis. The data was recorded to a file in a tabular mode, listing the scan number, total pressure inside the mass spectrometer chamber, and the partial pressure at the twelve m/e ratios, for each successive scan. The program also displayed graphically in real time the partial pressure of four of the channels. The channels could be selected and changed when required, and the vertical scales could be altered to provide a better display of the data as it varied.

The rest of the data was taken using the Keithly Metrabyte system of an EXP-16 expansion board for millivolt signals, an STA-16 board for volt signals, a DAS16-G1 card inside the computer, and the LabTech Notebook data acquisition program. The type of signal and final derived measurement for the different devices are shown in Table 4.1.

80

Table 4.1 Signal Measurement and Calculation.

Device	Signal	Derived Measurement
Anode thermocouple	mV	°C
Cathode thermocouple	mV	°C
Electrolyte thermocouple	mV	°C
Furnace thermocouple	mV	°C
Cell current	mV	A
Cell voltage	V	V
Flow controller 1	V	l/min
Flow controller 2	V	l/min

The thermocouples were K type, and the signals were taken directly into the EXP-16 board. The conversion to degrees Celsius was made by the thermocouple calibration tables in LabTech Notebook.

The cell current was calculated by measuring the voltage drop across a shunt resistor placed on the cathode side of the electrical circuit, and dividing this by the resistance of the shunt. The shunt was placed on the cathode side of the circuit because this side was where the circuit was earthed. If placed on the anode side, the entire cell current could find an alternative earth through the data acquisition cards and the earth of the computer.

The cell voltage was measured with contacts at the top of the anode and cathode connecting shafts. Therefore the measurement also included the voltage drop across the length of those metal tubes, as well as across the contact between them and the anode and cathode respectively. The anode hole was threaded with a ¼ inch UNF thread, and was wound onto the corresponding thread on the end of the connecting shaft. To improve the electrical contact, graphite powder was placed around the thread first. The cathode connection was made by pushing the connecting shaft into a hole in the top of the side wall of the crucible. With time this hole became worn and slightly enlarged, and the electrical connection deteriorated. Therefore several new holes were machined, and used for successive groups of experiments.

The gas flowrate from the two flow controllers was determined by measuring the voltage output that the controllers sent to the readout unit. The voltage was then multiplied by the calibration factor corresponding to the gas concentration at that time. The signals between the flow controllers and the readout unit were carried by factory supplied cables. An intermediate connection was made which allowed access to the plug pins that carried the voltage signal corresponding to flowrate.

As discussed previously, when the mass spectrometer was operated with twelve channels having a dwell time of 250 ms each, the time to complete 1 scan was 35 $^{1}/_{3}$ seconds. In order for the data collected through the DAS card into the second computer to be synchronised with the mass spectrometer data, LabTech Notebook was programmed to acquire data at the same sampling rate. To achieve this, the signals were measured at a rate 3 Hz, and block averages were calculated over 165 measurements, a frequency of 0.0283 Hz.

The data acquisition programs on the two computers were initiated simultaneously at the start of each experiment. The difference in sampling frequencies between the two computers was small enough that after 5 hours of sampling, the difference in samples was less than 2 seconds, much less than the sample period of 35 $^{1}/_{3}$ seconds.

The overall experimental system worked effectively, allowing experiments to be carried out investigating the influence of cell variables on current efficiency, the gases produced during different stages of electrolysis and anode effect, the changing cell voltage during electrolysis, and also the characteristic behaviour of the cell itself. Possible future modifications could include an alumina feeding apparatus to allow very slow continuous feeding into the electrolyte during electrolysis. This would mean that electrolysis could be carried out for longer periods with smaller changes in alumina concentration before the occurrence of anode effect and termination of measurements.

5.   Current Efficiency Determination Algorithm.

This section describes in more detail the algorithm that is used to calculate current efficiency from the initial mass spectrometer data. The assumptions made and justification of them are discussed, and the accuracy of current efficiency is verified through crosschecking. The algorithm is broken into the stages of calibration, determining gas concentrations and finally the oxygen balance to determine the current efficiency.

5.1.   Mass Spectrometer Calibration.

The mass spectrometer data collected for each experiment consisted of the partial pressure at twelve different m/e ratios recorded every 35 seconds. The m/e ratios of interest to current efficiency calculation are 40, 44 and 28 corresponding to argon, carbon dioxide and carbon monoxide respectively. The other channels were used to monitor other gases of interest, such as those produced during anode effect, which is discussed in chapter 8. An example of the data relevant to current efficiency is shown in Figure 5.1.
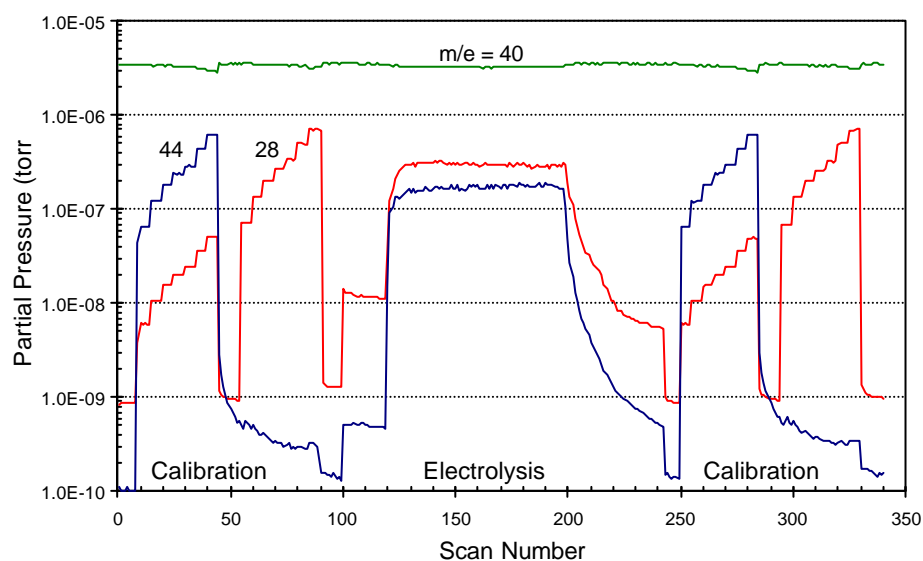
Figure 5.1 *Mass spectrometer data for an entire experiment.*

CO and CO_2 were the only gases quantified for the modified oxygen balance because gas monitoring of other oxygen containing species indicated that responses were either not detected or were at such a low and constant level that there would be no noticeable effect on the measured current efficiency.

The delay time to measure a step change in the concentration of these gases was less than one scan, or 35 seconds, as seen in Figure 5.1, when there were definite steps during the calibration stage. The delay time when the gases were passed through the electrolysis cell was still less than one scan, as shown by the response at the start of the electrolysis stage of each experiment.

The calibration was made by mixing the calibration gases, giving different CO_2 and CO concentrations which were sampled for a number of scans. The calibration gases were 20 ± 0.2 mol% CO_2 (balance argon), 20 ± 0.2 mol% CO (balance argon), and pure argon. They were mixed with the flow controllers, which had a range of 0-10 l/min, with an accuracy of $\pm$ 1% of flow, repeatability of ± 0.02 l/min and resolution of 0.01 l/min.

The flows were varied as follows to obtain calibration points up to 20 mol% CO_2 or CO:

Table 5.1 Gas calibration flowrates.

Ar	CO_2/Ar or CO/Ar	Total flow	Ar	CO_2 or CO
l/min	l/min	l/min	mol%	mol%
1.0	0	1.0	100	0
4.5	0.5	5.0	98	2
2.0	0.5	2.5	96	4
1.5	0.5	2.0	95	5
1.17	0.5	1.67	94	6
0.75	0.5	1.25	92	8
0.5	0.5	1.0	90	10
0.33	1.0	1.33	85	15
0	1.0	1.0	80	20

Between 2 and 10 mol% CO_2 or CO the argon flow was varied and the mixture flow held constant so that only one of the flows had to be altered between calibration points, meaning a faster change of gas concentration and finer definition in the gas analysis.

Synchronous gas flow rate and mass spectrometer partial pressure data were recorded, which enabled the actual gas concentration at each calibration point to be plotted against the partial pressure reading. The mass spectrometer variability at a constant gas concentration was tested by performing calibrations for extended periods, and calculating the deviation around the mean reading. The standard deviation in partial pressure, when translated into gas concentrations, was $\pm$ 0.35% of the CO_2 concentration value and $\pm$ 0.17% of the CO concentration value.

Polynomial curves were fitted to the calibration data, generating calibration equations of the form:

$$y = a + bx + cx^2 \tag{5.1}$$

where y is the gas concentration (mol fraction), x is the partial pressure (torr, corrected in the case of CO) and a, b, and c are constants. The curves for the starting calibrations of the experimental data above are shown in Figure 5.2.
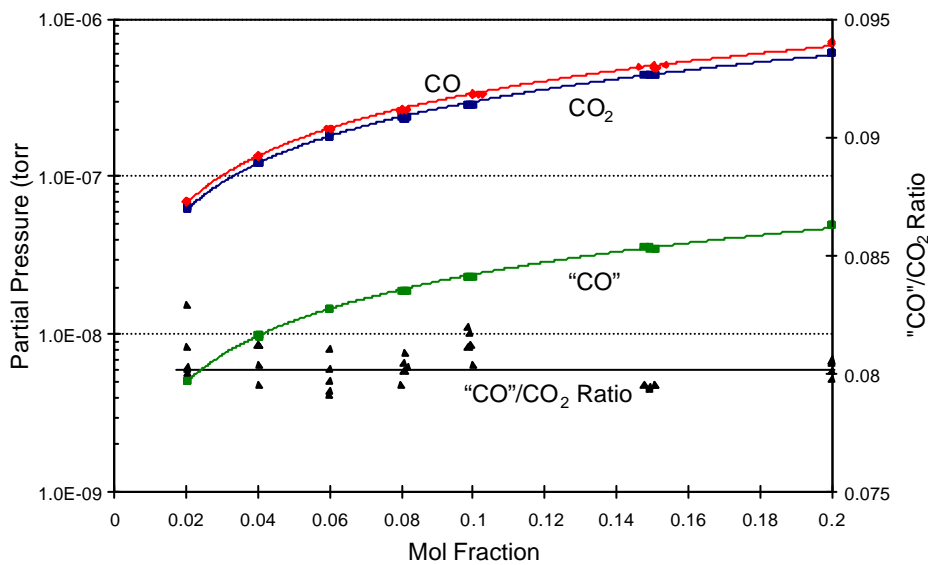
Figure 5.2 *Calibration curves of the starting calibration data in Figure 5.1.*

The calibration equation constants of the curves above are given in Table 5.2. The constants for the calibration curves of the ending calibration are also given. The high r^2 coefficients indicate the very good fits made through the calibration data, and are typical of the values for all experiments.

Table 5.2 Calibration curve constants.

		a	*b*	*c*	r^2
CO_2	start	-0.004369	376436	-6.8374E+10	0.9996
	finish	-0.006380	390462	-8.0780E+10	0.9990
CO	start	-0.005205	346602	-7.7966E+10	0.9988
	finish	-0.004851	344240	-7.0385E+10	0.9989

5.2.   Product Gas Concentration.

The calibration equations were applied to the data during electrolysis, generating curves of gas concentration *vs* time as shown in Figure 5.3. The horizontal axis has been changed from scan number to time to indicate the actual duration of electrolysis, and also to better define the electrolysis starting point.

The gas concentrations determined during electrolysis had a general pattern of increasing as electrolysis was started, proceeding with some minor variation until anode effect occurred, the falling away as the cell current dropped The gas concentrations took about 5 minutes to build up to a steady concentration, and dropped rapidly when anode effect occurred in the cell after 46 minutes of electrolysis.

Figure 5.3 also demonstrates the rapid response of the gas analysis, with gas concentrations given approximately every 35 seconds. The concentrations vary from point to point, however the variation is small and overall trends are still apparent.

A feature of the product gas concentrations is the saw-tooth type variation in both CO and CO_2. Investigations were made to determine if this point-to-point variation was real or was due to the experimental technique. There was some small variation in the argon flow signal, as mentioned earlier, however this measurement had no impact on the CO and CO_2

concentration variations seen above as it was not part of the calculation. The argon flowrate variation did impact on the current efficiency calculations, and is discussed later in section 5.3. The gas bubble release frequency from under the anode was measured to see if it was of similar magnitude to the gas analysis frequency, and a possible source of noise. The bubble release frequency was determined by measuring the cell voltage with a fast sampling frequency. The voltage increased and dropped as each bubble was formed and then released, and the number of bubbles in a period of time were counted.
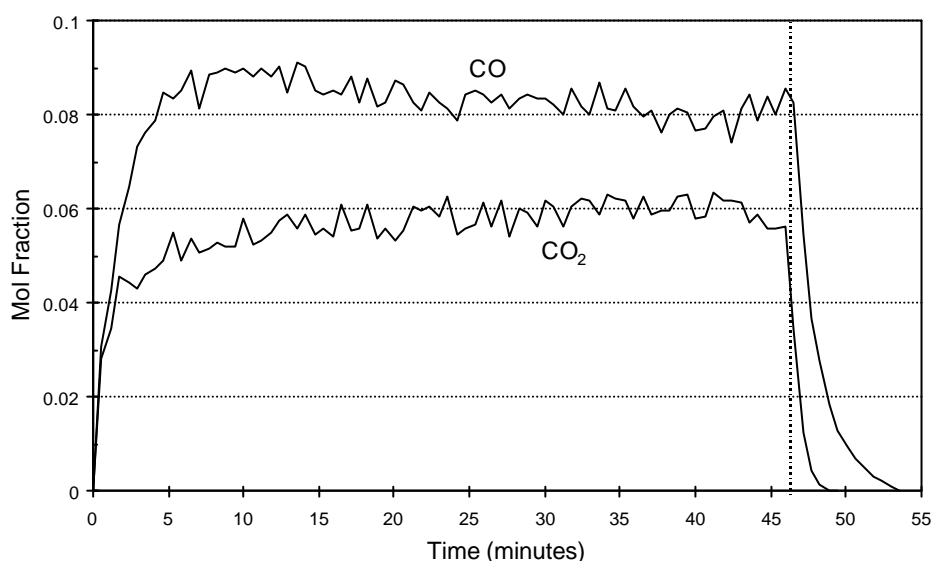
Figure 5.3 *Gas concentrations calculated from the mass spectrometer data.*

The bubble release frequency is plotted against anode current density in Figure 5.4. The current density was varied by changing the cell current with the same sized anode. Therefore with gas production proportional to current, a linear bubble release relationship is expected, and seen, with a linear coefficient of 0.9826. At the normal cell current of 75A (anode current density 1.107 A/cm2) the bubble release frequency was approximately 0.9Hz, many times more frequent than the gas analysis, as the mass spectrometer sampled every $35\frac{1}{3}$ seconds (0.0283Hz). Even at the lowest current density used the bubble release was still an order of magnitude faster than the gas sampling. Therefore the variation in point to point gas concentration was shown not to be a result of the sampling technique, and must be considered the real variation for the cell.
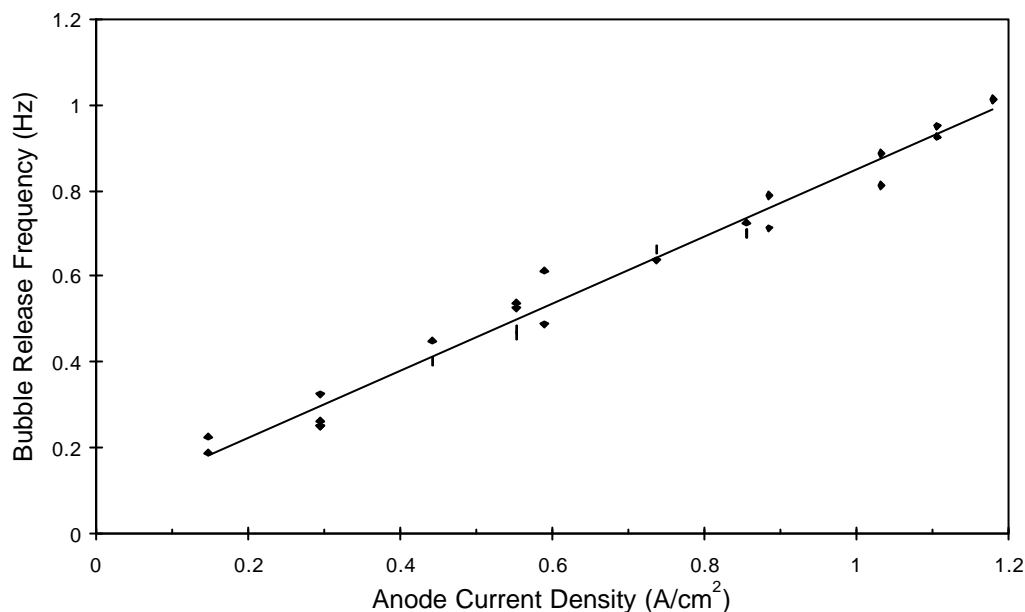
Figure 5.4 *Anode gas bubble release frequency.*

5.3. Current Efficiency Determination.

As described in chapter 2, the current efficiency was now calculated using the oxygen balance method. A critical part of the method is the measurement of the argon flowrate into the cell. This was done by measuring the output voltage signal from the flow controller, and converting this to a flowrate with a calibration factor. This gave a flowrate with a standard deviation of 0.017 l/min, and this point to point variation resulted in a noisy current efficiency *vs* time plot. As this variation was a result of the data acquisition method, the variation was reduced by taking a moving average of 10 measurements, approximately equal to the gas residence time in the cell, which reduced the standard deviation to 0.004 l/m. Also if there was any instantaneous change in the flow of argon into the cell, it would not be expected to be observed immediately in the gas flowrate out from the cell because the cell acted as a buffer to short term variations in the flow. The flowmeter had a stated variability of ± 0.02 l/min, which is slightly larger than the actual measured value of ± 0.017 l/min. However, when calculating the theoretical variability in the overall current efficiency measurement the conservative flow variation figure was used.

The flowrate of argon into the cell was combined with the argon concentration in the product gas to determine the product gas flowrate, which was converted to a molar flowrate using the ideal gas law. The molar flow of oxygen from the CO_2 and CO was then calculated, and compared to the theoretical molar oxygen determined with Faraday's law, giving current efficiency.

The plot of current efficiency *vs* time (from the gas concentrations seen in Figure 5.3) is shown in Figure 5.5. The current efficiency increased for a few minutes until it reached a stable level, and is then shown as electrolysis proceeded until anode effect occurred after 46 minutes, when it dropped away quickly.

There are two main features of the current efficiency *vs* time plot. The first characteristic of the data in Figure 5.5 is that generally there is very little variation in current efficiency with time. To obtain a single value for the current efficiency for the experiment, an average was taken. To ensure that the initial increase in current efficiency did not influence the average value and comparisons could be made between different experiments, the first 10 minutes of each experiment were not included in the average. The current efficiency shown in Figure 5.5, after the 10 minute starting period, had an average value of 81.5%.
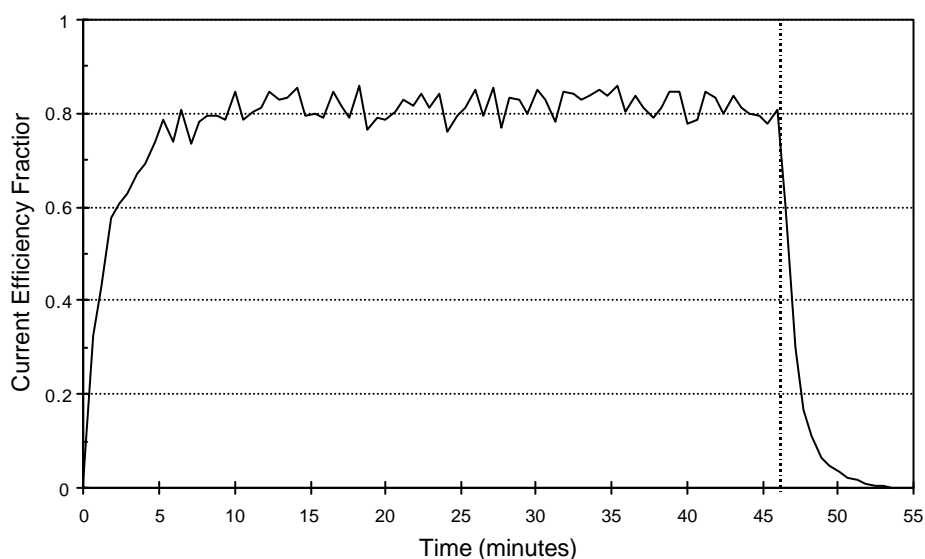
Figure 5.5 *Current efficiency calculated by the oxygen balance method.*

The accuracy of the current efficiency values was determined by calculating the current efficiency using the limits of accuracy of the contributing data. The calibration gas concentration and gas flow rate data accuracy combined to give a theoretical overall current efficiency accuracy of $\pm\,4\%$. The accuracy was also influenced by the digital power supply programming accuracy, although this variation was very small and only caused a $\pm\,0.05\%$ difference to current efficiency. The detailed calculation of current efficiency accuracy is given in Appendix 1. While the theoretical accuracy appears to be wide, the absolute values of current efficiency are second in importance to the trends that are shown in detail in chapter 6.

To confirm the validity of the values calculated, a comparison was made between the current efficiency and the depletion of alumina in the electrolyte. Electrolyte samples were taken before electrolysis was started and after anode effect occurred, and the alumina concentrations were determined by Leco analysis (performed by Comalco Research Services, Melbourne, Australia, using a Leco RO-416DR oxygen instrument with the standard nickel/tin flux method and blank correction). For this experiment the starting alumina concentration was 6.0 ± 0.09 wt% which had reduced to 2.8 ± 0.09 wt% at anode effect. The current efficiency was integrated with time, and this was used to calculate the faradaic consumption of alumina during electrolysis. Using the known starting alumina concentration, the effective electrolyte volume gave the starting alumina weight. Subtracting the electrolytic consumption gave the final alumina weight, which with the final electrolyte weight gave the final alumina concentration. In this case the alumina concentration back-calculated from the current efficiency was 2.97 ± 0.25 wt%, which compares very closely with the analysis of 2.8 wt%, verifying the current efficiency calculation method and that the values measured are reasonably accurate.

The second characteristic is the scatter in the data. The variability in the current efficiency due to the argon flowrate signal measurement has already been taken account of, as discussed earlier in this section. To determine if the scatter observed is an experimental artefact, analysis was made of how the variability of the data impacted on the current efficiency variability. When the variations in gas flowrate (from the flow controller) and partial pressure (from the mass spectrometer) were considered, the corresponding current efficiency variability would be $\pm\,1.00\%$ (detailed calculations are given in Appendix 1). This is a conservatively high estimate of the variability, as the actual flow rate variation was less than that used in the calculations.

However this is still significantly lower than the standard deviation of current efficiency observed in any of the experiments performed. The standard deviation of the current efficiency in Figure 5.5 is 2.64% around the average of 81.5%.

Therefore the scatter demonstrated in the current efficiency plot (Figure 5.5) is real, and may be caused by gas waves or gas induced electrolyte mixing. While the exact reason is not clear, this type of variation has been seen in other current efficiency studies using the oxygen balance method. Figure 5.6 shows the current efficiency from an Aluminium Pechiney study by Leroy and Pelekis [25], where there was also variation around a steady state value.
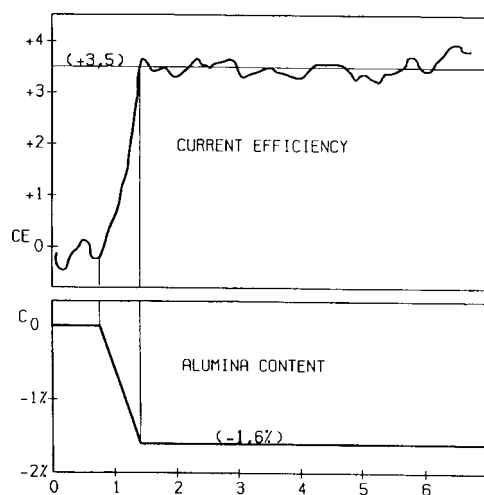
Figure 5.6 *Current efficiency variability [22].*

While the electrolytic reduction of alumina is a chemical reaction, there are continuously changing physical conditions such as the surface of the anode, the size and shape of gas bubbles under the anode, the electrolyte chemistry as it circulates in the cell, the current density varying as each gas bubble is formed and then released, and the anode-cathode distance increasing as the anode is consumed on a micro scale. Because of this dynamic situation, it is not surprising to see such variability in the current efficiency.

The current efficiency determination algorithm provides an accurate method for measuring current efficiency with a fast response time. The accuracy of the measurement is given, and the values are verified by crosschecking with the alumina concentration. The theoretical variability is given, and the variation in the current efficiency response is shown to be real.

91

6.   Cell Performance and the Effect of Key Variables.

This section covers the general performance of the cell, discussing the composition of the product gas and the level of current efficiency attained in the cell. Results are presented demonstrating the effect of cell parameters on current efficiency, covering anode-cathode distance, current density and electrolyte chemistry. The final results presented are the influence of alumina concentration on current efficiency.

6.1.   General Performance of the Cell.

The product gas concentrations of CO and CO_2 for an experiment are shown in Figure 6.1. This demonstrates the common finding of the CO concentration being higher than (or in some cases about equal to) the CO_2 concentration. This is different to the normal gas concentrations from an industrial cell during electrolysis, where the CO_2 concentration has been measured at 5-7 times larger than CO [64].
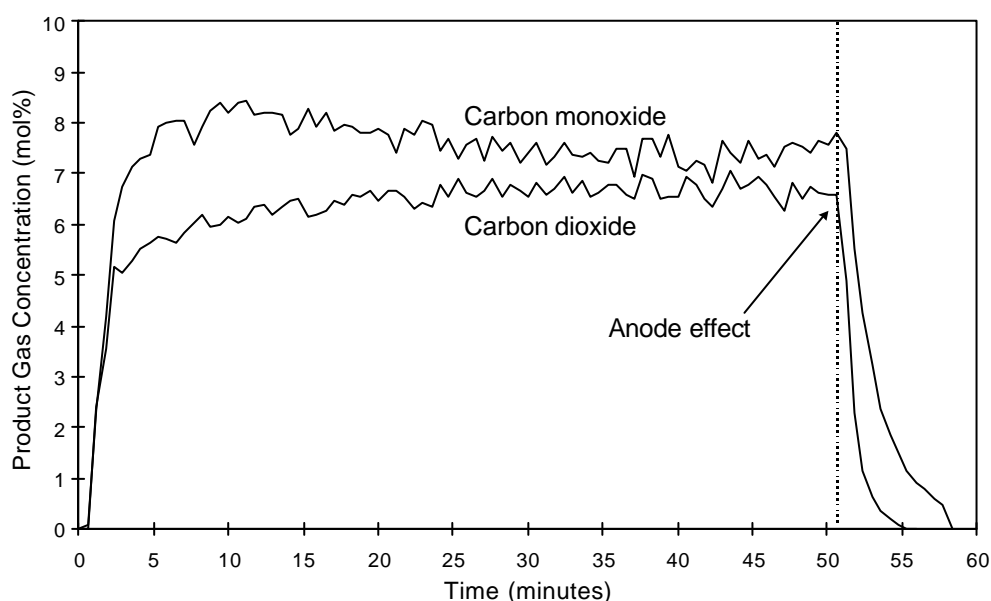
Figure 6.1 *Product gas concentration during electrolysis.*

Also of note is the large initial difference in the gas concentrations. This may be due to the initial condition of the anode. The anodes were machined from a spent anode butt (New Zealand Aluminium Smelter Limited, Tiwai Point, NZ), and a new anode was used for each experiment. Because CO formation is favoured on the less ordered carbon in the anode structure [9], there may have been preferential consumption of the binder pitch in the initial new anode surface until an equilibrium state was reached. The Boudouard reaction also occurs preferentially with the binder carbon, so may be more prevalent at the beginning of electrolysis.

Another explanation is that at the beginning of the experiment there is no dissolved CO_2 in the electrolyte, and during the initial stages of each experiment the dissolved CO_2 may build up to the equilibrium level. Assuming 100% current efficiency and CO_2 being the only product gas, less than one minute of electrolysis would be needed to produce enough CO_2 to achieve the equilibrium level. However, most of the gas is released as bubbles, CO is also formed and the current efficiency is significantly lower than 100% during the starting period. Therefore the build-up of dissolved CO_2 in the electrolyte is likely to take several minutes longer. Also the dissolved CO_2 will be consumed by back reaction, further lengthening the build-up period. There is also no oxygen present in the system, which would otherwise increase the CO_2/CO ratio.

The final factor influencing the build-up of the product gas concentrations once electrolysis is started is the mixing in the cell of the product gases with the much larger purging gas flow. This causes a small time lag from electrolysis starting until the product gas composition has built up to the true level.

The product gas composition was then used to determine the current efficiency via the oxygen balance, as outlined in chapter 5. A typical current efficiency *vs* time trace is shown in Figure 6.2.

93
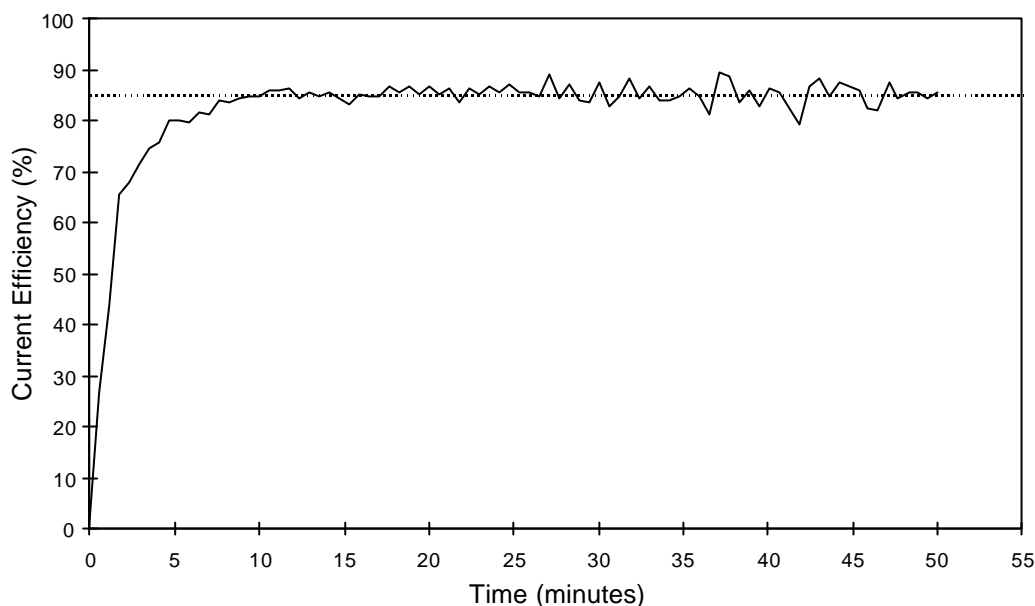
Figure 6.2 *Current efficiency vs time.*

The mixing of the reaction product gases with the purging gas during the initial stages of electrolysis, showing an apparent build up in efficiency, is highlighted. During this period the metal dissolution and reoxidation will be moving to its steady state value. There is also some resistive heating of the electrolyte during this period, which may contribute to the starting effect. While this means that for an initial period the current efficiency is not stable, this behaviour has been reported for other laboratory cells [21] and is unavoidable with the experimental set-up used.

The resistive heating of the electrolyte during the early stages of electrolysis is illustrated in Figure 6.3. The electrolyte and anode temperatures were stable before electrolysis was started at 0 minutes. At this point the temperatures rose as both the anode and electrolyte underwent resistive heating. The electrolyte temperature increased by 8-10 °C in about 15 minutes, with the largest increase in the first few minutes. The temperatures were then quite stable, although the electrolyte temperature rose slightly in the last few minutes before anode effect. This small rise agreed with the cell voltage, which increased as anode effect was approached and the cell resistance increased. During anode effect the very high voltage across the cell caused an interference with the thermocouple signals, so the temperatures could not be measured. However, as soon as anode effect was terminated by switching the current off, measurements indicated the temperatures had increased. Castellano *et al.* [21] showed a

94

similar anode temperature increase of 10-15°C during anode effect for a 5A laboratory cell. The anode effect was terminated by switching the power supply off, and with the no current flowing the temperatures quickly returned to the pre-electrolysis levels.
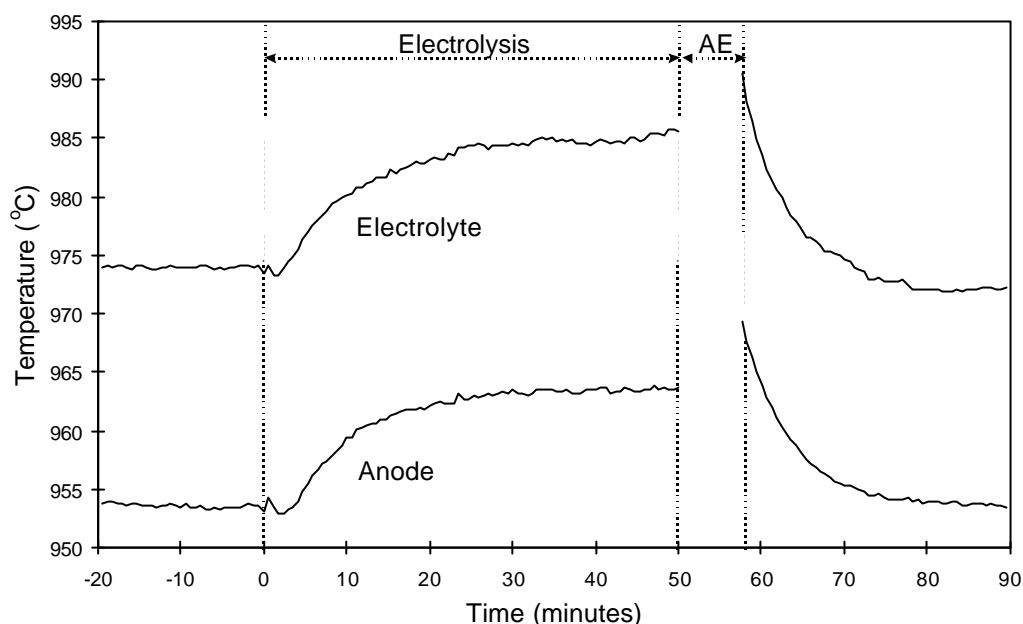
Figure 6.3 *Electrolyte and anode temperatures during electrolysis.*

The measured electrolyte temperature is much higher than the anode temperature because of the positions of the thermocouples. The electrolyte thermocouple is placed directly into the electrolyte, whereas the anode thermocouple is positioned in the connecting shaft, at the top of the anode.

At the start of electrolysis the calculated electrolyte liquidus temperature (based on composition) was 959°C [93], giving a superheat of 14°C. By the onset of anode effect the liquidus temperature had increased to 973°C, and the increased electrolyte temperature meant the superheat was maintained at 13°C. Therefore while the electrolyte temperature increased during the experiment, the superheat remained relatively constant. The disadvantage of the high currents used and the resultant resistive heating, was that the electrolyte temperature could not be accurately controlled during electrolysis. This meant that the effect of temperature on current efficiency could not be determined with the present arrangement. However, as shown by the studies reviewed in section 2.5.1, there is universal agreement that increasing temperature has a negative effect on current efficiency.

95

The overall average current efficiencies achieved in the cell of between 70 and 90% (the average seen in Figure 6.2 is 85.4%) appear low compared to industrial cells where the current efficiency is usually above 90%. This indicates that the current efficiency achieved in the laboratory cell is significantly lower than in industrial cells, the main reason being the design of the cell. When the electrolyte was mixed from the individual components before the cell was heated, no aluminium metal was added. The lack of a metal pad at the start of each experiment meant that as aluminium was produced it would have formed small droplets on the non-wetting cathode surface. This would give rise to an increased mass transfer area between aluminium and electrolyte, allowing a greater opportunity for back reaction and loss of current efficiency. This is also indicated by the high ratio of CO to CO_2 in the product gas.

There is also some loss of current efficiency due to the formation of aluminium carbide and from sodium reduction. However these losses are small, and would be expected to be much lower than the accuracy of the measured current efficiency.

Another factor which could influence the measured current efficiency is the involvement of the boron nitride pieces used in the cell. Fellner *et al*. [19] proposed that BN reacts with CO_2 when immersed in electrolyte according to reaction *6.1*:

$$2BN + 3CO_2 = B_2O_3 + 3CO + N_2 \tag{6.1}$$

In further work Grjotheim et al. [35] confirmed the presence of nitrogen in the product gas when helium was used as the carrier gas. Because of the presence of nitrogen, which was assumed to be from reaction *6.1*, a correction was made when using the Pearson-Waddington equation. The authors also found a carbon deficit , which could have been caused by further reaction with boron nitride:

$$2BN + 3CO = B_2O_3 + 3C + N_2 \tag{6.2}$$

Both reactions *6.1* and *6.2* constitute a loss of oxygen if B_2O_3 is not included in the oxygen balance. If they occur to a significant extent then some adjustment must be made to account for them, or there will be a systematic error in the measured current efficiency. However the

shape of the current efficiency curves would not be altered, so trends highlighted would still be correct.

Silny and Utigard [91] also investigated the reduction of CO_2 to CO by boron nitride according to reaction *6.1*. CO_2 flowing over BN without electrolyte present did not react, whereas when electrolyte was present CO_2 reacted noticeably, with 17% CO in the product gas. To check if the reaction was caused by the BN or the electrolyte, CO_2 was passed through electrolyte without any BN, and CO was still seen in the product gas. The authors claimed that in spite of this, reaction *6.1* overrides all other processes in the system.

Castellano *et al*. [21] looked further into the behaviour of BN, and the different types of grade "A" BN (containing 5-8 wt% B_2O_3) and pyrolitic BN (free of B_2O_3). When either type was used, a small amount of nitrogen was found in the product gas. This was only observed during electrolysis, gas samples taken before or after electrolysis did not contain any nitrogen. When grade "A" BN was used, the current efficiency was higher than in its absence. The difference in the measured current efficiency was approximately proportional to the exposed BN area, and decreased when the BN was used repeatedly. The reaction of the boric oxide with aluminium by reaction *6.3* was shown to be the likely cause for this, because this reaction consumed some of the dissolved metal in the electrolyte. This meant that the back reaction was slowed down, and the apparent current efficiency calculated by gas analysis increased.

$$B_2O_3 + 2Al = 2B + Al_2O_3 \tag{6.3}$$

The decrease in current efficiency with successive use of the same piece of BN was attributed to a diminishing supply of B_2O_3, as it is readily soluble in cryolite.

The use of boron nitride pieces was very important in the design of the cell, to define the anode and cathode areas and shield some of the exposed carbon. Pyrolitic BN was used, so the occurrence of reaction *6.3* can be discounted. However it is possible that reactions *6.1* and *6.2* occurred during electrolysis, which would influence the current efficiency measurement. To check if this was the case, the gas analysis was used to determine if nitrogen was present in the product gas. Table 3.2 shows the fragment ion patterns for the various gases of interest in this study. Both N_2 and CO have their main peak at m/e = 28, and both

have an ion and/or fragment at m/e = 14. However the ion (N_2^{2+}) and fragment (N^+) at m/e = 14 have an intensity of 5-14% of the main peak for N_2, whereas the relative intensity for CO (CO^{2+}) is only around 1%. When experiments were performed, calibration of the mass spectrometer was made both before and after electrolysis. If reactions *6.1* and/or *6.2* do occur, then it will only be during electrolysis [21]. Therefore during calibration, when no nitrogen was present, the ratio of m/e 14 to 28 will be only due to CO. If any nitrogen is present during electrolysis, this ratio will increase.

Figure 6.4 shows the partial pressure of the peaks at m/e = 14 and 28. For clarity, only the data from during the CO calibrations and electrolysis is shown. Electrolysis was started at scan 140, and anode effect was reached at scan 230. The corresponding 14/28 ratio is shown in Figure 6.5. The ratio is only shown during calibration and electrolysis as there were other gases present at anode effect that made the ratio invalid.
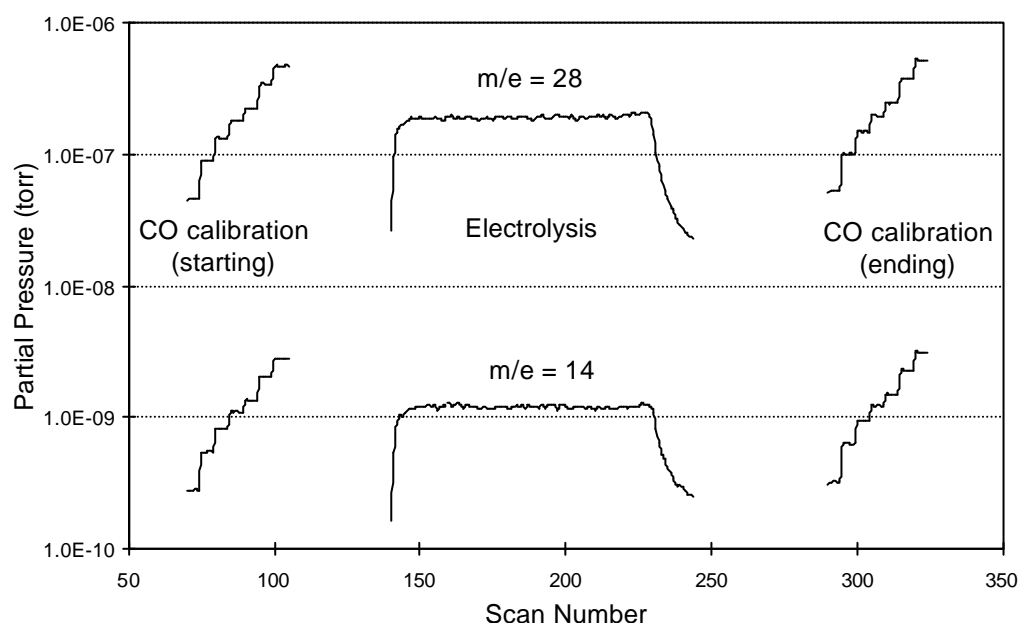
Figure 6.4 *Partial pressure at m/e = 14 and 28 due to carbon monoxide.*

There is some variation in the ratio during electrolysis, but the overall value is very close to that during calibration. Because the ratio is small, a small variation in the m/e = 28 partial pressure results in a large variation in the ratio. The ratio during electrolysis is not exactly the same as the calibrations, so the possibility of reactions involving boron nitride cannot be completely excluded. However the fact that the ratio is so close, combined with the very good agreement

between alumina concentrations calculated earlier, suggests that if there is any reaction with BN it is very minimal.
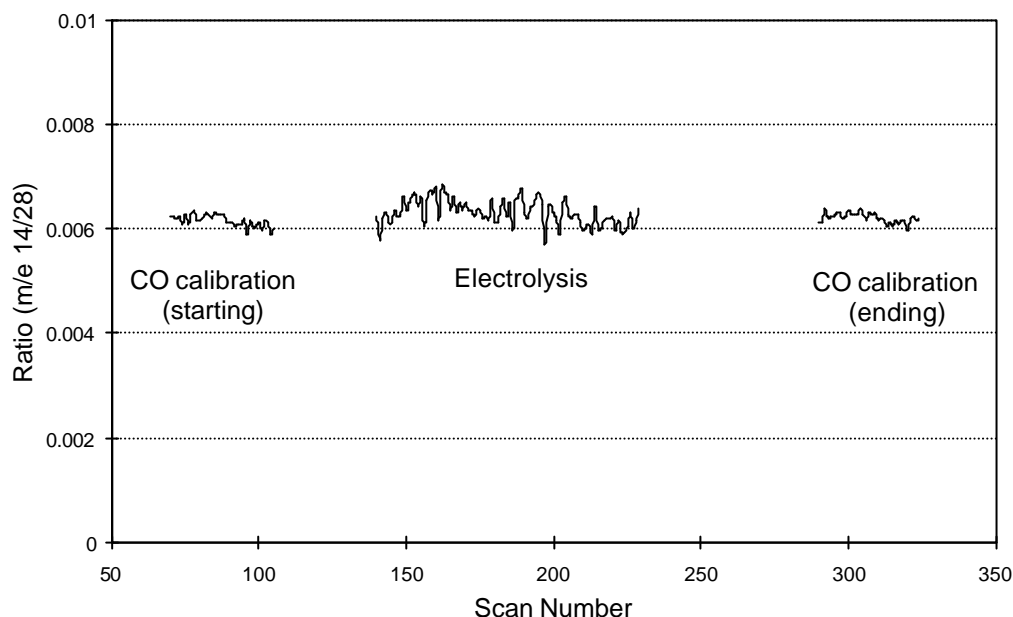
Figure 6.5 *Ratio of m/e 14/28 during carbon monoxide calibration and electrolysis.*

A comparison was made with the ratio of m/e 14/28 for gas with nitrogen present. When air was sampled, and other gas mixtures containing nitrogen as well as argon, oxygen and carbon dioxide, the ratio was between 0.0077 and 0.0083, considerably higher than the 0.0062 seen in Figure 6.5. The presence of nitrogen in the gas has an obvious effect on the ratio, further suggesting that the reaction of BN to form nitrogen as a byproduct can be discounted. Therefore if there is an influence on the derived current efficiency it will be very small, certainly no where near as high as the 12% reported by Castellano *et al.* [21]. One possible explanation for this disagreement is differences in the experimental set-up. In this study a cell current of 75 amps was used, whereas Castellano used only 4.5 amps. Although a smaller anode was used, their current density was also lower. Therefore the rate of primary reaction in this study was much larger, and if the BN was involved, the relative rate of reaction would be much less.

There was some other involvement of boron nitride, however this had no influence on the performance of the cell or the current efficiency measurement method as it was only at anode effect. This is discussed in section 8.2.4.

Water had to be considered also when determining the validity of the lower than normal current efficiency in the laboratory cell. If water was present in the product gas, this could be a source of oxygen not accounted for in the oxygen balance, resulting in an erroneously low current efficiency. However when the mass spectrometric data was examined, the partial pressure level at m/e = 18 (water) was found to be constant throughout the entire duration of the experiment. There was no increase during electrolysis, therefore no oxygen liberated from alumina escaped analysis by being bound as water, and the calculated current efficiency was not affected by water in the product gas. There also could not have been any extra water vapour released during the experiment that was initially absorbed on the alumina, as this would have been driven off during heating of the cell and eliminated before gas analysis began.

6.2.   The Influence of Cell Variables on Current Efficiency.

To further establish the performance characteristics of the cell, its behaviour with respect to cell variables was investigated, providing results in the form of correlations. As well as being results of the study, this also allowed comparison with previous findings to further confirm the validity of the current efficiency measurement method used.

6.2.1.   The Influence of Anode-Cathode Distance on Current Efficiency.

The influence of anode-cathode distance on current efficiency was studied in a series of experiments where the anode current density was 1.107 A/cm^2 (75 amps) and the cryolite ratio was either 2.39 or 2.33 (excess AlF$_3$ 8.19 or 9.0 wt%). The current efficiency and standard deviation are shown with ACD in Table 6.1.

Table 6.1 Influence of anode-cathode distance on current efficiency.

Anode-Cathode Distance (mm)	Current Efficiency (%)	Standard Deviation (%)
30	85.1	3.05
30	84.3	1.84
30	84.3	1.58
35	87.1	1.95

35	83.2	2.47
40	85.4	1.82
45	84.8	1.78

These results are presented graphically in Figure 6.6.
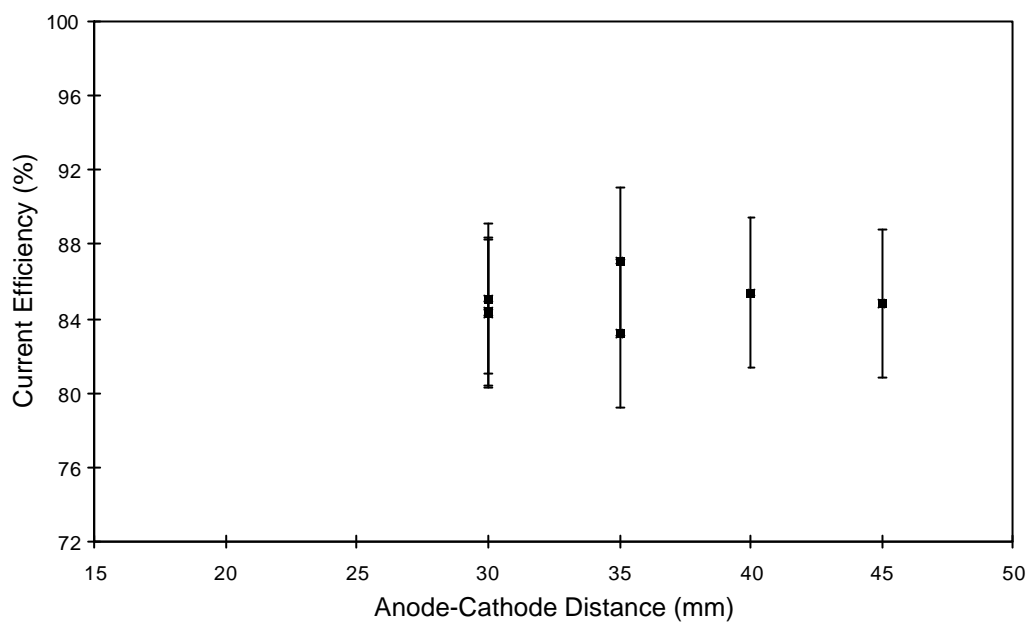
Figure 6.6 *Influence of anode-cathode distance on current efficiency.*

There is clearly no discernible effect of inter-electrode distance on the current efficiency, which was to be expected because of the design of the cell. With no metal pad in place at the start of each experiment, growing to a very small metal layer after electrolysis, there was no metal pad wave and mass transfer was gas-driven. Therefore the mass transfer conditions were the same at all the anode-cathode spacings used, and the current efficiency was not affected.

Previous studies of the influence of anode-cathode distance on current efficiency, reviewed in section 2.5.5, indicate no variation of current efficiency above a critical ACD. Below the critical ACD the current efficiency decreases rapidly. As seen in Figure 6.6, no attempt was made to determine if there was a limiting or critical electrode spacing, as this would have required much smaller electrolyte volumes resulting in shorter electrolysis times. One of the strong points of the method used is the ability to measure current efficiency over long electrolysis times, so a brief electrolysis period with a small ACD would result in a less precise current efficiency measurement.

6.2.2. The Influence of Current Density on Current Efficiency.

The influence of current density on current efficiency was studied in a series of experiments where the cryolite ratio was either 2.39 or 2.33 (excess AlF_3 8.19 or 9.0 wt%). The current efficiency and standard deviation are shown with current density in Table 6.2.

Table 6.2 Influence of anode current density on current efficiency.

Anode Current Density (A/cm^2)	Current (A)	Current Efficiency (%)	Standard Deviation (%)
0.295	20	71.3	2.55
0.295	20	69.2	2.75
0.554	37.5	77.0	2.11
0.554	37.5	76.1	1.96
0.856	58	80.9	2.82
1.107	75	87.1	1.95
1.107	75	85.4	1.82
1.107	75	84.8	1.78
1.107	75	83.2	2.47
1.107	75	84.4	1.84
1.107	75	84.3	1.58
1.107	75	85.1	3.05

The results are presented graphically in Figure 6.7. The trend of increasing current efficiency with increasing current density agrees with the findings of other studies, as reviewed in section 2.5.4. The increase in current efficiency is predominantly due to the larger ratio of forward to back reactions at the higher cell currents, however there is also more CO formed electrolytically at the anode at low current densities and the CO_2/CO ratio increases with increasing current density. However the trend in Figure 6.7, with a slope of 17.25 (linear fit R^2 = 0.9617) is at the higher end of range of laboratory studies shown by Grjotheim [33]. The large effect of current density on current efficiency may be accentuated by the mass transfer conditions present in the cell. At the lower current densities the aluminium produced will form into droplets more slowly, and there will be a greater ratio of surface area to volume, effectively providing a larger mass transfer area for the metal to dissolve.
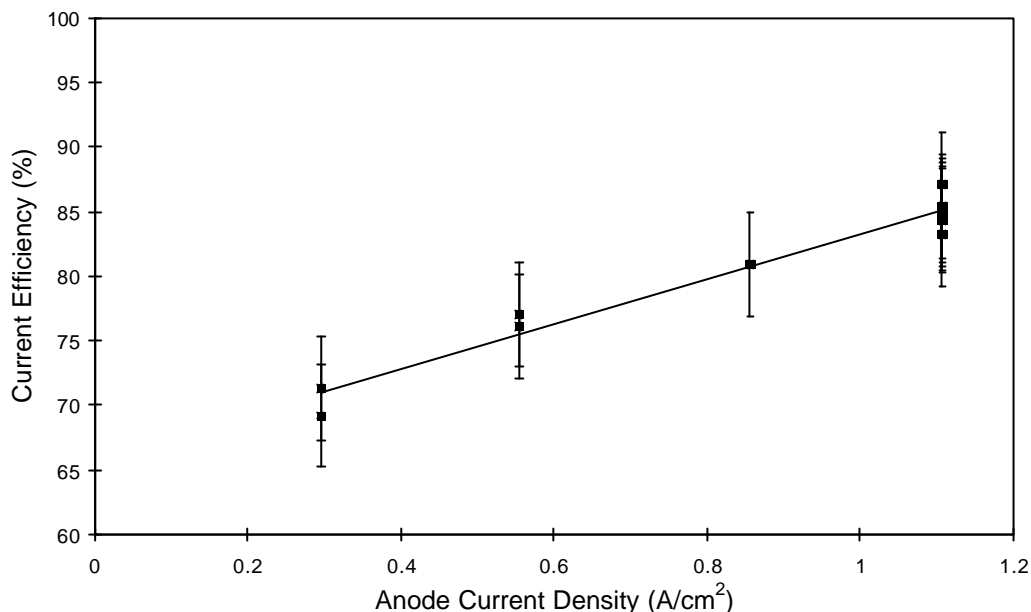
Figure 6.7 *Influence of anode current density on current efficiency.*

While a linear relationship is indicated in Figure 6.7, this is only within the bounds of the current density investigated and does not suggest a trend at either higher or lower current densities. In some of the previous studies reviewed in section 2.5.4, the current efficiency was found to drop off considerably at very low current densities. These very low current densities were not investigated in this study as at low cell currents the product gas concentration in the cell exit gas would be low, and the accuracy of the gas analysis reduced.

6.2.3. The Influence of Electrolyte Chemistry on Current Efficiency.

The cryolite molar ratio was varied at a constant current density of 1.107 A/cm^2 (75A) by changing the excess aluminium fluoride in the electrolyte. The extremes of electrolyte chemistry investigated were 0 and 15 wt% excess AlF_3 (cryolite ratio = 3, 1.98), with the majority of experiments at 8.19 and 9.0 wt% excess AlF_3 (cryolite ratio = 2.35). Because of the strong influence of excess AlF_3 in lowering the liquidus temperature, the experiments were carried out at different starting temperatures ranging from 936-980°C so the superheat was constant during the electrolysis period of each experiment at 15°C. With the resistive heating encountered, it was considered more important to maintain constant superheat than overall cell temperature.

103

Table 6.3 shows the current efficiency and standard deviation for the experiments with different excess AlF_3 contents. The results are presented graphically in Figure 6.8, clearly showing the strong relationship between electrolyte chemistry and current efficiency.

Table 6.3 Influence of electrolyte chemistry on current efficiency.

Cryolite Molar Ratio	Excess AlF_3 (wt%)	Current Efficiency (%)	Standard Deviation (%)
3.0	0.0	81.5	2.64
2.78	2.73	81.4	2.82
2.78	2.73	81.3	2.56
2.39	8.19	87.1	1.95
2.39	8.19	85.4	1.82
2.39	8.19	84.8	1.78
2.39	8.19	83.2	2.47
2.39	8.19	85.1	3.05
2.33	9.0	84.3	1.84
2.33	9.0	84.3	1.58
2.17	11.72	85.6	2.69
1.99	15.0	89.1	2.09
1.99	15.0	88.9	2.67

The linear correlation has a slope of -7.8% current efficiency per unit cryolite molar ratio (-15.6% current efficiency per unit weight ratio), with a fit of $R^2 = 0.8093$. This agrees very well with previous studies, the slope being almost identical to that of three different reports [27,44,45] reviewed in Table 2.4. The trend is well established, having being shown in many specific laboratory studies and also observed in smelters as a result of operational changes.
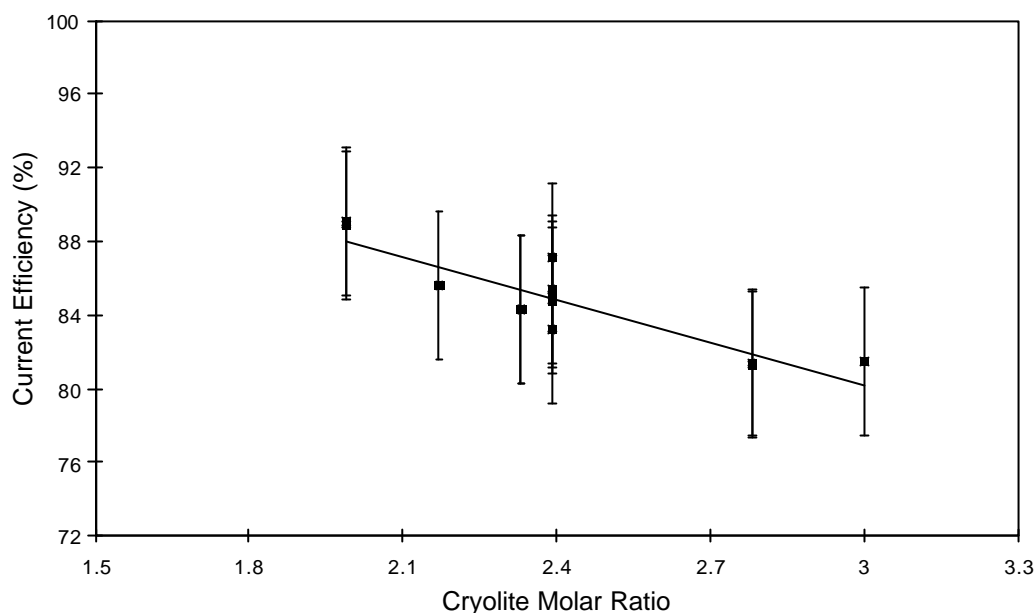
Figure 6.8 *Influence of electrolyte chemistry on current efficiency.*

The good agreement between the findings in this study and the established current efficiency - electrolyte chemistry, anode cathode distance and current density trends from previous laboratory and industrial studies further confirm the performance of the cell, and the accuracy of the method developed. This gives confidence in the use of the cell and method to investigate the relationship between alumina concentration and current efficiency.

6.3. The Influence of Alumina Concentration on Current Efficiency.

The technique, described in detail in chapter 5, involved measuring current efficiency as a function of time as the alumina concentration was depleted from its initial value and electrolysis continued until an anode effect occurred. From a knowledge of the initial mass of electrolyte and alumina, and also of the analysed final alumina concentration, the total number of moles of alumina electrochemically consumed could be calculated. This gave an integrated overall measure of current efficiency for the duration of each experiment. For the series of experiments conducted, the integrated instantaneous values of current efficiency compared well with the values determined by the alumina depletion. As the current efficiencies were shown to be constant during each experiment, the change in alumina concentration was calculated as a linear depletion.

The following three figures show current efficiency plotted against alumina concentration for the experiments performed. The experimental conditions are those found in Tables 6.1-6.3. The differing conditions are irrelevant as each experiment was used to determine the trend of current efficiency with alumina concentration rather than the absolute value of the current efficiency. For each curve, electrolysis started at the high alumina concentration, the current efficiency increased to a steady value, and proceeded to anode effect at the low alumina concentration.
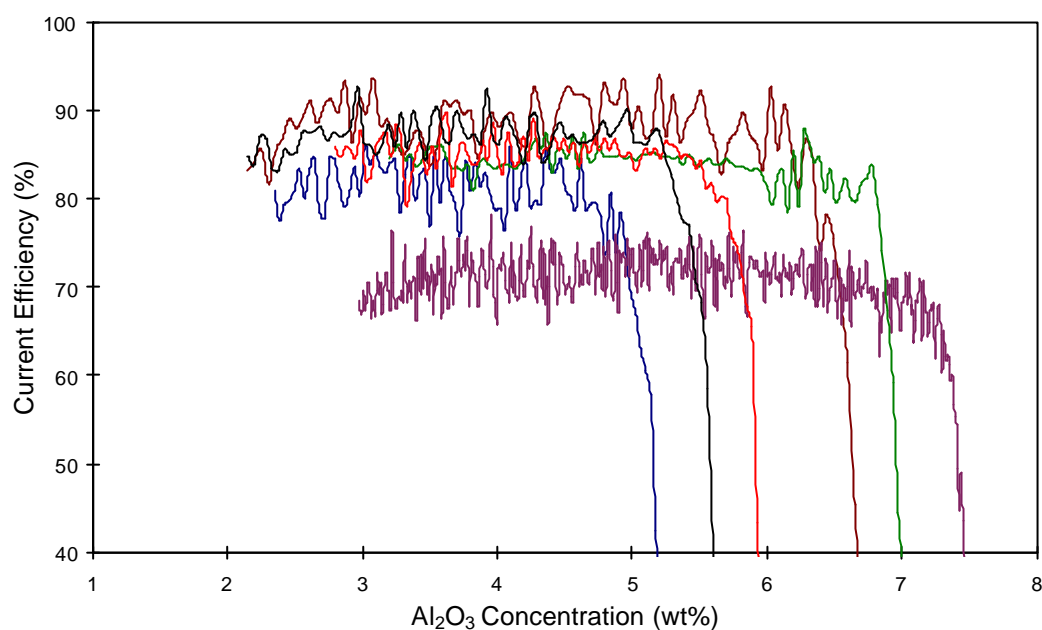
Figure 6.9 *Current Efficiency vs Al$_2$O$_3$ Concentration (runs a-f).*
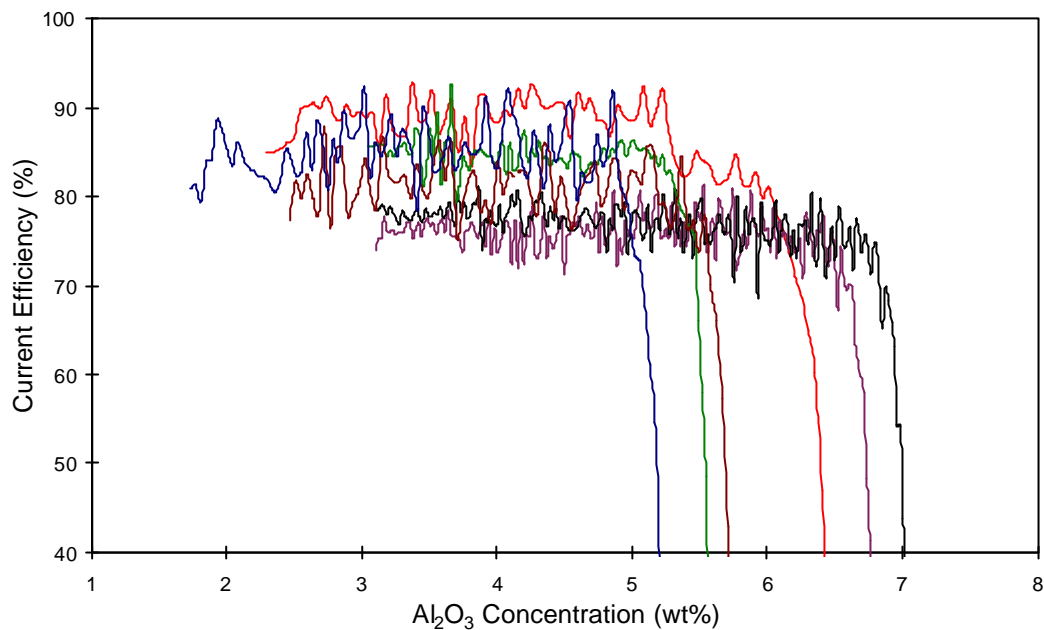
Figure 6.10 *Current Efficiency vs Al₂O₃ Concentration (runs g-l).*
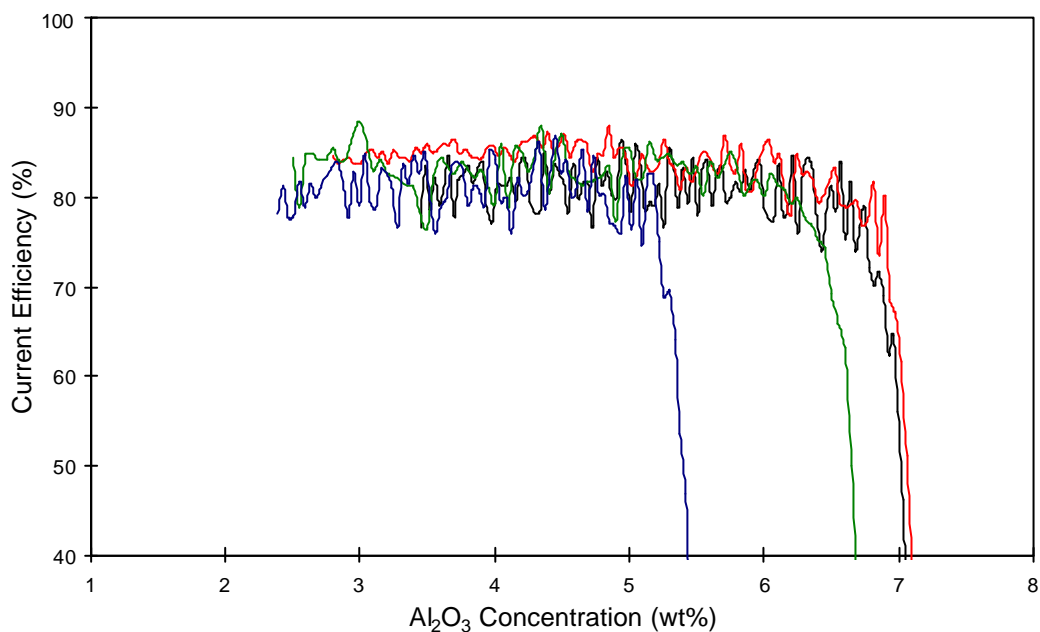
Figure 6.11 *Current Efficiency vs Al₂O₃ Concentration (runs m-p).*

Linear fits were made excluding the initial start-up period. For the experiments with cell current of 75A, the first 10 minutes were excluded. For 58A, 20 minutes were excluded, 30 minutes for 37.5A and 40 minutes for 20A current. In this way the start-up period was kept consistent with the integral current passing through the cell.

The numerical values are presented in Table 6.4, giving the average current efficiency, the standard deviation around the average, the rate of change of current efficiency with alumina concentration, and finally the alumina concentration range over which each experiment was carried out.

Table 6.4 The Influence of Alumina Concentration on Current Efficiency.

Current Efficiency (%)	Std. Dev. (%)	$dCE/dCAl_2O_3$ (%/wt%)	Al_2O_3 Concentration (wt%)
80.9	2.82	+0.1789	7.1-3.2
81.5	2.64	+0.0181	5.3-2.3
88.9	2.67	+0.4715	6.8-2.1
89.1	2.09	-0.5934	6.5-2.3
71.3	2.55	-1.0964	7.5-2.0
76.1	1.96	+0.4193	6.8-3.1
77.0	2.11	-0.8464	7.1-3.1
84.3	1.58	-0.4443	7.1-3.2
84.3	1.84	-0.7810	7.2-2.8
83.2	2.47	-0.3260	6.8-2.5
84.8	1.78	-0.3341	5.6-3.0
85.4	1.82	+0.1590	6.0-2.8
87.1	1.95	+0.5201	5.7-2.1
81.3	2.56	+0.7045	5.5-2.3
81.4	2.82	+0.0846	5.8-2.0
85.1	3.05	+0.9654	5.3-1.7

Figure 6.12 shows the linear fits plotted on one axis, covering the range of 1.75-7 wt% Al_2O_3. While some of the slopes are positive and some negative, and there is no correlation between the direction of the slope and the absolute current efficiency.

To make a comparison between the different experiments, the fits are plotted in Figure 6.13 to show the change of current efficiency as the alumina concentration varies above and below a nominal value of 4.5 wt%. Even the largest slopes give rise to a change in current efficiency of less than 6% over the wide alumina concentration range covered.
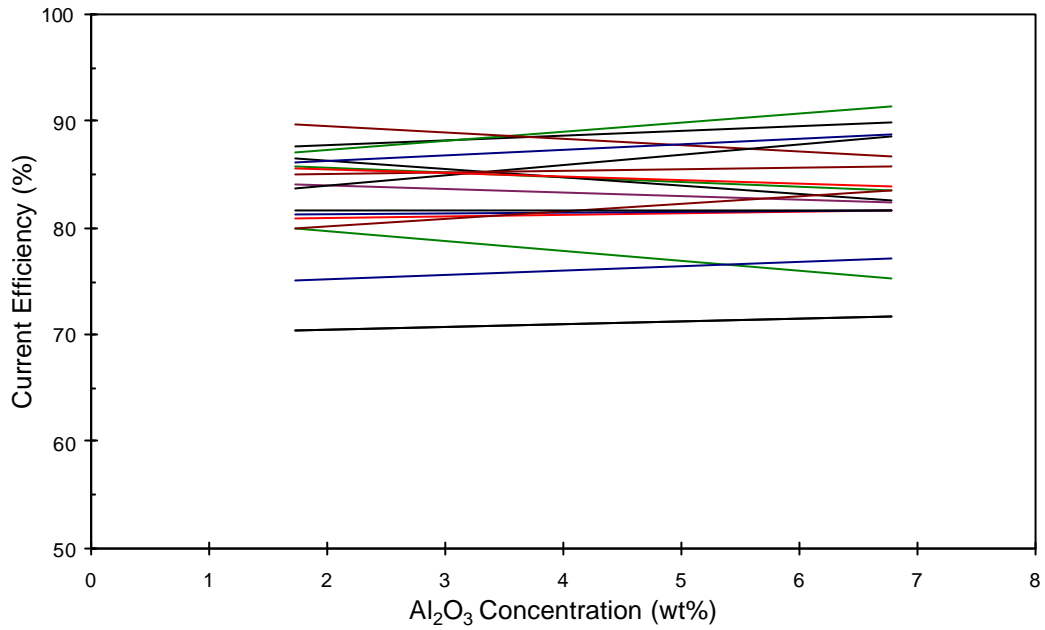
Figure 6.12 *Current Efficiency - Al₂O₃ Concentration Linear Fits.*
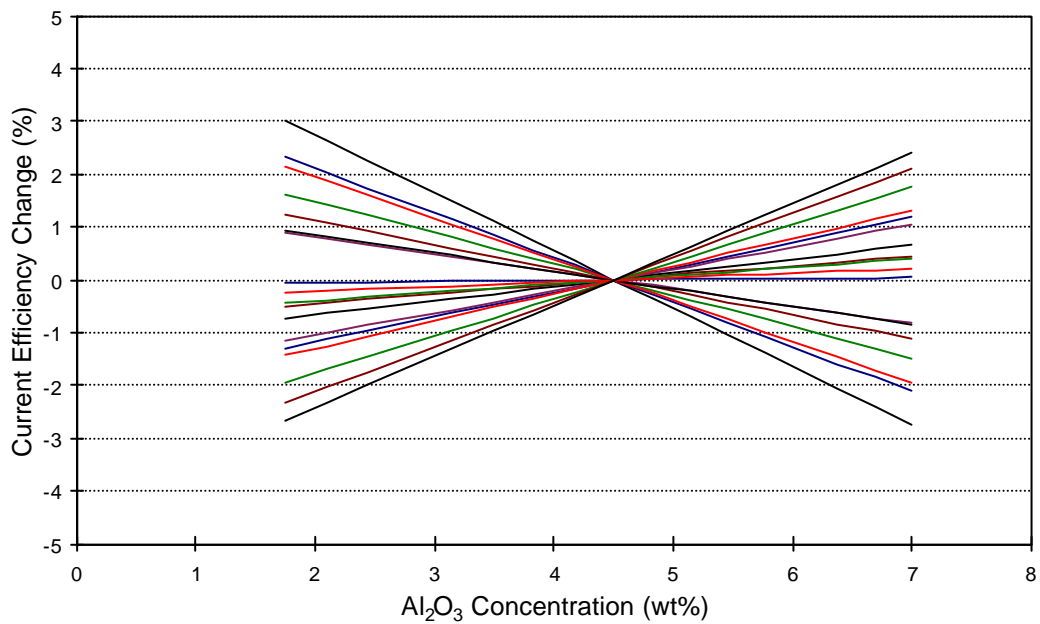
Figure 6.13 *Change of current efficiency with varying alumina concentration.*

The overall average value of the linear fits is -0.0376 %CE / wt% Al_2O_3, with a standard deviation of 0.5864. Figure 6.14 shows the comparison of these results to those found in the studies reviewed in section 2.5.2. The average value is shown as the central bold line, and the standard deviation is shown by the dotted lines. Apart from the Solli *et al.* study [30], only one of the previous studies [26] falls within the range found by this study. The other studies

reviewed show a much greater current efficiency dependence on alumina concentration. The findings of this study agree with those of Solli *et al*. [30], showing that there is effectively no influence of alumina concentration on current efficiency.
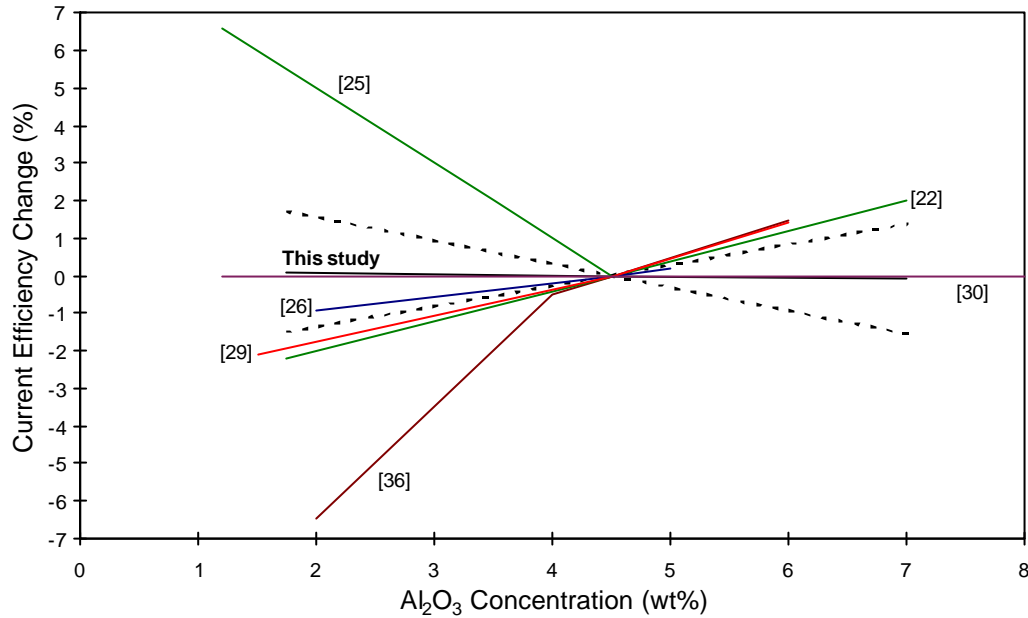
Figure 6.14 *Comparison to literature values for the alumina influence on current efficiency.*

A possible explanation for some researchers finding positive effects of alumina concentration on current efficiency and others negative can be found when the lowest curve in Figure 6.9 is examined. If the current efficiency is only considered between 3 and 4 wt% alumina, a slightly positive influence is indicated. However, if the response between 6 and 7 wt% alumina is examined, a slightly negative influence is seen. Thus interpreting data over a limited alumina concentration or time basis can lead to differing slopes because of the inherent standard deviation in the response. Previous studies illustrating this well are those by Grjotheim *et al*. [35] and Lillebuen and Mellerud [37], whose results are shown in Figures 2.9 and 2.10 respectively (section 2.5.2). In both cases a current efficiency minimum was shown with respect to alumina concentration, which could clearly be interpreted as a positive or negative effect of alumina if the alumina concentration range on only one side of the minimum was used.

Another explanation for differing current efficiency - alumina concentration relationships is the cell stability, especially for studies conducted on industrial cells. Stability was not a factor in

110

this study, as the cell was stable under all conditions tested. The studies shown in Figure 6.14 were carried out at different conditions, and as such it is possible that there could be interactions between different factors leading to the different trends seen. However in each of these studies the effects of other factors were taken into account, so the trends shown are due to alumina alone. It is possible that in studies on industrial cells, a changing alumina concentration does not directly cause a change in the current efficiency, but rather causes a change in the level of stability, therefore indirectly impacting on the efficiency. An example is the strong negative effect of alumina found by Leroy *et al.* [25], which led to cells being operated at low alumina levels. This gave high current efficiencies, although they could have also been due to the stable cell control, and associated low sludge formation and controlled anode effect frequencies. Another example of this is seen when Figure 2.13 from Alcorn *et al.* is examined.
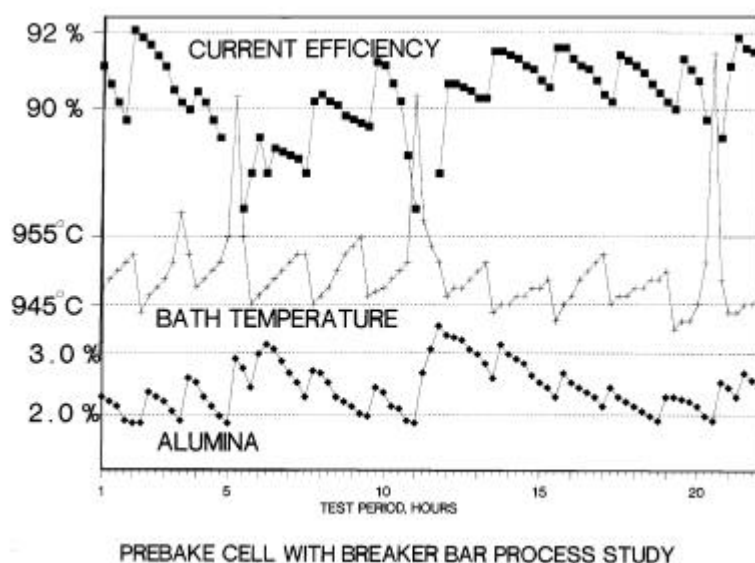
Figure 2.13 *Current efficiency of prebaked cells [26].*

In this current efficiency *vs* alumina concentration plot for a prebaked cell, there is a marked short term trend of decreasing efficiency with decreasing alumina concentration, which coincides strongly with the corresponding increasing temperature during each feeding phase. However, looking at the current efficiency over a wider time period shows the opposite trends. Between 1 and 11 hours, there is a general increase in alumina concentration and a decrease in current efficiency. From 11 hours onwards, the trend is reversed with a decrease in alumina concentration and an increase in current efficiency. For the alumina concentration to

111

steadily increase the cell must have operated with overfeeding, a period when sludge was likely to have formed. Sludge formation has a negative effect on cell stability, unsettling the metal pad and also changing the anode effect frequency [94]. It is possible this caused, or at least significantly contributed to the decreasing efficiency seen. The same applies to the period of increasing current efficiency, when the cell must have operated with underfeeding, ensuring that all the sludge was dissolved and the cell stability improved.

It also seems that the large difference in results from the different studies can be attributed to the similarly large difference in experimental conditions. Some studies were on laboratory cells, others on industrial cells of prebaked, VS and HS Söderberg design, others being models. Several of the studies utilised gas analysis and some form of the Pearson-Waddington equation [26,29,35,36], the shortfalls of which have already been discussed. Therefore the results are likely to be different because of different gas sampling and handling techniques and differing levels of reactions affecting the CO/CO_2 ratio, especially the Boudouard reaction. Another significant difficulty with all of the studies on industrial cells is the ability to isolate the effects of different variables, which is added to by the often long time between measurement points. For example in the study by Paulsen *et al*. [29], measurements were made every 5 minutes in some cases, but generally every 10 minutes. Any current efficiency variation between the sampling times was not accounted for, which as shown by this study could be significant. The method used also draws question on the results, as in one series of measurements the cell temperature was allowed to vary, while in another series the anode-cathode distance was varied in an attempt to keep the temperature constant. Obviously these variations impact significantly on the cell performance, making it difficult to determine which of the variables, or in what combination, actually caused the changing current efficiency. The dynamics of an industrial cell mean that when current efficiency was being measured it is unlikely that there was no influence on it other than by alumina concentration.

The most significant finding of this study, of no influence of alumina concentration on current efficiency, implies that the alumina concentration is not the prime consideration when operating the cell. This agrees with the findings of Solli *et al*. [30], who attributed the lack of current efficiency dependence to the only very slight dependence of dissolved metal activity on alumina concentration. This means a changing alumina concentration does not significantly alter the

amount of dissolved aluminium, therefore the rate of back reaction and resulting loss of efficiency is also unchanged.

While the results show that alumina concentration does not have a direct influence over current efficiency, the appropriate alumina levels must still be maintained to avoid either sludge build-up or unnecessarily high anode effect frequencies. Where importance should be placed is on minimising the disruption to the cell through the alumina feeding process and maintaining stable conditions. The most likely disturbance from feeding is to the electrolyte temperature, which as shown in section 2.5.1 has a strong effect on current efficiency.

6.4. Summary.

The performance of the cell, determined with the oxygen balance method, was shown to be generally slightly lower than of industrial cells, because of the cell design. Parameter studies of the main cell variables were performed. No influence of anode-cathode distance was found, which was expected because of the lack of a metal pad in the cell. Current density was found to have a strong influence on current efficiency, at a rate of 17.25 %CE per A/cm^2, between 0.3 and 1.1 A/cm^2. The effect of current density below 0.3 A/cm^2 was not investigated, although a sharp decrease in efficiency would be expected. The influence of electrolyte chemistry on current efficiency was investigated by varying the excess aluminium fluoride content of the electrolyte. The effect found was -7.8 %CE per unit cryolite molar ratio, between cryolite ratio 1.99 and 3. The most important of the results of this study are those relating current efficiency to alumina concentration, because there is still debate as to the extent of this relationship. The current efficiency was measured between 1.75 and 7 wt% alumina, and the relationship found was -0.0376 %CE / wt%. This shows that effectively there is no influence of alumina concentration on current efficiency over the normal alumina concentration range found in industrial cells.

7.   Components of Cell Voltage.

While there is considerable literature focusing on the voltage drop across aluminium cells, especially the decreasing energy requirements with improving technology, there is somewhat less information on the individual components making up the total cell voltage.

In this study two different techniques were used to investigate the components of cell voltage, and in particular to determine the anode polarisation and alumina activity contributions to the overall cell voltage. The first technique utilised fast switching of the cell current and high frequency voltage measurement to separate the voltage components. The second technique involved measuring cell voltage during cell electrolysis, and calculating certain voltage components from correlations to leave the polarisation components remaining.

7.1.   The Current Interruption Method.

The cell polarisation was determined using a method very similar to that outlined in detail by Hyde and Welch [10]. Briefly, the cell is operated under normal electrolysis, with high frequency measurement of the cell voltage. The cell current is interrupted, and the resulting voltage decay is recorded. When the current is switched off, the ohmic component of the voltage disappears immediately, while the polarisation dies away because the energy of polarisation is released more slowly.

The current interruption method was performed over a range of anode-cathode spacings, and with different current densities, for an experimental setup where the alumina concentration gradually reduced from 6.5 wt% to 3 wt%. The current interruption was repeated several times at each anode-cathode spacing and current density to provide verification of the results.

An example of the voltage measurement for a single current interruption run is given in Figure 7.1. Between 0 and 20 seconds the current was at 75 amps, giving a current density of 1.107

A/cm^2. The saw-tooth type of voltage response corresponds to the formation and release of gas bubbles under the anode. This voltage response was highlighted because of the high voltage measurement frequency of 100Hz, detecting the sharp drop in voltage as each bubble was released. These voltage characteristics were not seen in the work described in earlier chapters because the frequency of measurement was lower, and also the measurements were averaged over 35 second periods.

Shortly before the current was switched off at 20 seconds, the frequency of voltage measurement was increased to 1000Hz. This captured the voltage immediately after the ohmic component was removed, which then decayed until a stable nernst value was reached. The difference between the first voltage reading after current termination and the Nernst voltage current gave the value of polarisation.
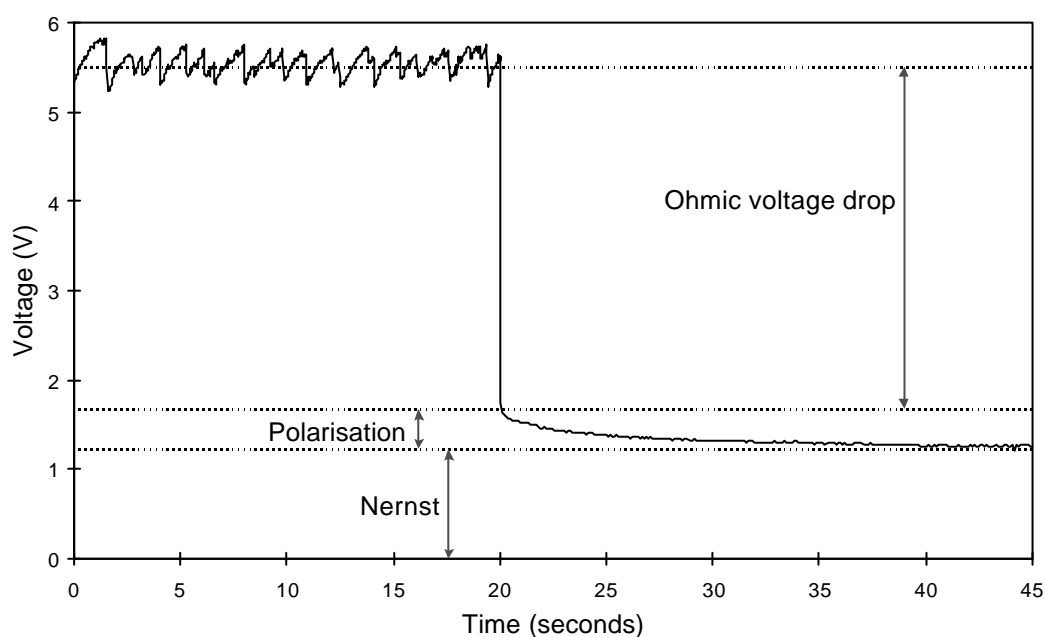
Figure 7.1 *Current interruption to determine components of cell voltage.*

To determine the ohmic resistance, the total voltage before current interruption was calculated by averaging the readings over the 20 seconds of measurement where the bubble formation and release was evident. The cell resistance was then calculated from the total cell current.

The results of the measurements are summarised in Table 7.1, giving the total voltage, ohmic voltage and resistance, the nernst potential and the polarisation.

115

Table 7.1 Polarisation measurements from current interruption.

| Al$_2$O$_3$ (wt%)	ACD (mm)	I (A/cm^2)	Total (V)	Ohmic (V)	R (Ω)	Nernst (V)	Pol (V)
6.5	30	0.295	2.732	1.111	0.056	1.252	0.369
		0.554	3.621	1.976	0.053	1.250	0.395
		0.856	4.686	3.045	0.053	1.239	0.402
		1.107	5.486	3.860	0.051	1.241	0.385
6	15	0.295	2.611	0.946	0.047	1.246	0.419
		0.554	3.265	1.605	0.043	1.244	0.416
		0.856	4.016	2.332	0.040	1.249	0.436
		1.107	4.650	2.956	0.039	1.244	0.450
6	20	0.295	2.672	1.007	0.050	1.241	0.424
		0.554	3.362	1.687	0.045	1.246	0.428
		0.856	4.186	2.487	0.043	1.249	0.450
		1.107	4.869	3.155	0.042	1.251	0.463
6	25	0.295	2.768	1.084	0.054	1.244	0.441
		0.554	3.534	1.820	0.049	1.251	0.463
		0.856	4.478	2.754	0.047	1.246	0.477
		1.107	5.247	3.523	0.047	1.244	0.480
5.5	35	0.295	3.158	1.440	0.072	1.248	0.471
		0.554	4.385	2.647	0.071	1.249	0.490
		0.856	5.883	4.159	0.072	1.233	0.491
		1.107	7.049	5.336	0.071	1.230	0.483
3.5	30	0.295	3.073	1.262	0.063	1.244	0.568
		0.554	3.957	2.146	0.057	1.244	0.568
		0.856	4.982	3.180	0.055	1.234	0.568
		1.107	5.830	4.048	0.054	1.229	0.553
3	35	0.295	3.520	1.592	0.080	1.230	0.698
		0.554	4.651	2.733	0.073	1.226	0.693
		0.856	5.895	3.995	0.069	1.230	0.669
		1.107	7.310	5.449	0.073	1.220	0.641

Theoretically, the Nernst voltage should be given by the equation:

$$E^{rev} = E^o_{Saturation} - \frac{RT}{6F} \ln \frac{a_{Al_2O_3}}{a_{Al_2O_3 Saturation}}$$

(7.1)

assuming the anode gas is constant (CO_2) and at a constant pressure (p = 1 bar). Since the saturation solubility of alumina is in the range 7 - 10 wt% for the electrolytes used, and the activity of alumina is expected to be approximately proportional to concentration in the range below 7%, the shift in Nernst potential is expected to be small. A decrease is to be expected, but only of the order of (RT/6F)ln(6.5/3) for the range of this study *i.e.* 15mV. The data of Table 7.1 is consistent with this, adding weight to the accuracy of the measurements.

On examination there is no significant effect of either current density or anode-cathode distance on the polarisation. The averages at 15, 20 and 25mm ACD suggest a very small increase in polarisation, however these measurements were made sequentially and as such there is a corresponding small change in alumina concentration. The change in polarisation is small, and it is not possible to differentiate between the influences of alumina concentration and ACD. The observed effect of current density is inconsistent, as at some alumina concentrations there is an apparent increase in polarisation with current density, whereas at others there is a decrease or no change. Therefore no conclusion can be drawn on the influence of current density. Contrasting, however, the cell variable exhibiting a significant influence over polarisation is alumina concentration, with a clear increase in polarisation as the alumina concentration decreases. To demonstrate this the alumina concentrations at each polarisation reading were calculated from a known starting alumina concentration. The polarisation is plotted against alumina concentration in Figure 7.2. The curve drawn through the data not of any particular function, and is indicative of the general increasing polarisation trend as the alumina concentration decreases.

This demonstrates the magnitude of the change in polarisation across the range of alumina concentrations that could be expected in an operating cell. If the curve is extrapolated to 2wt% alumina, a typical anode effect value, it can be seen that the total increase in polarisation from 7wt% would be between 0.5 and 0.7V. Given the accuracy of alumina analysis in commercial cells, this is consistent with the observations.
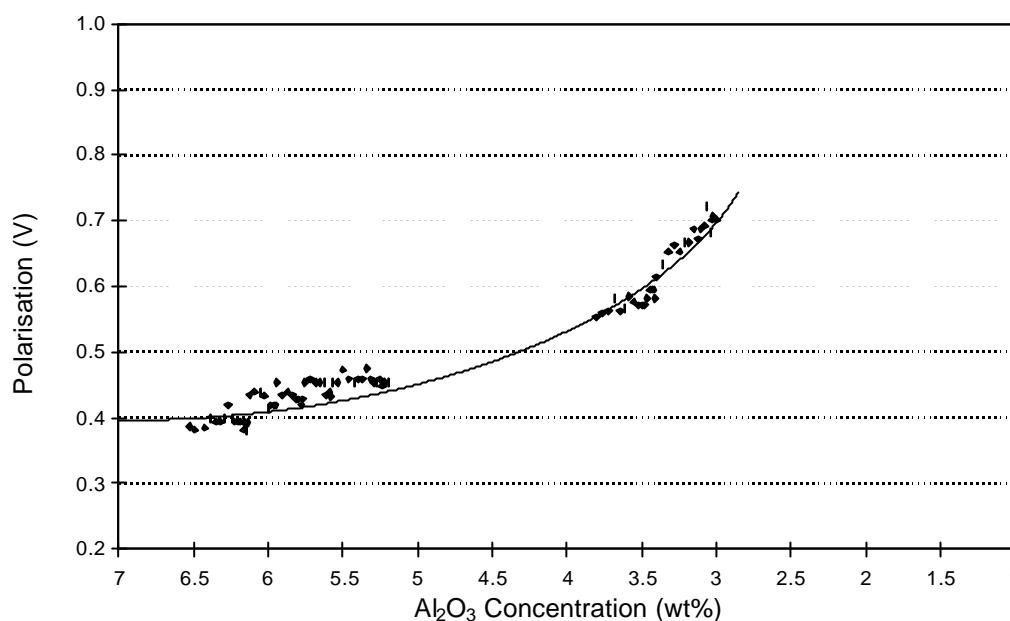
Figure 7.2 *Change in polarisation with alumina concentration.*

7.2.   Continuous Cell Voltage Measurement.

The cell voltage was continuously measured during all experimental runs for the current efficiency trials. For these runs the alumina concentration was determined before electrolysis began and after anode effect occurred by way of sampling the electrolyte. This allowed the voltage to be matched against the alumina concentration for the duration of electrolysis. Changes in alumina concentrations between these two limits could be calculated from current efficiency measurements. A typical cell voltage curve is given in Figure 7.3.

The overall value of cell voltage is very high, due to the voltage drop through the external circuit and the various connections to both anode and cathode. However the changes are only due to changes at the electrode interfaces and within the electrolyte. The general shape of the cell voltage curve was very repeatable over all of the experiments performed.   For all electrolysis, the voltage initially increased rapidly by about 0.3 to 0.6V, due to cell resistance and polarisation, before plateauing. This is common and attributed to the formation of NaC_x and/or Al_4C_3 layers on the electrode. These processes influence the curve for the first 30 minutes typically, but thereafter the changes are as expected from various resistance control

118

curves. Thus the changes in that part of the curve can be attributed to changes in parameters that influence the anode/electrolyte potential (or electrode polarisation).
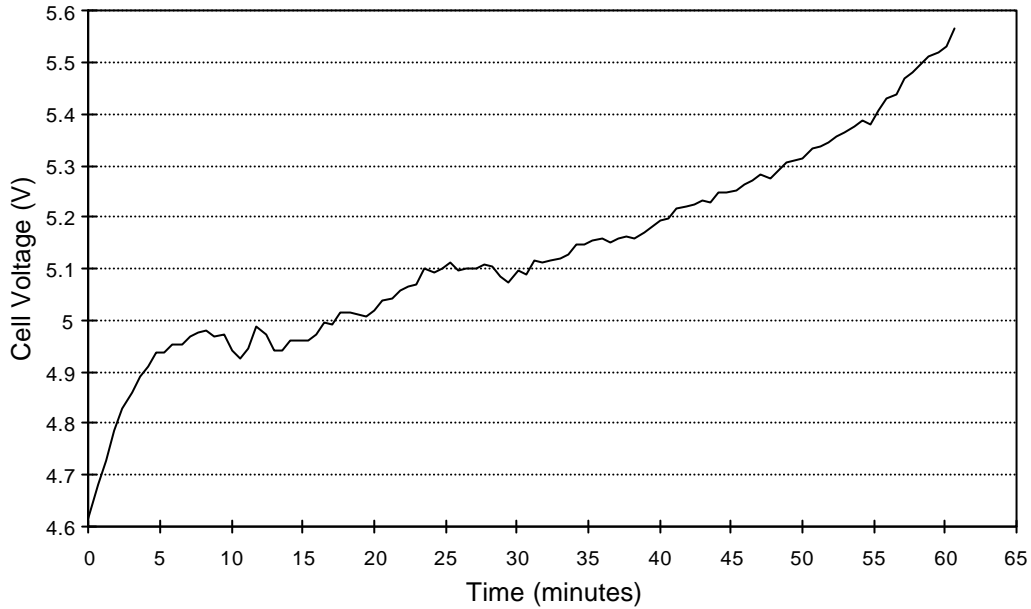
Figure 7.3 *Cell voltage during electrolysis up to anode effect onset*.

The cell voltage can be broken down into the various components, for more detailed investigation, by using the cell voltage equation:

$$V^{cell} = E^{rev} + \mathbf{h}_{an} + \mathbf{h}_{cat} + \mathbf{h}_{conc} + IR_{electrolyte} + IR_{bub} + IR_{cat} + IR_{an} + IR_{ext} \qquad (2.3)$$

To determine the anode reaction polarisation, three main voltage components were calculated.

The standard electrode potential ($E°$) was calculated from the Gibbs free energy of formation of both CO_2 and Al_2O_3 using equation *2.5*, taking a saturated solution for the standard state. The Gibbs free energies could then be interpolated to the cell temperature, which was measured simultaneously with the voltage.

The cathode polarisation ($\mathbf{h}_{cat}$) is known to be both small and dependent on the metal-electrolyte interfacial turbulence. In this case it was calculated with the Alcoa equation *2.8*. The cryolite ratio of the electrolyte was calculated using equation *2.2*, which took into account the changing alumina concentration during electrolysis.

119

The remaining contributions are dominated by the various ohmic values. The combined electrolyte and bubble voltage drops ($IR_{electrolyte}$) were calculated using equation *2.12* from Hyde and Welch [10]. The electrical conductivity term was determined with the correlation given by Wang *et al*. [12], while the electrode area was determined by considering the physical geometry of the cell.

When these three terms were calculated and subtracted, the remaining voltage consisted of the external ohmic voltage drop ($IR_{external}$) plus the anode polarisation and activity contributions ($\boldsymbol{h}_{anode}$), values that could not be calculated directly. The $IR_{external}$ term is comprised of the voltage drops across the external circuit, across the connections to anode and cathode as well as across the anode and cathode themselves. The $\boldsymbol{h}_{anode}$ term includes all terms that affect the anodic potential. It includes the anode reaction polarisation, concentration polarisation and alumina activity contributions to the overall cell voltage. The largest of these three terms is generally considered to be the anode reaction polarisation at normal alumina concentrations. However the concentration polarisation is included as it is small and difficult to calculate, and the alumina activity term is included because it is also small and there is uncertainty about its exact value (see section 2.2).

The cell voltage curve in Figure 7.3 is broken down into components and plotted in Figure 7.4. This highlights the anode reaction polarisation and external voltage terms, and shows the shape of the curve with increasing polarisation as anode effect was approached. During the last 12 minutes before anode effect began the voltage increase was typically 0.3V. The assumption behind this is that the external voltage did not change significantly during the electrolysis period, so the variation observed is all due to polarisation. The external voltage is not expected to vary, as the change in conditions such as electrode resistance is insignificant during electrolysis.

This method of breaking the cell voltage down into the individual components was applied to a series of voltage curves from experiments with different conditions. As mentioned earlier, the alumina concentration was measured at the start and end of each experiment, allowing the voltage to be plotted against alumina concentration rather than time, as above. This is demonstrated in the following Figures 7.5 to 7.9, each for groups of experiments with different

conditions. The individual curves making up each plot have been shifted vertically to account for different external voltages and highlight the shape of the voltage increase rather than the absolute values.
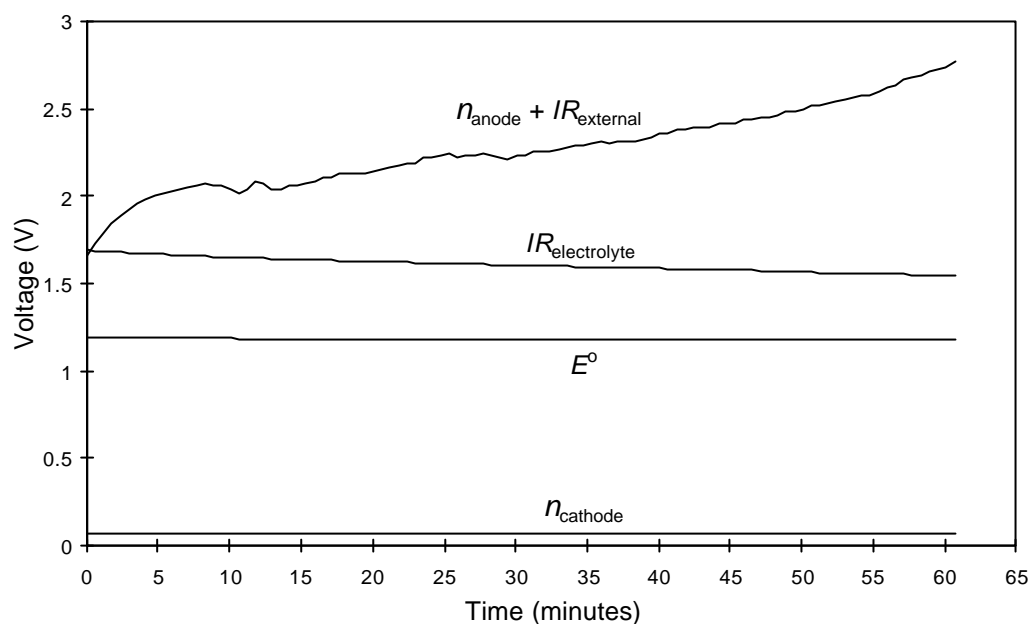
Figure 7.4 *Components of total cell voltage during electrolysis.*
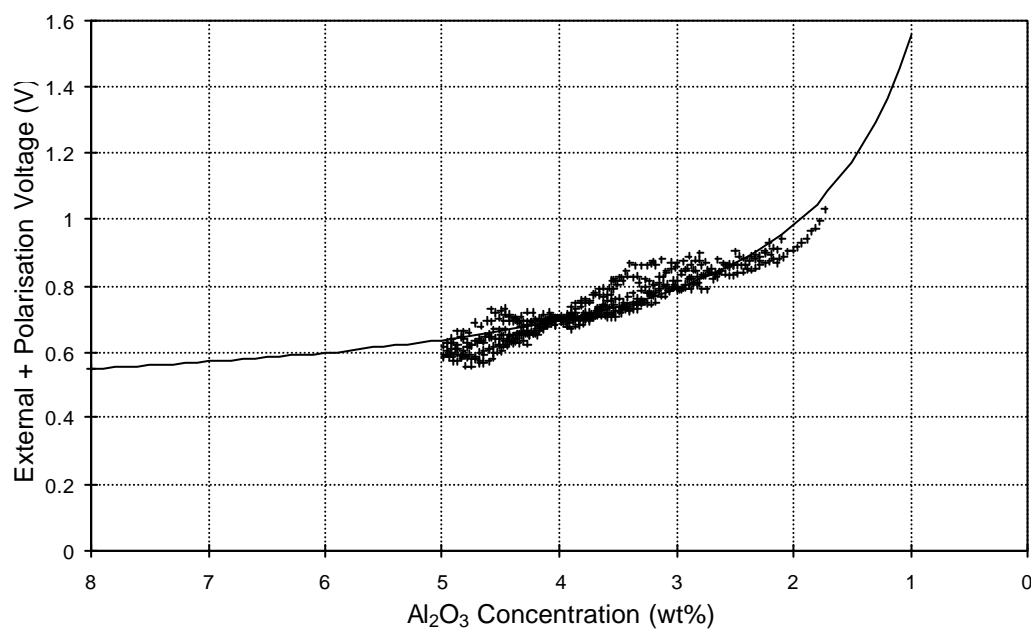
Figure 7.5 *External plus polarisation voltage (I=1.107A/cm^2, CR=2.33).*

121
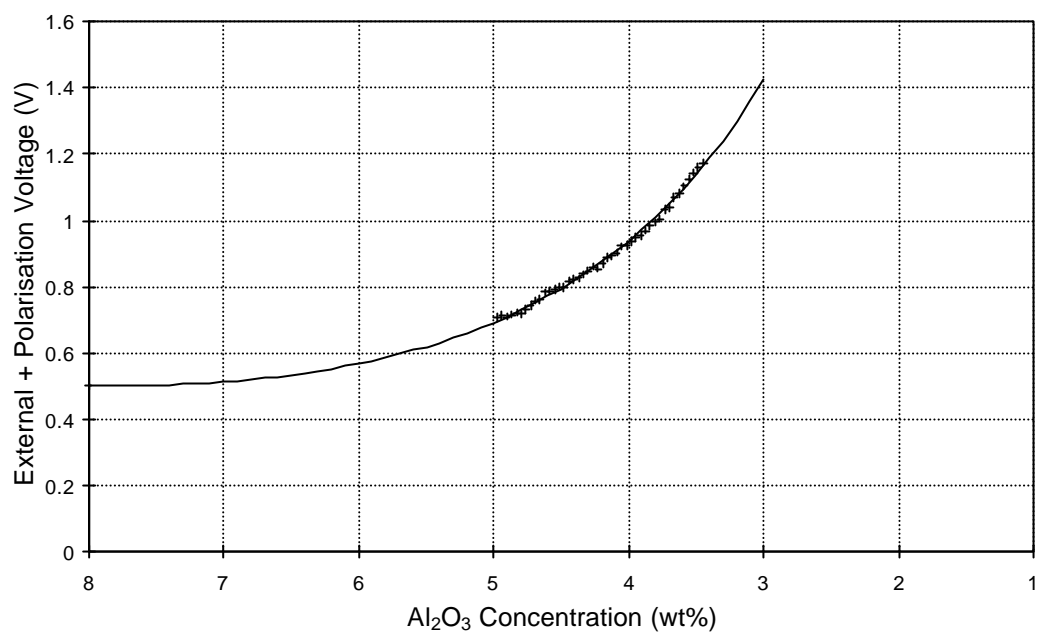
Figure 7.6 *External plus polarisation voltage (I=0.856A/cm², CR=2.33).*
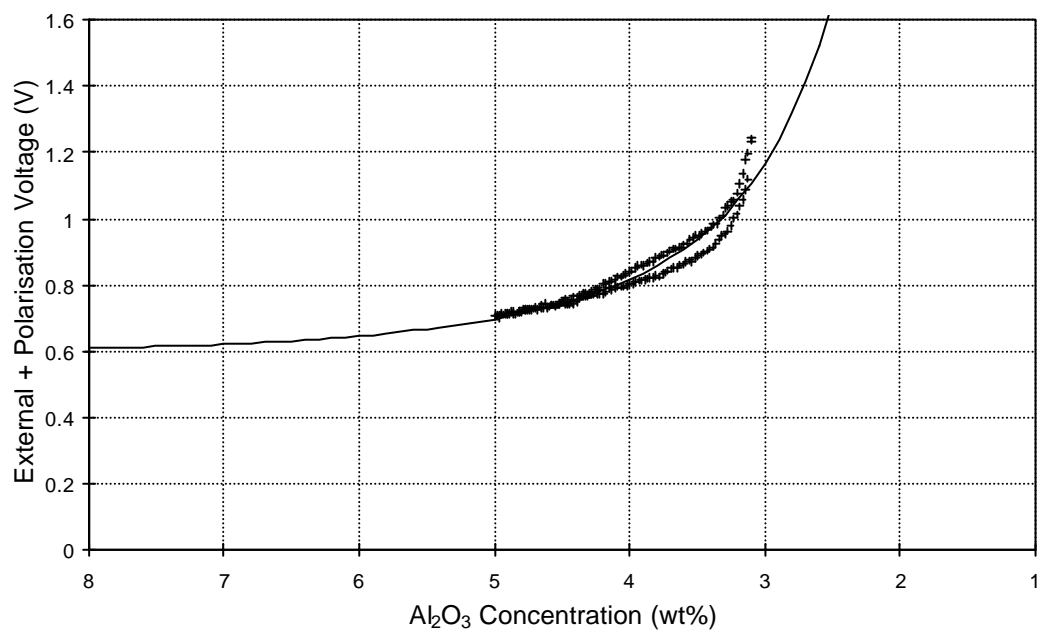
Figure 7.7 *External plus polarisation voltage (I=0.554A/cm², CR=2.33).*

122
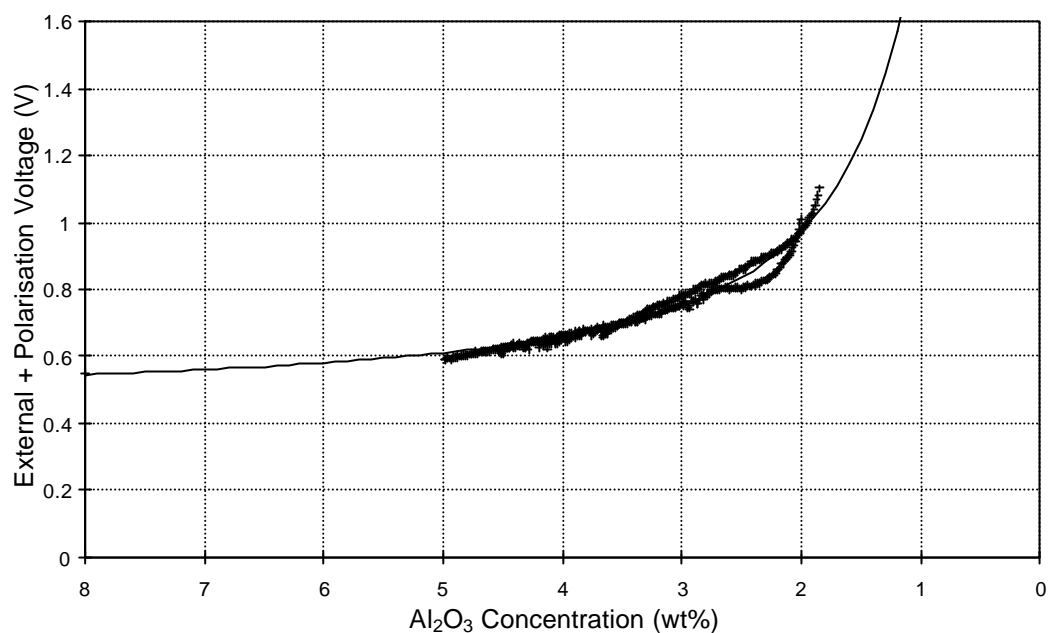
Figure 7.8 *External plus polarisation voltage (I=0.295A/cm², CR=2.33).*
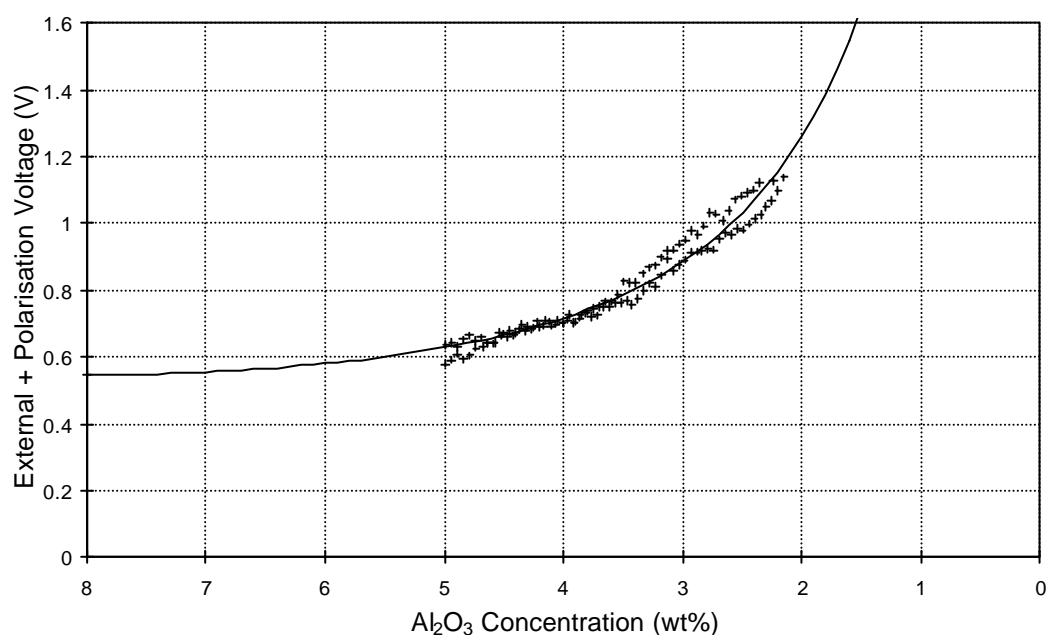
Figure 7.9 *External plus polarisation voltage (I=1.107A/cm², CR=1.99).*

The curves drawn through the data sets were then all plotted together, and were individually shifted along the x and y axes to account for differing external voltage drops and different anode effect alumina concentrations. The extrapolation of the curves at low alumina concentrations were also truncated to highlight the general trend of the data. The resulting

123

Figure 7.10 shows the similarity in the shape of the polarisation curve, as well as the magnitude of the polarisation change as the alumina concentration decreased.
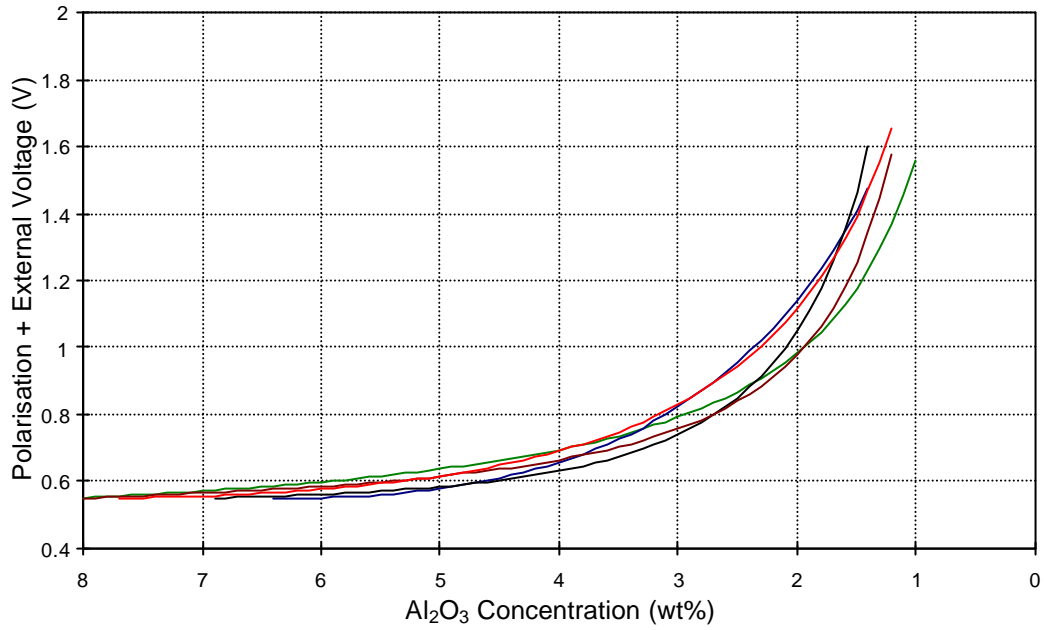
Figure 7.10 *Combined polarisation plus external voltage curves.*

A single curve representative of all the data, of the form $y = a + bx + c/x$, is given in Figure 7.11. The curve has been offset to start at zero volts for the saturated solution, and strictly this assumes no polarisation at the start of electrolysis. By also shifting the curve along the x-axis to end at zero wt% alumina the horizontal axis now represents the change in alumina concentration before anode effect rather than any specific alumina concentration values.
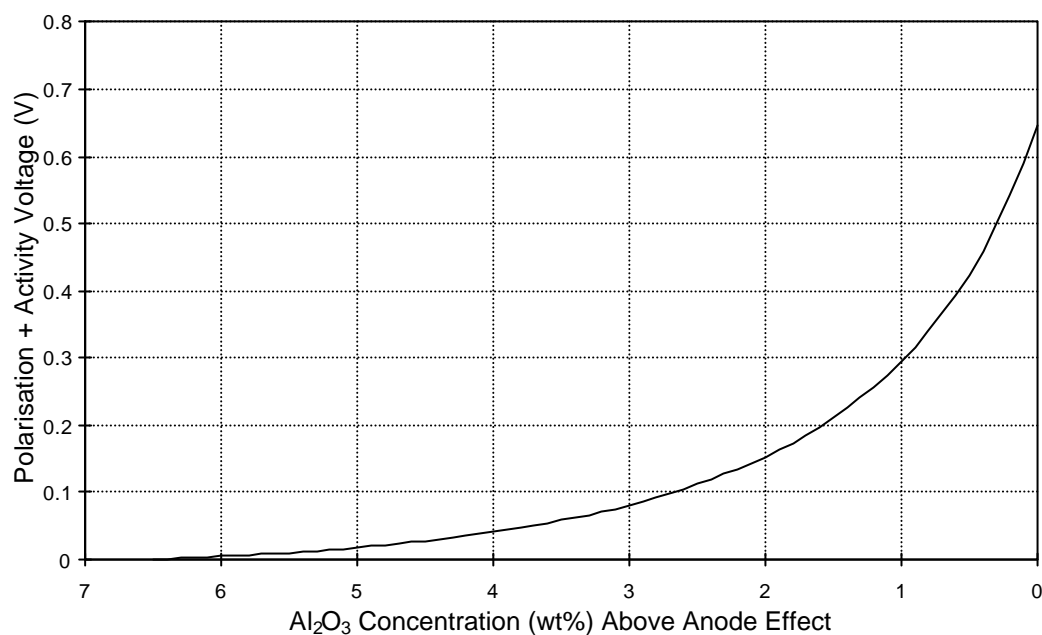
Figure 7.11 *Polarisation plus alumina activity contribution.*

The change in voltage along the y-axis is not as large as in Figure 7.10 because of the truncation of the curves at low alumina concentrations, so the curves ended at voltages similar to those measured rather than being artificially high. The curve in Figure 7.11 clearly highlights the total change in voltage due to polarisation plus alumina activity, until anode effect, as being up to 0.65V. The magnitude of the polarisation increase agrees more closely with the plant values rather than laboratory values found in Table 2.1 [9], likely to be because of differences in laboratory cell design.

The activity contribution to the cell voltage can also be determined using equation *2.7* from Rolin [6], with the index in the equation at 2.77, and also at 1 for comparison. These comparisons are plotted in Figure 7.12. Assuming the index to be 2.77, the activity contribution constitutes 0.09V of the total cell voltage. When the index is taken as 1, the activity contribution is correspondingly lower at 0.03V. However considering the alumina saturation dependant activity contribution with the index in equation *2.7* between 1 and 2.77, the value is small relative to the anode polarisation, which is alumina concentration dependant only. More importantly, the overall shape of the polarisation curve is unchanged, showing that the change in cell voltage due to polarisation and in small part to the alumina activity, is sufficient to initiate formation of fluoride species by reaction *2.39*, which is discussed in detail in chapter 8.
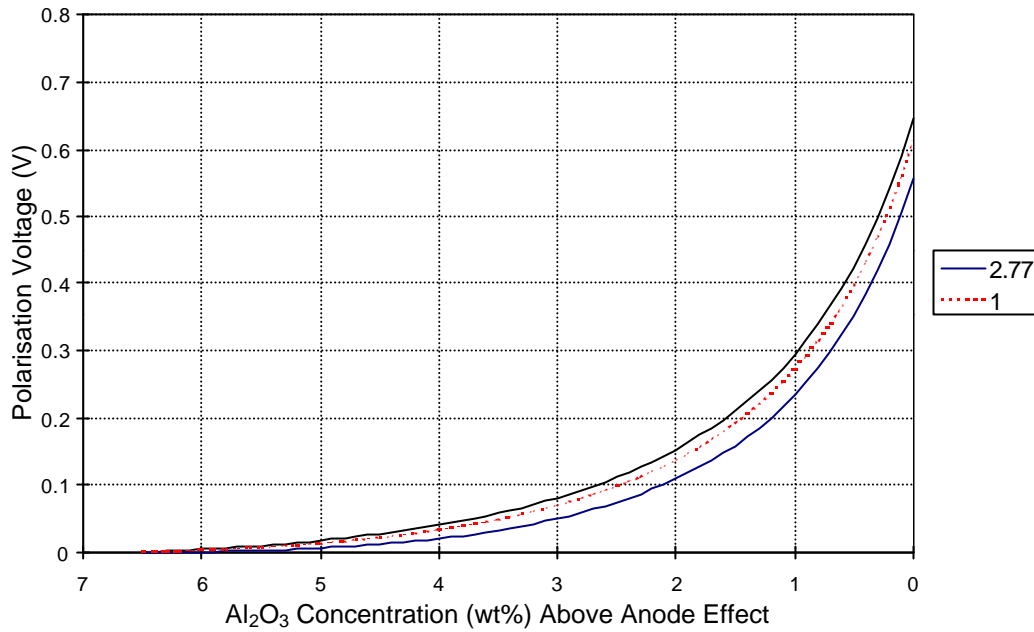
Figure 7.12 *Anode polarisation without the activity contribution.*

An important application of this method of breaking the cell voltage down into components is in the area of alumina feeding strategy, anode effect prediction and anode effect frequency reduction. If the characteristics of the increasing cell voltage are known, then the behaviour of a cell could be tracked and comparisons made between the measured and expected voltage. Obviously this would require significant measurement on industrial cells, and frequent standardising of the actual cell voltage measurements to allow for interferences and variations from the model. Overall this would allow the onset of anode effect to be anticipated, providing further input to the control of conditions in the cell and reducing the frequency of anode effect. The advantages of this are minimising the disturbance to the cell, and from a global perspective reducing the amount of fluorocarbons released into the atmosphere. It has even been suggested recently [95] that anode effects should be avoided altogether through a combination of monitoring of cell voltage, bath superheat and alumina concentration. This is based on the theory that the positive aspects of anode effect such as cleaning the cell of carbon dust are far outweighed by the negative aspects such as cell overheating and excessive energy loss.

126

7.3.   Summary.

This section has shown how two different methods were used to predict the shape of anode reaction polarisation *vs* alumina concentration curves, and the magnitude of the voltage increases.

The current interruption method allowed for direct measurement of the polarisation component of the total cell voltage. The change with alumina concentration was built up by repeated measurements with a changing electrolyte. This method showed the polarisation increase to anode effect to be in the range 0.5 - 0.7V.

The continuous voltage measurement method required the cell voltage to be broken down into the various components, which then identified the contribution from polarisation. Voltage curves from different experimental conditions were overlayed, and a representative curve fitted. Again the magnitude of polarisation increase up to anode effect was shown to be in the range of 0.5 - 0.7V.

The activity contribution to the total cell voltage as suggested by Rolin [6] was shown to be small, and did not have any significant effect on the shape of the voltage curve. The value of the index in the activity equation was also shown to have only a minor effect on the overall cell voltage.

8. Gas Evolution During Electrolysis and at Anode Effect.

This chapter outlines the findings of both experiments and thermodynamic modelling of the gases produced during normal electrolysis and through the transition into anode effect. Experimental measurements were made with the electrolytic cell and gas analysis system developed, in some cases the same experiment was used for investigating both current efficiency and the other gases formed in the cell at the same time. The thermodynamic modelling set-up conditions are given in detail, including both fluorine and sulfurous species. The predictions of fluorine species and experimental findings are discussed in this chapter, while the predictions of sulfurous species and corresponding gas analyses are covered in the following chapter.

8.1. Thermodynamic Predictions.

Predictions were made of the equilibrium composition of the cell product gas using the CSIRO Thermodata thermochemical modelling package. The basis of the technique was the standard free energy minimisation approach, calculating the equilibrium gas mix from a set of initial conditions. To allow comparison with previous studies, different oxidising conditions were considered, which also allowed for comparison with the findings from the experimental cell.

The three states modelling industrial cells were designated "unburnt", "partially burnt" and "completely burnt" gas, covering different zones in the cell, following the terminology and design of a previous study by Henry and Holliday [62]. The "unburnt" scenario modelled the initial gas formation underneath the anodes, where although CO formation by reaction *2.17* occurs at a lower potential, the higher oxidation potential through anode polarisation means that CO_2 formed by reaction *2.1* is favoured. The "partially burnt" scenario modelled the gas, after being released as bubbles from under the anode, trapped under the solid electrolyte

crust. This is a highly reducing zone where the gases are in contact with the solid anode carbon, and the temperature is between 600 and 950°C. There is also some permeation of air through gaps in the crust, allowing a small amount of oxygen to mix with the gas. The third scenario of "completely burnt" gas modelled the gas emerging through cracks and holes in the crust to burn as a flame with the drafting air. This combustion region provides a completely oxidised atmosphere and temperatures up to 1300°C. The laboratory cell was also mimicked, so the thermodynamic predictions could be matched against the gas analysis from the cell.

The initial conditions used for the thermodynamic predictions are given in the following tables 8.1 and 8.2. For normal electrolysis a high CO_2 to CO ratio of 10:1 was used, based on the typical ratio found in industrial cells. For anode effect the ratio was inverted to model the high proportion of CO found in cell gas. The other significant difference in the initial conditions to differentiate anode effect was the inclusion of CF_4 and C_2F_6. These gases, in a 10:1 ratio, were chosen as the way to introduce fluorine as they are known to be formed at anode effect [52,64]. The thermodynamic calculations then considered the possibility of other fluorine-containing species. In both electrolysis and anode effect, the anode was considered by including solid carbon in the initial conditions for all scenarios. Moisture present in the drafting gas of industrial cells was also considered by including a small amount of hydrogen in the initial conditions, with water included as a possible equilibrium species. HF was not included as it would not be detected in the laboratory set-up due to the alumina scrubbing system, and also because the predictions would not take into account the adsorption of HF onto alumina.

Some sulfur was included to model a high sulfur content in the anodes. One item of debate when setting up the initial conditions was the state and form of the sulfur. Sulfur is bonded in some way to carbon but it is generally considered that it will "desulfurize" if the anode is heated above 1350°C. Thus at lower temperatures the bonding will stabilise the reaction

$$C_xS_2 = xC + S_{2\,(g)} \qquad\qquad (8.1)$$
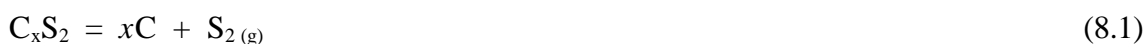
making the equilibrium pressure less than one atmosphere. Practically this can be handled by treating it as pure sulfur but at a reduced thermodynamic activity by assuming a low activity

co-efficient. This was done in preliminary calculations but it was found to have only a minor effect on the multiple equilibrium. Therefore the data presented is based on unit sulfur activity.

Table 8.1 Initial molar conditions (normal electrolysis).

Species	Laboratory Cell	Industrial Cell Unburnt	Industrial Cell Partially Burnt	Industrial Cell Completely Burnt
$CO_{2(g)}$	10	10	10	10
$CO_{(g)}$	1	1	1	1
$S_{2(g)}$	0.1	0.1	0.1	0.1
$O_{2(g)}$	0	1E-05	1	5
$H_{2(g)}$	0	0.5	0.5	0.5
$C_{(s)}$	3	3	3	3
$S_{(l)}$	0.2	0.2	0.2	0.2

Table 8.2 Initial molar conditions (anode effect).

Species	Laboratory Cell	Industrial Cell Unburnt	Industrial Cell Partially Burnt	Industrial Cell Completely Burnt
$CO_{2(g)}$	1	1	1	1
$CO_{(g)}$	10	10	10	10
$S_{2(g)}$	0.1	0.1	0.1	0.1
$CF_{4(g)}$	5	5	5	5
$C_2F_{6(g)}$	0.5	0.5	0.5	0.5
$O_{2(g)}$	0	1E-05	1	5
$H_{2(g)}$	0	0.5	0.5	0.5
$C_{(s)}$	3	3	3	3
$S_{(l)}$	0.2	0.2	0.2	0.2

The equilibrium gas concentration was calculated at intervals of 25°C from 1350°C down to room temperature, to cover the range from high temperatures where some reactions take place down to low temperatures where gaseous emissions are released into the atmosphere.

8.1.1. Thermodynamic Predictions: Electrolysis.

The predictions of the equilibrium gas composition during normal electrolysis for the different oxidation states are shown in Figure 8.1 to Figure 8.4.

The composition of the laboratory cell gas (Figure 8.1) consists of only CO and CO_2 as there was no other oxygen or hydrogen in the system. The levels of CO_2 and CO are similar until the equilibrium temperature drops below 700°C, when the Boudouard reaction *2.24* becomes less favoured and the CO_2 does not react with the carbon to the same extent. This is a trend apparent in all of the scenarios including at anode effect, except for completely burnt gas during electrolysis, when reactions with oxygen are dominant.

The introduction of some hydrogen and a small amount of oxygen causes hydrogen and water vapour to be present in the equilibrium gas mixture for unburnt industrial cell gas (Figure 8.2). At cell temperatures water is just favoured over hydrogen, and becomes even more favoured when further oxygen is added to model the partially burnt gas (Figure 8.3). In this situation the CO_2 becomes favoured over CO, although is not yet completely dominant.

The shift from partially burnt to completely burnt gas gives a very different equilibrium gas composition (Figure 8.4). Now CO_2 becomes the dominant species, there are lesser amounts of oxygen and water vapour present, and only a very small amount of CO is found at the higher temperatures.
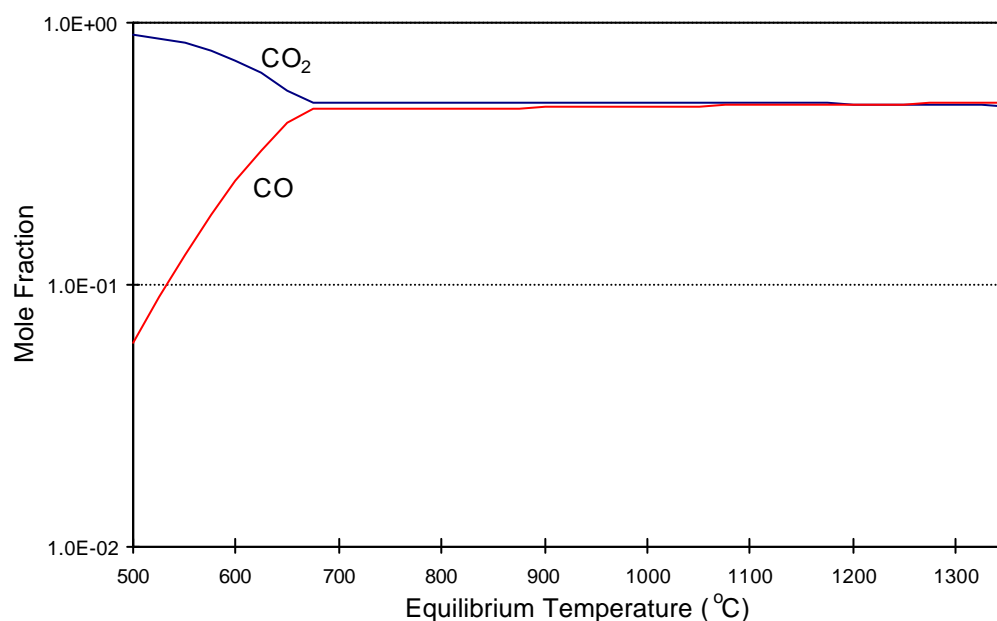
Figure 8.1 *Equilibrium gas composition: laboratory cell, electrolysis.*

131
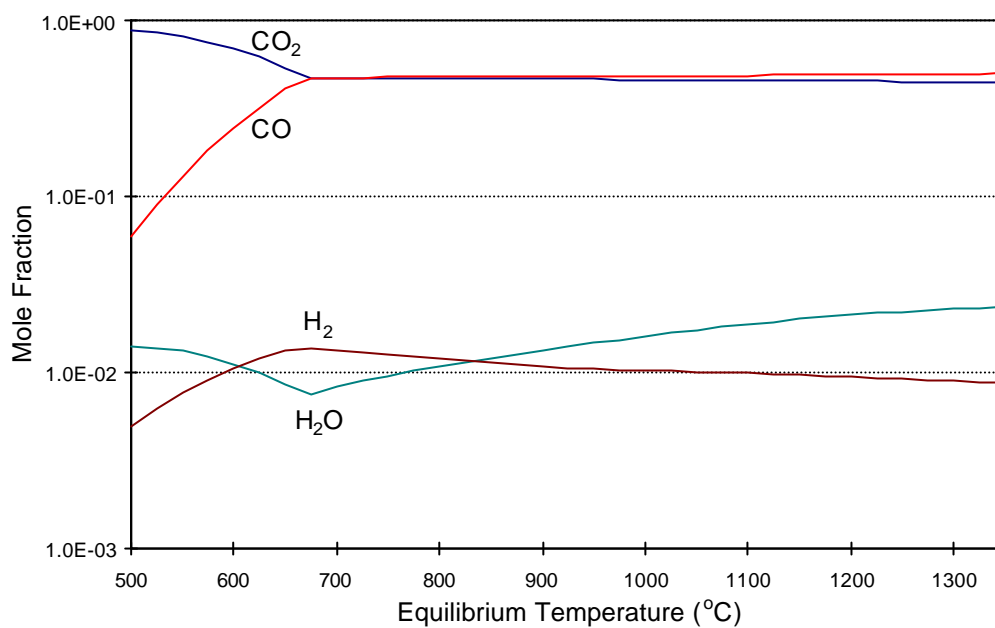
Figure 8.2 *Equilibrium gas composition: industrial cell (unburnt), electrolysis.*

Figure 8.3 *Equilibrium gas composition: industrial cell (partially burnt), electrolysis.*

Figure 8.4 *Equilibrium gas composition: industrial cell (completely burnt), electrolysis.*

The gas compositions at 975°C for the normal electrolysis scenarios are given in Table 8.3, demonstrating the trend of increasing CO_2 and decreasing CO concentration as the oxidation level is increased. This also suggests that the gas composition when formed under the anodes has similar levels of CO_2 and CO, and as the gas passes through the zones of increasing oxidation the CO reacts to form more CO_2.

Table 8.3 Equilibrium gas composition (mol fraction) at 975°C for electrolysis.

Species	Laboratory Cell	Industrial Cell Unburnt	Industrial Cell Partially burnt	Industrial Cell Completely burnt
CO_2	0.497	0.466	0.599	0.889
CO	0.479	0.484	0.351	2.0E-07
O_2	2.8E-15	2.4E-15	7.6E-15	0.054
H_2	0	0.010	0.007	4.5E-09
H_2O	0	0.015	0.019	0.032

These results establish the validity of the thermodynamic modelling, providing predictions that agree with the general expectation of higher CO_2 content in the more oxidised gas.

133

8.1.2. Thermodynamic Predictions: Anode Effect.

The following predictions of equilibrium gas composition at anode effect do not include any transition period from normal electrolysis, and also do not consider the elapsed time from the beginning of anode effect, which has been shown to be of importance to the concentration of gases evolved [64].

The anode effect composition for the laboratory cell (Figure 8.5) shows, as expected for a low oxidation scenario, high CO and low CO_2 concentrations. Also, in agreement with previous studies [52,64,65,67], CF_4 is the main fluorine containing species, with C_2F_6 present to a very low level. Importantly COF_2 is indicated in reasonable levels, showing it is a thermodynamically favourable equilibrium product. However it must also be considered that the predictions do not take account of any kinetic barriers to the formation of the various species.

The gas compositions for both unburnt industrial cell gas (Figure 8.6) and partially burnt industrial cell gas (Figure 8.7) are almost identical, and only vary significantly from the laboratory cell because of the presence of hydrogen and water vapour. There is not a significant difference from unburnt to partially burnt gas, because although the amount of oxygen in the initial conditions increased slightly, this was overridden by the high CO/CO_2 ratio in both scenarios.

Similar to the predictions for electrolysis, there is a significant change in the equilibrium composition with the completely burnt industrial cell gas (Figure 8.8). CO remains with the highest concentration, although it has decreased and CO_2 has increased to be just below CO. COF_2 is higher, and at cell operating temperatures is at similar levels to CF_4, with C_2F_6 only present in trace levels.
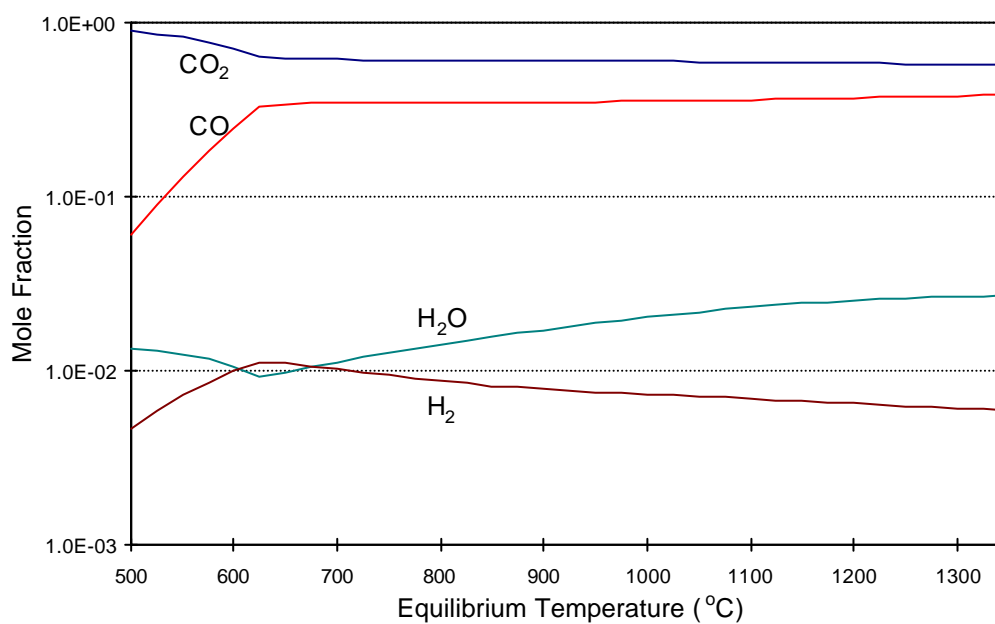
Figure 8.5 *Equilibrium gas composition, laboratory cell, anode effect.*
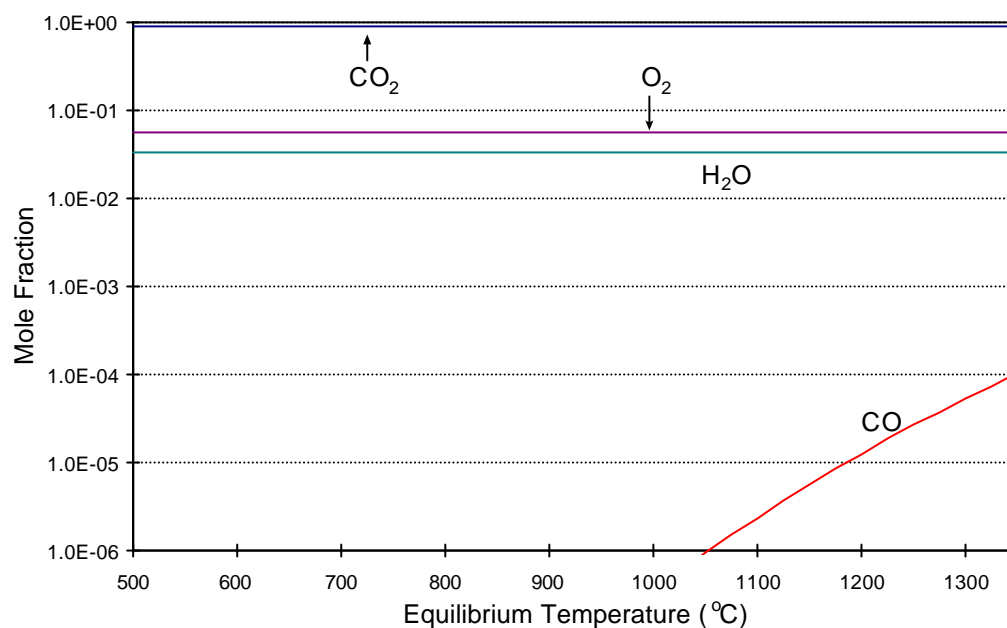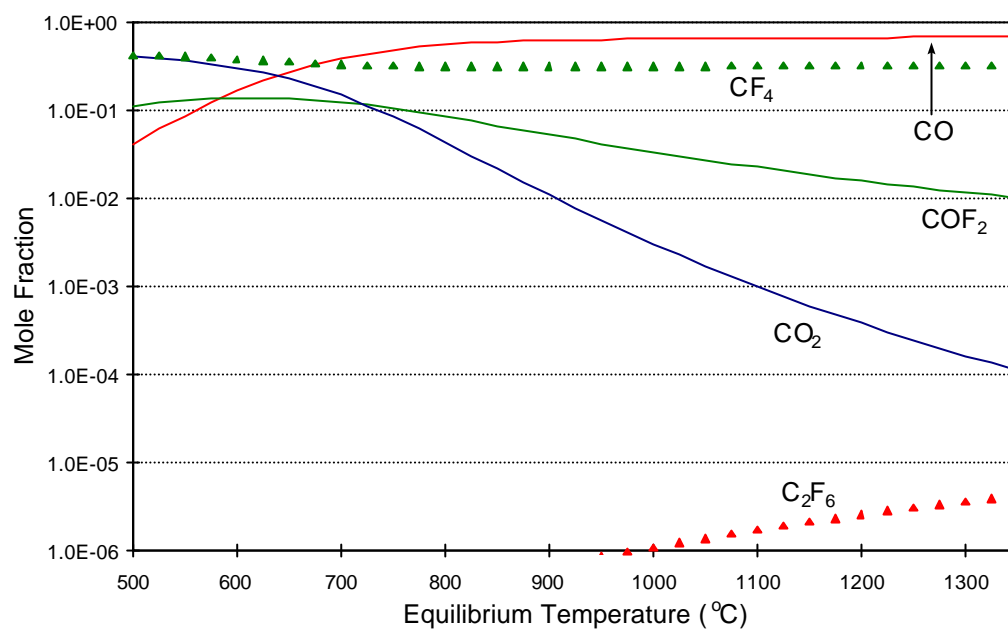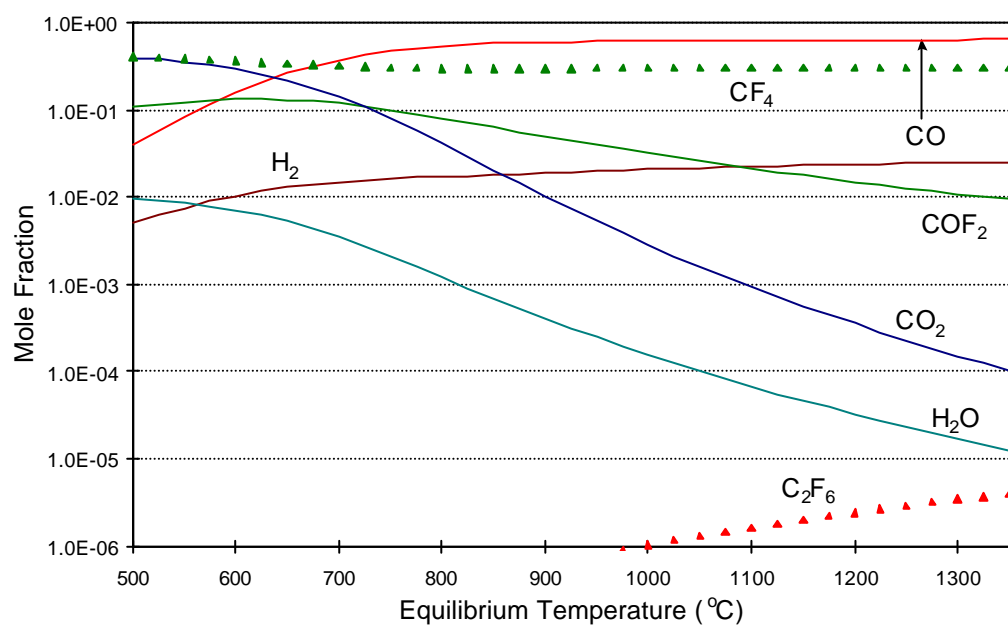

Figure 8.6 *Equilibrium gas composition: industrial cell (unburnt), anode effect.*

135
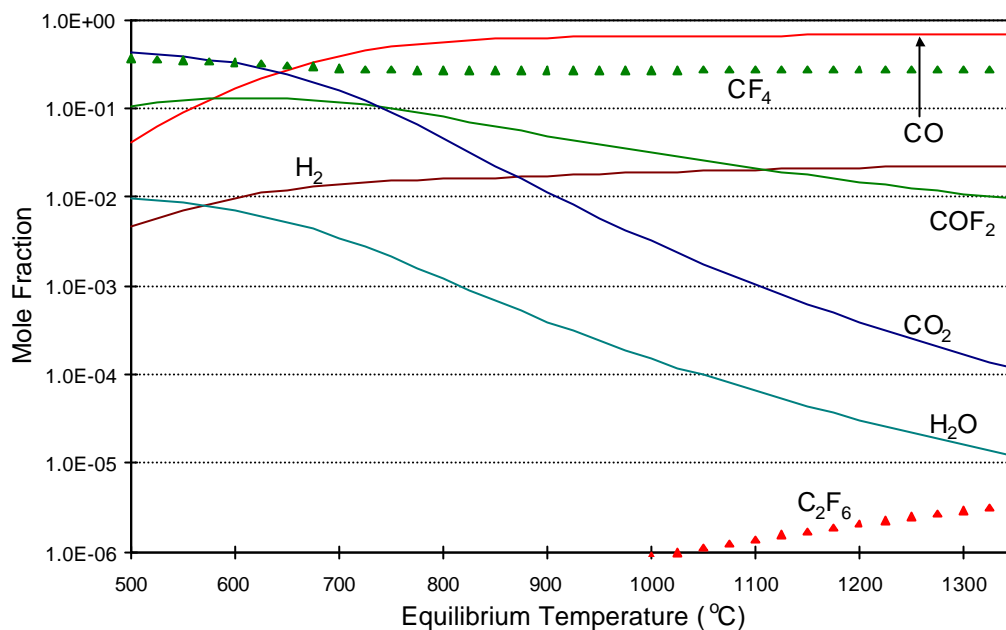
Figure 8.7 *Equilibrium gas composition: industrial cell (partially burnt), anode effect.*
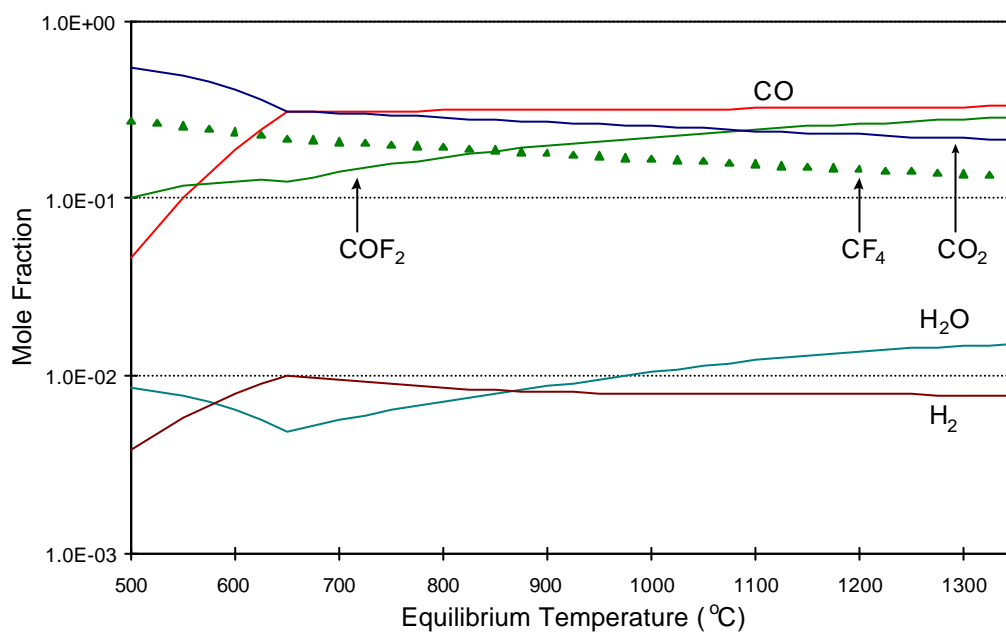
Figure 8.8 *Equilibrium gas composition: industrial cell (completely burnt), anode effect.*

The results are summarised in Table 8.4, giving the composition at 975°C, and showing the trends as the gas becomes more oxidised.

Table 8.4 Equilibrium gas composition (mol fraction) at 975°C for anode effect.

Species	Laboratory Cell	Industrial Cell Unburnt	Industrial Cell Partially burnt	Industrial Cell Completely burnt
CO_2	0.004	0.004	0.004	0.258
CO	0.632	0.619	0.653	0.318
O_2	1.1E-19	1.0E-19	1.1E-19	1.7E-15
H_2	0	0.020	0.019	0.008
H_2O	0	2.0E-04	1.9E-04	0.010
CF_4	0.311	0.303	0.272	0.171
C_2F_6	9.5E-07	9.1E-07	7.8E-07	2.4E-08
COF_2	0.037	0.035	0.035	0.217

These predictions highlight the fact that CO is the favoured carbon oxide product, even in the fully oxidised gas. CF_4 is produced in much larger quantities than C_2F_6, and COF_2 is a potential product from a thermodynamic point of view, although kinetics of its formation are not considered.

8.2. Experimental Findings.

The experimental set-up allowed tracking of gases during electrolysis, through the transition into anode effect. In Figure 8.9 the mass spectrometric response of CO, CO_2 and CF_4 are shown for an experiment. Electrolysis was from 0 to 105 minutes, when anode effect began and proceeded for approximately 10 minutes before the cell current was terminated.
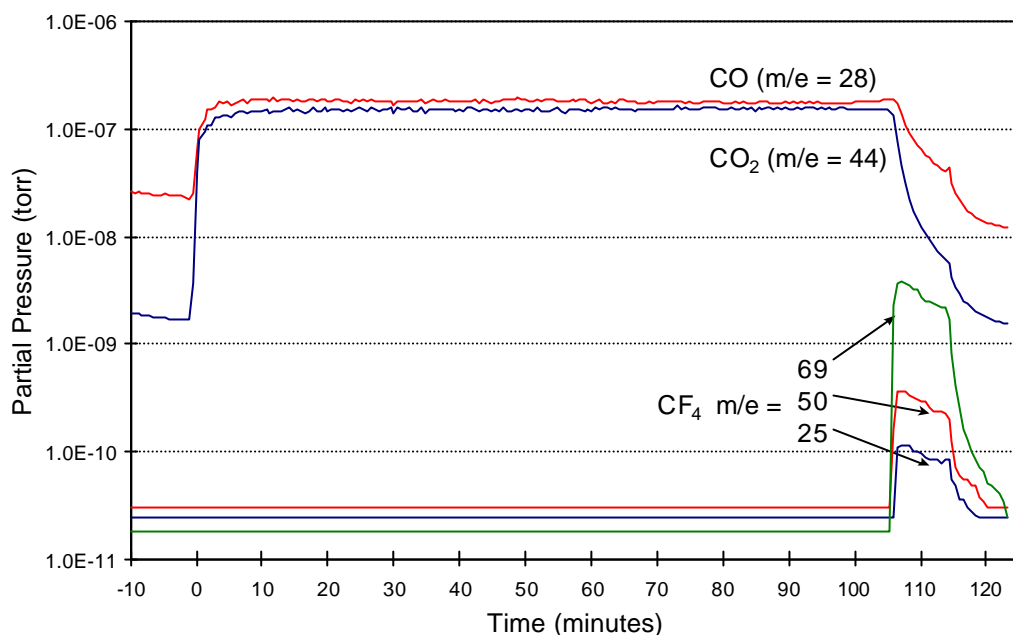
Figure 8.9 *CF_4 generation at anode effect.*

8.2.1. Comparison to Thermodynamic Predictions.

During electrolysis the levels of CO and CO_2 were similar, findings very close to the thermodynamic prediction shown in Figure 8.1. The ratio of CO to CO_2 remained steady until the last few minutes before anode effect, when the amount of CO and the CO/CO_2 ratio increased. During anode effect both CO and CO_2 dropped as the cell current decreased, however the ratio of CO/CO_2 increased as the formation of CO_2 decreased much faster and CO was the favoured gas. This agrees well with the thermodynamic predictions for the laboratory cell at anode effect shown in Figure 8.5, where the ratio of CO/CO_2 also increased significantly, and also other experimental findings such as Tabereaux *et al.* [64], where the CO_2 showed a decay while the CO increased. The laboratory cell showed a CO decrease because the current was not maintained during anode effect, however the increasing CO/CO_2 ratio is the same.

Figure 8.9 also shows the formation of CF_4 during anode effect. The partial pressures at m/e = 60, 50 and 25, all corresponding to CF_4, are at baseline levels during electrolysis. However at 105 minutes they rise suddenly as the CO and CO_2 responses decrease. While it was not possible to conclusively prove that C_2F_6 is not formed, the ion fragment at m/e = 25 (CF_2^{2+}) is only formed from the CF_4 parent, and while those at m/e = 50 (CF_2^+) and 69 (CF_3^+) could be

138

from both CF_4 and C_2F_6, the relative ratios between the three ions are consistent with the gas only being CF_4. Again the experimental findings agree with the thermodynamic predictions, as CF_4 is the prevalent fluoride species in Figure 8.5 whereas C_2F_6 is almost non-existant.

The experimental and theoretical findings agree well although they are not exactly the same. The main reasons for this are that the experimental results are a continuous measurement of a changing situation, whereas the thermodynamic predictions are of an equilibrium position. The initial conditions used for the predictions were formulated to best represent the different scenarios, although estimates were made in doing this. The most significant difference is that the thermodynamic predictions do not take any account of the mechanism of formation of any of the species considered. Therefore certain species might be predicted while there are barriers to their formation.

8.2.2. Onset of Anode Effect.

To focus on the start of anode effect, Figure 8.9 is redrawn in Figure 8.10 showing the gas analysis in more detail around the anode effect. Quite clearly the formation of CF_4, beginning between 105 and 106 minutes, occurred as a step increase rather than a gentle build-up. At the same point in time the levels of both CO and CO_2 started decreasing, as the cell current decreased due to the higher cell resistance.

To confirm the point when anode effect started, the cell voltage during electrolysis is shown in Figure 8.11.

139
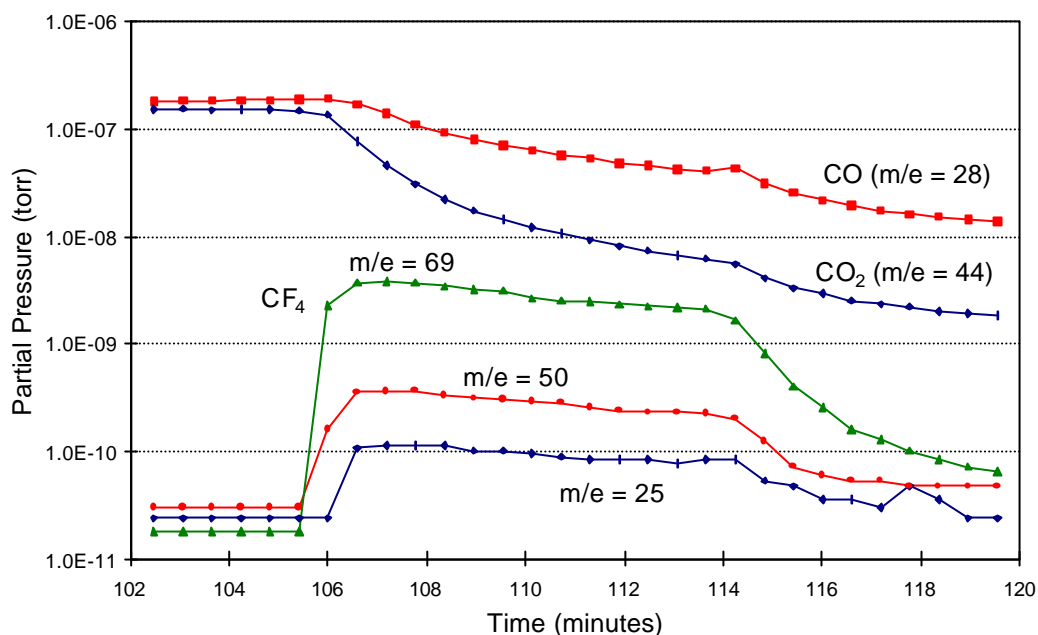
Figure 8.10 *CF$_4$ formation at anode effect: a more detailed view.*
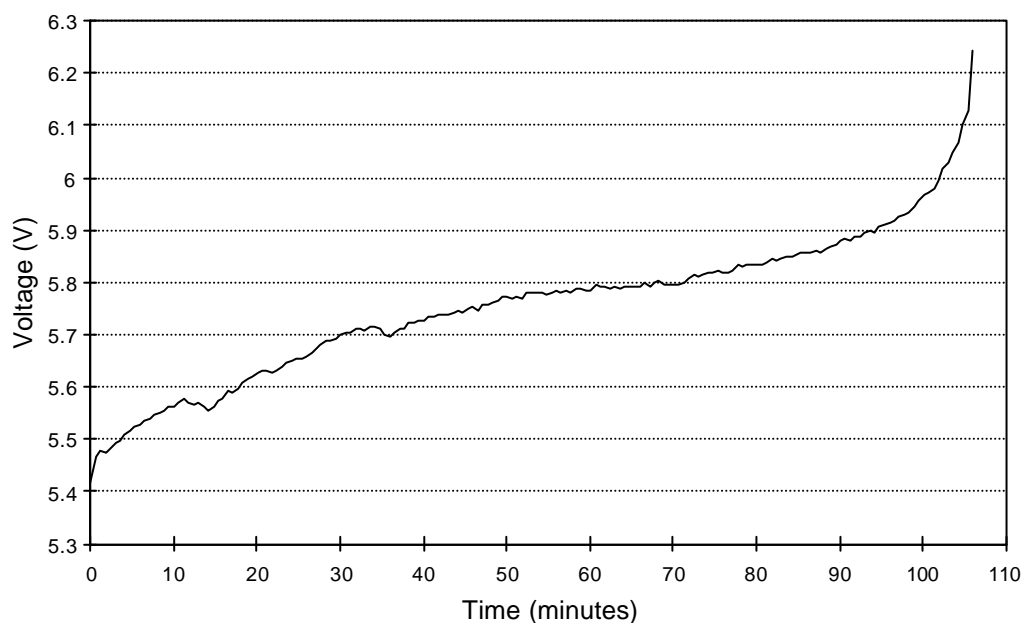
Figure 8.11 *Cell voltage during electrolysis.*

The most important feature of the cell voltage curve is the rapid increase near the end of electrolysis. The curve ended because the next voltage sample was above 10V, the limit for the data acquisition, so the actual voltage could not be determined from this point onward through the anode effect. As can be seen in Figure 8.12, the last voltage sample before 10V was exceeded coincides with the last gas analysis sample before CF$_4$ was detected. Using the definition of anode effect onset as being the sudden increase in voltage, this shows that CF$_4$

140

formation did not begin before anode effect, in direct agreement with Tabereaux *et al*. [64]. This was confirmed by checking the voltage and CF_4 responses in 22 experiments where CF_4 was targeted in the gas analysis. In every experiment there was no detection of CF_4 before the voltage showed the step increase to over 10V.
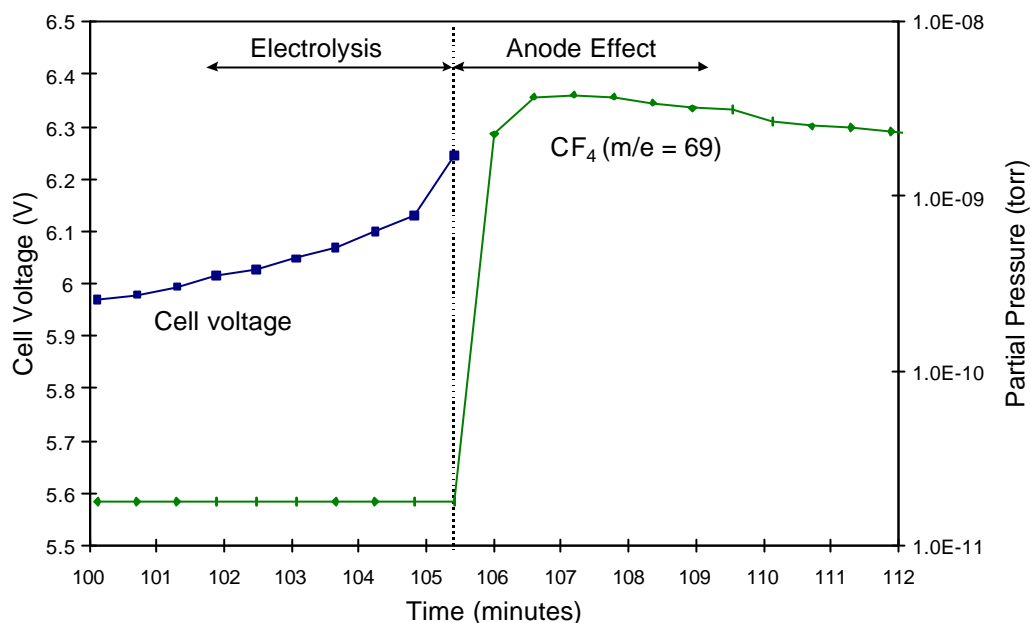
Figure 8.12 *Onset of anode effect at increased cell voltage*.

8.2.3.   Formation of COF_2.

To further investigate the onset of anode effect, the gas analysis was set up to check for the presence of carbonyl fluoride. The cell voltage was also analysed as described in section 7.2, and broken down into the different components to highlight the anode reaction polarisation. The mass spectrometric response as well as the anode reaction polarisation are shown together in Figure 8.13, which focuses on the end of electrolysis and the anode effect for the experiment.

Focussing first on the anode reaction polarisation, it can be seen that this increased by approximately 1.1V over the duration of electrolysis, 0.3V during the last 12 minutes before anode effect began after 60 minutes. The second feature is the mass spectrometric analysis, which showed CF_4 at m/e = 69 being formed only after the cell voltage had increased

stepwise to above the 10V measurement limit, clearly defining the accepted point of anode effect onset.
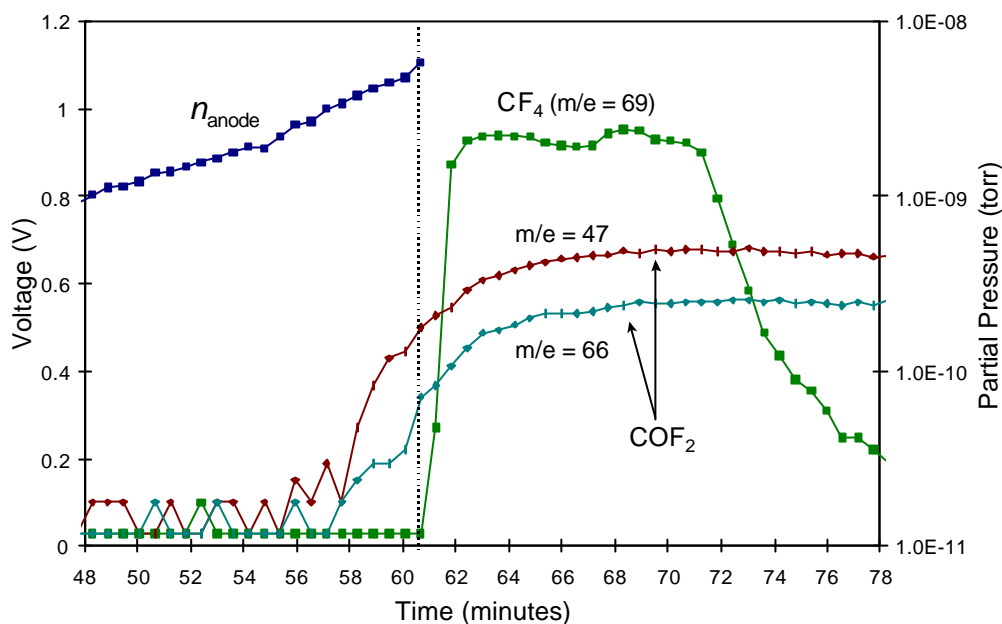
Figure 8.13 *COF$_2$ formation before anode effect onset*.

By far the most significant feature of Figure 8.13 is the response of the mass spectrometric peaks at m/e = 47 and 66. These correspond to carbonyl fluoride, the peak at m/e = 47 being the COF^+ ion and the peak at m/e = 66 being the COF_2^+ ion. The response of the two peaks is simultaneous, and the intensity ratio of m/e 66/47 remains relatively constant at 50%, agreeing well with another COF_2 analysis [85].

This evidence proves that COF_2 was formed in the laboratory cell, confirming the otherwise unproven theory of COF_2 formation in the aluminium smelting cell put forward by previous workers [54-56,59]. Even more importantly, close examination of the data in Figure 8.13 demonstrates that the formation of COF_2 began before the onset of anode effect. Both of the signals (m/e = 47, 66) rose above their baseline values and showed a response for 5 sample points before the anode effect began, a period of 3 minutes. When the corresponding polarisation data is examined, the value during the last three minutes increased from 1 to 1.1V. If the assumption is made that at the very start of electrolysis only CO was being formed by reaction *2.17* (at 1.06V), then the voltage would need to increase by at least 0.8V before COF_2 formation by reaction *2.39* (at 1.86V) would be possible.

142

$2Na_3AlF_6 + Al_2O_3 + 3C = 3COF_2 + 6NaF + 4Al$ $\qquad\qquad$ $E° = -1.86V$ (2.39)
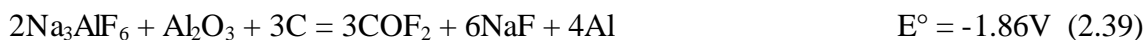
Therefore COF_2 formation was theoretically possible from 48 minutes onwards, so the detection of COF_2 is justified from an electrochemical point of view.

The findings demonstrated in Figure 8.13 were duplicated in two other experiments with the same current density of $1.107A/cm^2$. Responses of the mass spectrometric peaks at $m/e = 47$ and 66 were detected at 5 and 6 scans before anode effect started (2.9 and 3.5 minutes). The polarisation increases from the start of electrolysis until the point COF_2 was first detected were 1.15 and 1.05V, in close agreement with the 1V above.

There are several possible reasons why COF_2 has not been detected in previous studies, but has been seen here. The most likely reason is that in industrial cells, any COF_2 formed will decompose by hydrolysis to form HF and CO_2 by reaction *2.42*:

$COF_2 + H_2O = CO_2 + 2HF$ $\qquad\qquad\qquad\qquad\qquad\qquad\qquad\qquad\qquad$ (2.42)
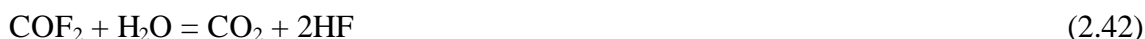
This reaction is excluded in the laboratory cell because of the lack of moisture due to the preheating of the electrolyte components and scrubbing alumina, the controlled atmosphere and continual gas purging.

The detection of COF_2 before anode effect lends weight to the theory that it is a precursor to anode effect. As discussed in section 2.7, it is possible for COF_2 to react with carbon, forming CF_4 and CO, with a favourable equilibrium constant at cell temperatures.

$2COF_2 + C = 2CO + CF_4$ $\qquad\qquad\qquad\qquad\qquad\qquad\qquad\qquad\qquad$ (2.40)

The CF_4 formed could be the very start of the film that is eventually present on the anode underside during anode effect. Therefore if COF_2 could be detected in industrial cells, it could be used in conjunction with cell voltage monitoring to provide early warning of anode effect and trigger remedial action such as alumina feeding.

The formation of COF_2 by reaction *2.39* and subsequent reaction producing CF_4 (*2.40*) also opens up the possibility of anode effect starting before the recognised step increase in cell

143

voltage. If anode effect was characterised by the presence of CF_4 in the gas under the anode then this could be well before the voltage had reached a level that permitted the direct formation of CF_4 by reaction *2.37*:

$$4Na_3AlF_6 + 3C = 12NaF + 4Al + 3CF_4 \qquad\qquad E° = -2.54V \quad (2.37)$$
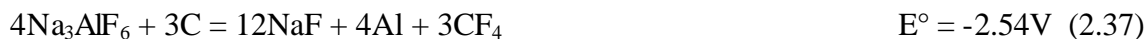
The sequence of events in the cell leading up to anode effect may even be considered in a different manner. The detection of COF_2 suggests that as the polarisation increases with decreasing alumina concentration, reaction *2.39* is initiated. The COF_2 formed then reacts with the anode carbon (*2.40*) producing CF_4. This CF_4 builds up as a film under the anode, accelerating the rate at which the voltage increases due to the increased resistance. The CF_4 film reaches sufficient thickness to become insulating, causing a step increase in the voltage [96], at which point direct electrochemical formation of CF_4 by reaction *2.37* begins. Therefore COF_2 plays an important role as an intermediate compound in the onset of anode effect.

8.2.4.   Involvement of Boron Nitride.

Because of the presence of boron nitride in the equipment, reactions between boron nitride and the cell products were investigated. The most thermodynamically favoured reactions are with COF_2 and CF_4:

$$3COF_2 + 2BN = 2BF_3 + 3CO + N_2 \qquad\qquad K\ (970°C) = 9.22E+32 \quad (8.2)$$

$$6CF_4 + 2BN = 2BF_3 + C_2F_6 + N_2 \qquad\qquad K\ (970°C) = 3.80E=12 \quad (8.3)$$

Out of both general interest and to test the accuracy of the thermodynamic calculations, the gas analysis was set to detect BF_3. The detection of boron containing species is aided by boron having two main isotopes, 80% at molecular weight 11 and 20% at 10. Thus any boron containing ions will be present in the gas analysis in pairs, 1 mass unit apart. Figure 8.14 shows the mass spectrometric response when ions corresponding to BF_3 were targeted.
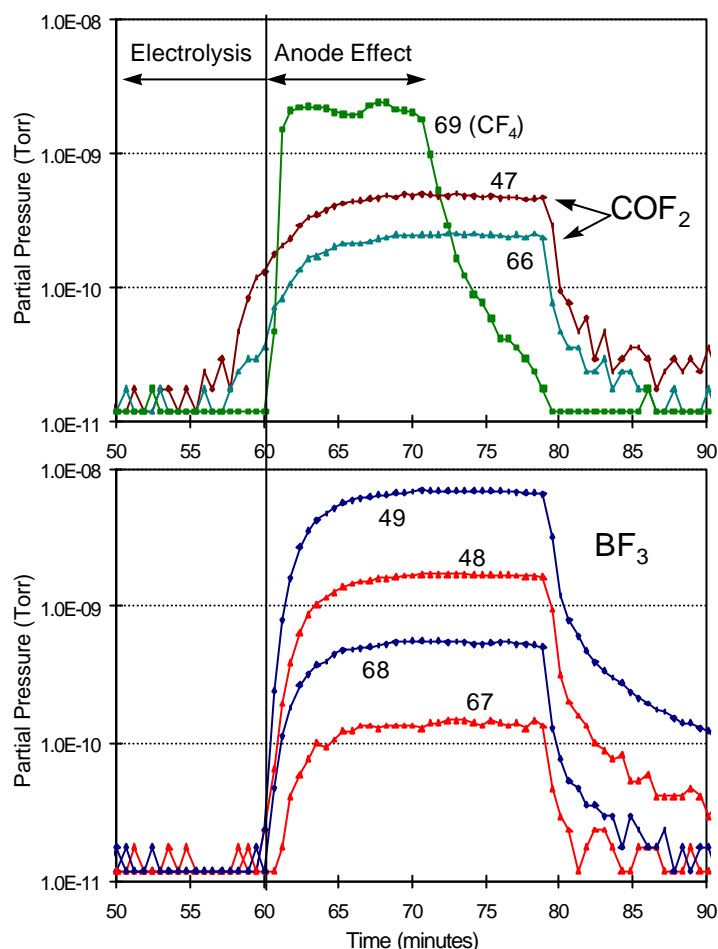
Figure 8.14 *Formation of BF₃ at anode effect.*

The upper section of the graph shows the data as in Figure 8.13, to define when anode effect began. The lower section shows the traces at m/e = 68 and 67 which correspond to the BF_3^+ ion, and those at m/e = 49 and 48 which correspond to the BF_2^+ ion. All four of these ions showed a definite response beginning at 60 minutes. The intensity ratio at 68/67 is the same as at 49/48, showing that the gas formed was BF_3, and it occurred immediately the cell went on anode effect. This suggests that reaction *8.2* between BN and CF_4 definitely occurred, however reaction *8.3* is not precluded. In fact the BF_3 response continued to mirror that of COF_2 after the CF_4 response dropped away.

Three experiments with a current density of 1.107 A/cm² showed BF_3 formation only during anode effect as above, while two others at a reduced current density of 0.295 A/cm² showed BF_3 produced before the onset of anode effect at the same time as COF_2. Because of the differing relative gas formations it is uncertain if the reactions forming COF_2 and BF_3 are coupled.

145

The formation of BF_3 indicates that the boron nitride in the cell did react, although it must be recognised that this is a phenomenon relevant only to laboratory cells containing BN, and also that this does not compromise the level of performance of the cell.

8.3.   Summary.

The thermodynamic modelling showed CO_2 and CO to be formed in similar levels in the unburnt or unoxidised regions such as under the anodes or the laboratory cell.   As the oxidation level increased, the ratio of CO_2/CO also increased.   Gas analysis from the laboratory cell confirmed the high CO levels, with in some cases more CO being formed than CO_2.   Using the modelling, CF_4 was shown to be the dominant fluorine containing species during anode effect, although COF_2 became important when the gas became oxidised.

Analysis of laboratory cell gas showed CF_4 being formed during anode effect, and not during normal electrolysis, with a clearly defined point when anode effect began as the cell voltage increased suddenly. COF_2 was detected in the cell gas shortly before anode effect began, after the cell voltage had increased through polarisation to a level where its electrolytic production was possible. BF_3 was also detected in the cell gas at and shortly before anode effect, indicating some reaction with the boron nitride used in the cell.

Except for the detection of COF_2, all of the findings outlined in this chapter agree with the results of previous studies into cell gas composition and anode effect.   The findings showing the formation of COF_2 confirm the speculation of previous publications that it can be formed and is a possible precursor to anode effect.

9.   Forms of Sulfur Released from the Cell.

This chapter outlines the findings of the experiments and thermodynamic modelling described in chapter 8, however concentrates on the sulfur containing gases produced during normal electrolysis and through the transition into anode effect. The predictions of sulfurous species, based on the initial conditions in Tables 8.1 and 8.2, and the corresponding experimental findings are discussed.

9.1.   Thermodynamic Predictions.

Predictions were made of the equilibrium composition of the cell product gas using the thermodynamic approach and oxidation states outlined earlier.

Figure 9.1 shows the predicted composition for the laboratory cell. The CO_2 and CO are as seen in Figure 8.1, however the vertical scale has been increased and the sulfurous species added. At cell operating temperatures COS is found in the greatest levels, with S_2 also significant. SO_2 and CS_2 are found to a much lesser extent, although SO_2 increases at higher equilibrium temperatures. The ratio of COS to S_2 increases as the temperature decreases, possibly due to the reaction of CO and S to form COS (*2.46*), as the equilibrium constant for this reaction increases with decreasing temperature. The formation of COS is very important from an environmental point of view, because it has a long atmospheric life where it reacts with water to form sulfuric acid, which catalyses reactions of ozone destruction [73].

The unburnt industrial cell gas scenario in Figure 9.2 and partially burnt gas in Figure 9.3 are almost identical to the predicted laboratory cell gas, except for the addition of some H_2S, obviously a result of the water vapour added to the initial conditions.

Once again the transition to completely burned gas (Figure 9.4) brings about the biggest change to the predicted gas composition. SO_2 becomes the only sulfurous species present in any levels above a very low trace.
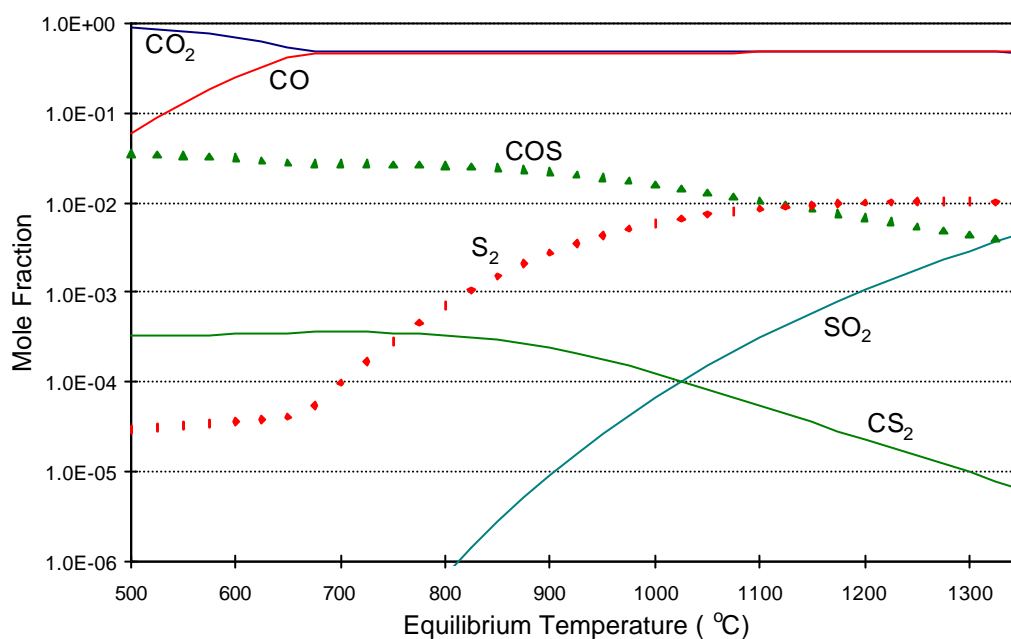
Figure 9.1 *Equilibrium gas composition: laboratory cell, electrolysis.*
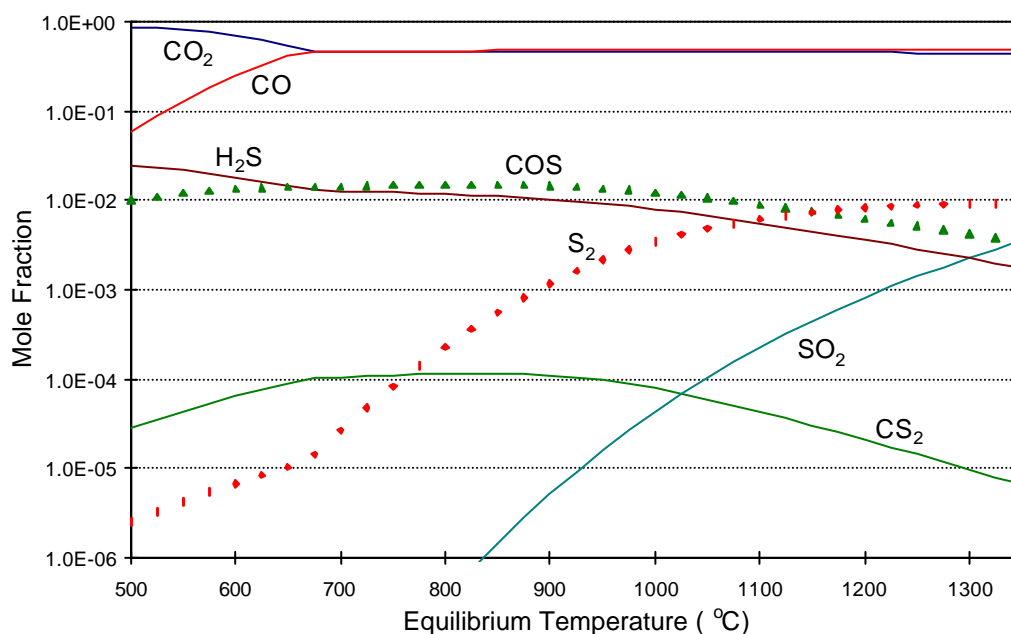
Figure 9.2 *Equilibrium gas composition: industrial cell (unburnt), electrolysis.*
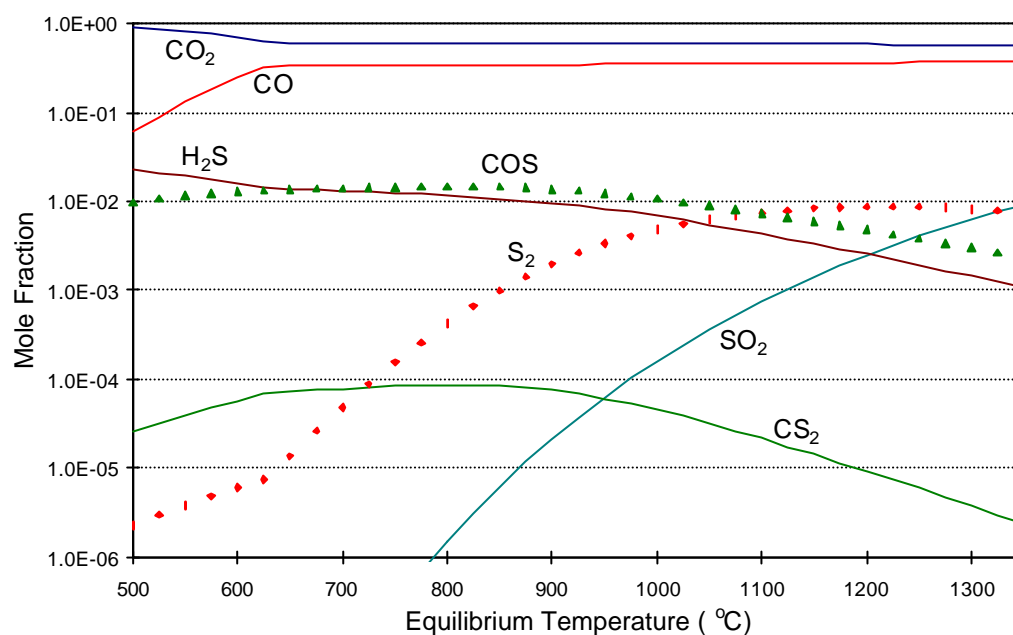
Figure 9.3 *Equilibrium gas composition: industrial cell (partially burnt), electrolysis.*

Figure 9.4 *Equilibrium gas composition: industrial cell (completely burnt), electrolysis.*

The gas compositions at 975°C for the normal electrolysis scenarios are given in Table 9.1, demonstrating the trend of COS being oxidised to form SO_2 as the oxidation state of the system is progressively increased.

149

Table 9.1 Equilibrium gas composition (mol fraction) at 975°C for electrolysis.

Species	Laboratory Cell	Industrial Cell Unburnt	Industrial Cell Partially burnt	Industrial Cell Completely burnt
CO_2	0.497	0.466	0.599	0.889
CO	0.479	0.484	0.351	2.0E-07
COS	0.018	0.013	0.012	2.3E-19
SO_2	4.3E-05	2.7E-05	1.0E-04	0.025
S_2	0.005	0.003	0.004	5.0E-24
CS_2	1.5E-04	8.7E-05	5.3E-05	1.4E-38
H_2S	0	0.009	0.008	1.6E-19

The predictions show CS_2 as an important product in all but the fully oxidised scenarios. This agrees with the experimental findings of Thonstad *et al*. [97], whereas previously CS_2 was considered to be much less significant [62,72,75]. The method of formation of CS_2 is not clear, possibly due to chemical reactions or from direct volatilisation [97].

The reactions involving sulfur and its form when released from the cell have a major impact on the carbon consumption. If the sulfur reacted and was released as SO_2 (as opposed to carbon released as CO_2) then the carbon (anode) consumption would only be different by the higher molecular weight of sulfur multiplied by the fraction of sulfur in the anode. However when COS is formed instead, the carbon (anode) consumption is increased dramatically as the ratio of anode material (carbon or sulfur) to oxygen increases fourfold. The formation of CS_2 and S_2 has an even stronger effect, consuming anode material without reducing any alumina in the electrolyte. Therefore while the only sulfurous species of any significance in the final oxidised gas released from the cell is SO_2, the actual impact on the carbon consumption is much larger because the sulfur has been initially released as COS and S_2.

In a similar manner to during electrolysis, the thermodynamic predictions of equilibrium gas concentration during anode effect are given from Figure 9.5 to Figure 9.8. The different oxidising conditions during anode effect present a different pattern of gas compositions. There is effectively no SO_2 found in the laboratory, unburnt and partially burnt scenarios, and only a very small amount in the completely burnt gas. COS, and H_2S for industrial cells, are the

favoured sulfurous species. Also of note is CS_2 being favoured ahead of S_2 in all but the completely burnt scenarios.
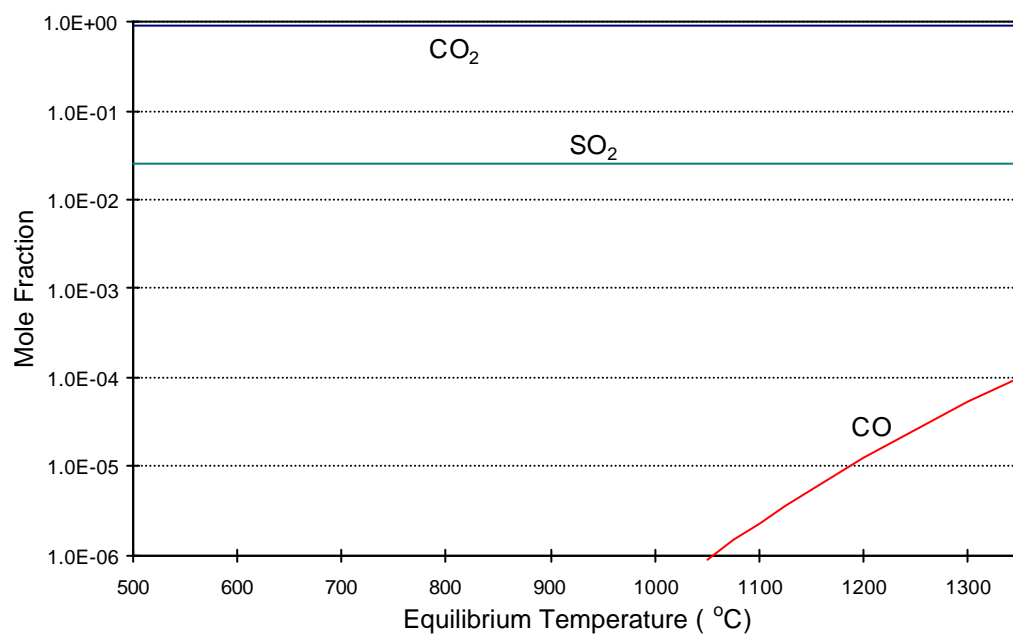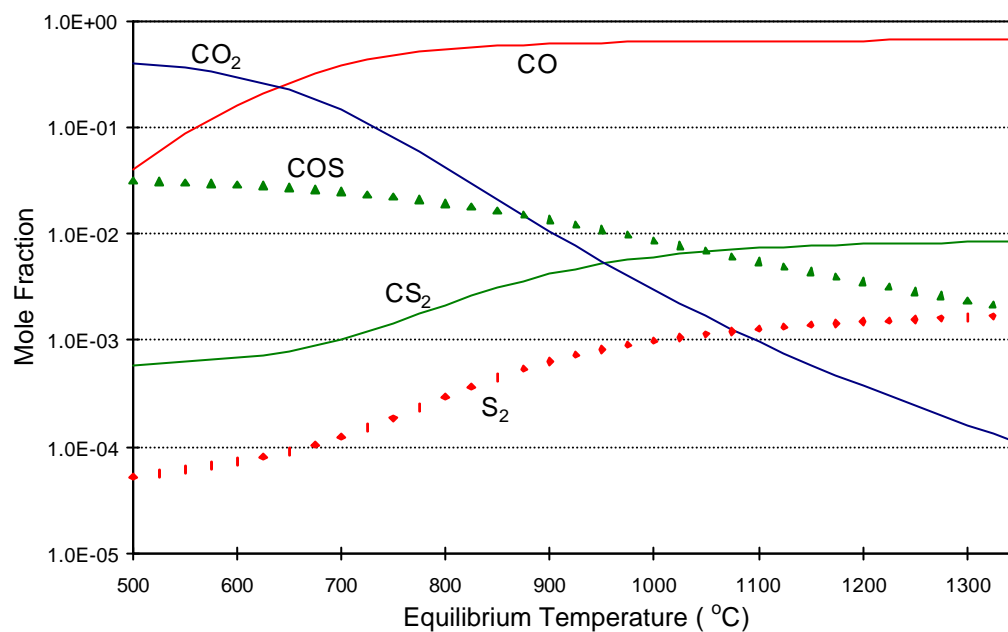

Figure 9.5 *Equilibrium gas composition, laboratory cell, anode effect.*
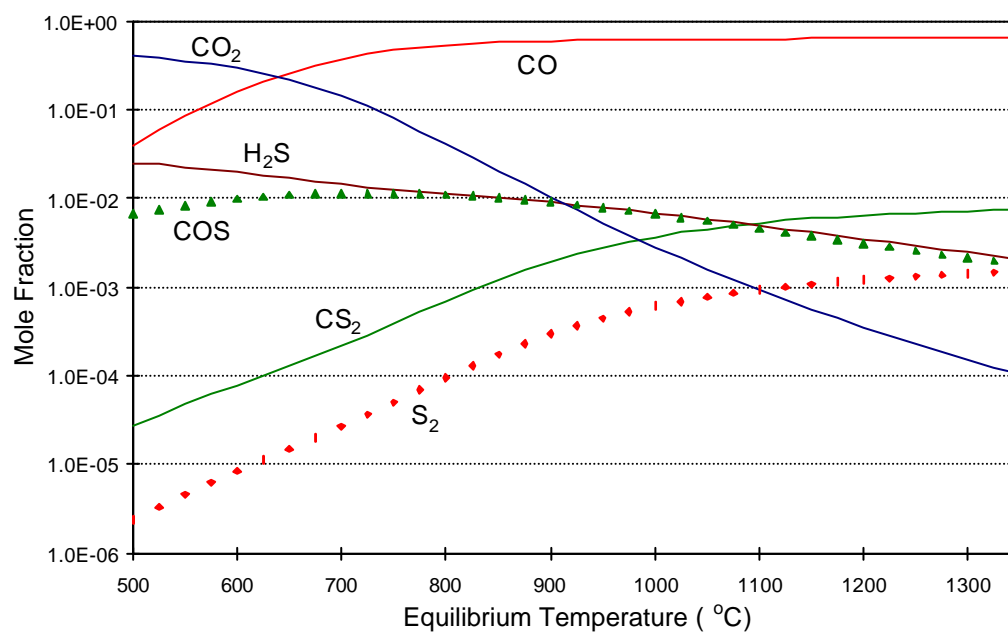
Figure 9.6 *Equilibrium gas composition: industrial cell (unburnt), anode effect.*
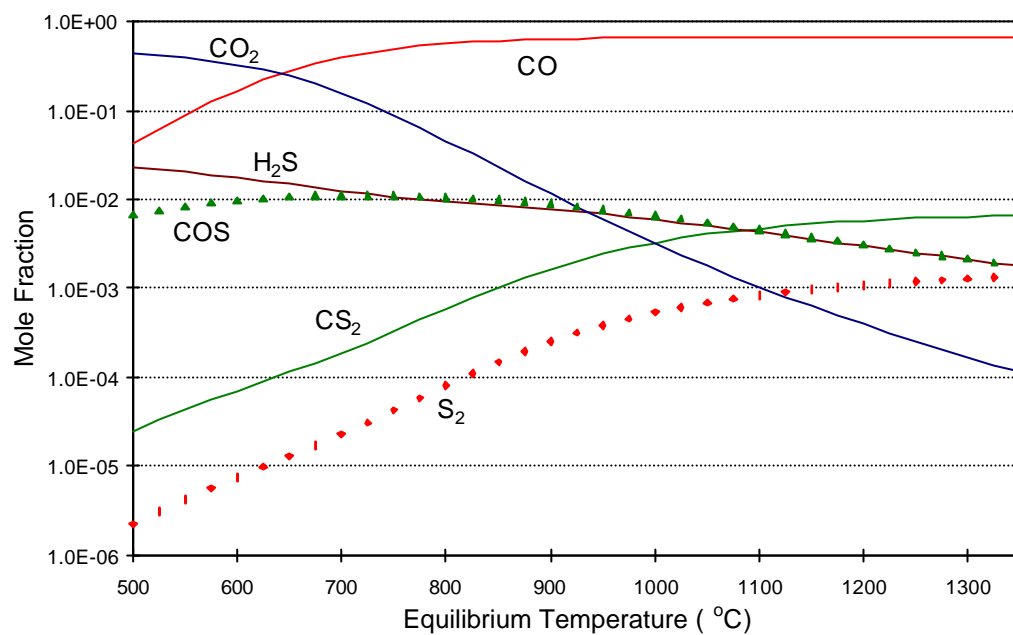
Figure 9.7 *Equilibrium gas composition: industrial cell (partially burnt), anode effect.*
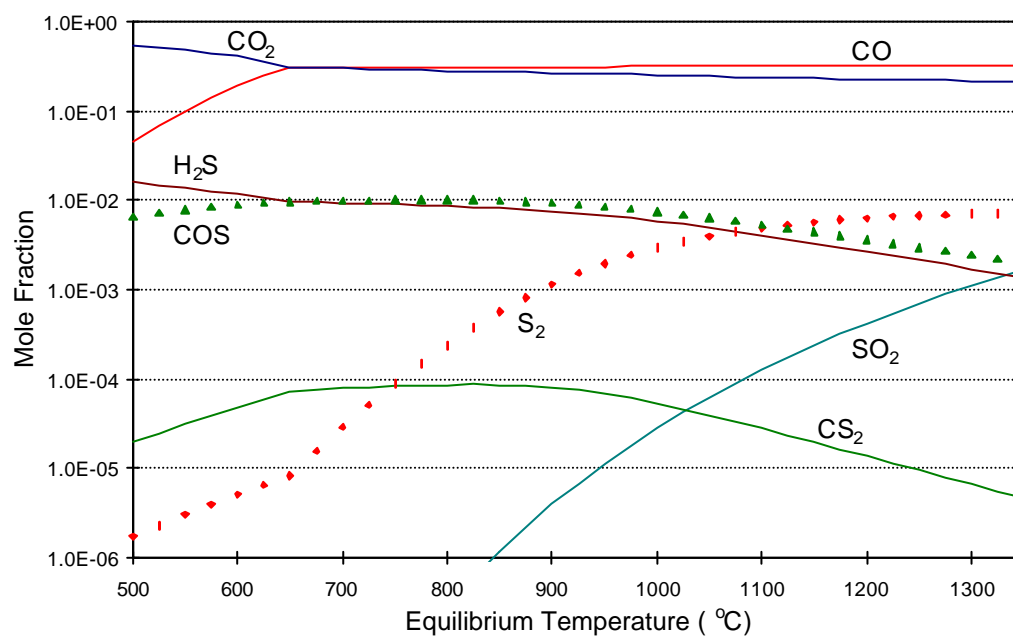
Figure 9.8 *Equilibrium gas composition: industrial cell (completely burnt), anode effect.*

The values at cell operating temperature are given in Table 9.2.

152

Table 9.2 Equilibrium gas composition (mol fraction) at 975°C for anode effect.

Species	Laboratory Cell	Industrial Cell Unburnt	Industrial Cell Partially burnt	Industrial Cell Completely burnt
CO_2	0.004	0.004	0.004	0.258
CO	0.632	0.619	0.653	0.318
COS	0.010	0.007	0.007	0.008
SO_2	6.8E-10	4.9E-10	5.1E-10	1.8E-05
S_2	9.1E-04	5.3E-04	4.6E-04	0.002
CS_2	0.006	0.003	0.003	6.0E-05
H_2S	0	0.007	0.006	0.006

The predictions at anode effect show that sulfur causes an even larger increase in carbon consumption at anode effect than during normal electrolysis, because even less sulfur is released as SO_2 and more as COS, S_2 and CS_2.

The predictions of sulfurous species during both normal electrolysis and anode effect agree closely with the experimental findings of both Henry and Holliday [52], Oedegard *et al*. [72], Kimmerle *et al*. [75] and Thonstad *et al*. [97]. These studies all showed COS favoured in unoxidised gas, and SO_2 formed as the oxidation level increased. CS_2 was only found in significant levels in unoxidised anode effect gas, with these predictions confirming its oxidation to SO_2 in the fully burnt gas.

9.2. Experimental Findings.

The mass spectrometer was configured to monitor the mass spectral peaks corresponding to SO_2, S_2, COS, H_2S and CS_2, during normal electrolysis and through the transition to anode effect. In all the experiments when sulfurous species were targeted, there was no response to any of the sulfurous species peaks other than those corresponding to COS. The response from COS at m/e = 60 can clearly be seen in Figure 9.9, starting when electrolysis began at 0 minutes, and continuing until anode effect at 106 minutes, when it dropped away in a similar manner to CO and CO_2.
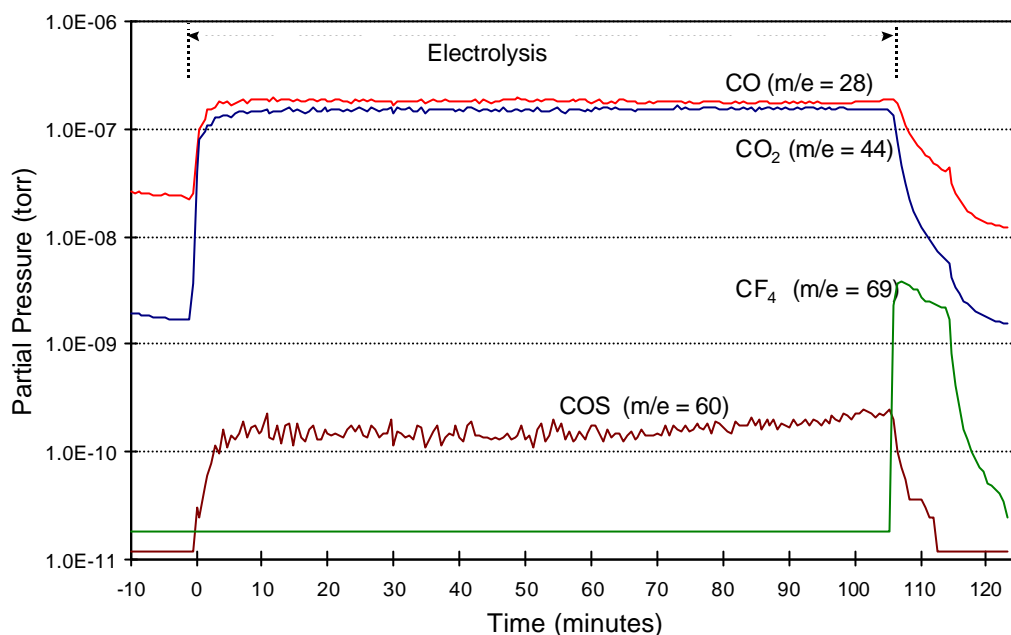
Figure 9.9 *Formation of carbonyl sulfide during electrolysis.*

The response at m/e = 60 was reasonably consistent throughout electrolysis, although it increased slightly as anode effect was approached, during a period when the ratio of CO to CO_2 also increased slightly. The similarity in the pattern of responses of COS, CO and CO_2 and the way COS dropped away as the current decreased during anode effect suggests that the formation of COS is either electrolytic, through reaction *2.44*:

$$Al_2O_3 + 3C + 3S = 3COS + 2Al \tag{2.44}$$

or directly related to the main products of electrolysis (CO and CO_2), especially by reaction *2.45*:

$$S + CO_2 + C = COS + CO \tag{2.45}$$

This is further supported by the agreement with the thermodynamic predictions, as in both the predictions and actual measurements COS was the only significant sulfurous species during electrolysis.

The second conclusion that can be drawn from these investigations is that the sulfur in the anodes is released initially as COS, which is then oxidised, not necessarily completely, to SO_2 as the gas passes through zones of higher oxidation potential and escapes the cell. The

thermodynamic predictions indicate a small amount of sulfur during electrolysis for the laboratory cell, although the gas analysis showed no indication of this. However if any sulfur was released it would condense in the gas collection system and therefore not reach the detector of the mass spectrometer, so no response is expected.

9.3.   Summary.

The findings of both the theoretical and practical investigations show very good general agreement with previous studies [52,72,75,97], with the most significant finding confirming the initial release of sulfur from anodes as COS, which then becomes oxidised to SO_2.as the gas escapes from under the anodes and through the crust of the cell. During anode effect the different oxidation conditions in the cell mean that COS remains the significant sulfurous species produced. Sulfur is also shown to be important to the carbon consumption of the cell, depending on the form of sulfur when initially released from the anode.

10. Conclusions and Implications of the Research.

10.1. Accuracy and Success of the Method Developed.

A laboratory scale aluminium cell and gas analysis system was designed that enabled detailed investigations into the current efficiency of the cell using the oxygen balance method. The system also allowed analysis of the gaseous species produced in the cell during electrolysis and anode effect. The cell was constructed to mimic an industrial cell as closely as possible, although the cell was operated without an initial metal layer at the cathode to avoid complications during operation. Boron nitride shielding was utilised in the cell to accurately define the anode and cathode areas. The cell current used was much larger than in previous laboratory studies, while maintaining a current density similar to that used in industrial cells, providing a larger volume of reaction gases for analysis. The reaction gases were continuously flushed from the cell with an inert carrier gas. This allowed for continuous gas analysis and hence current efficiency determination at a frequency of nearly every 30 seconds.

The current efficiency, calculated using a modified oxygen balance showed very good accuracy when compared to that calculated by the actual depletion of alumina in the electrolyte. The current efficiency was shown to have a variability about a mean value, which was genuine and not caused by uncertainties in the measurements in the system.

10.2. Cell Performance and Current Efficiency Trends.

The general performance of the cell was shown to be slightly lower than that of industrial cells under similar operating conditions. This was primarily due to a lack of metal pad at the cathode at the start of electrolysis, causing a larger back reaction between dissolved metal and carbon dioxide. The boron nitride used in the cell was also shown to have no effect on the current efficiency.

156

The cell was designed without a metal pad at the cathode, which meant that no influence of anode-cathode distance on current efficiency was expected, which was confirmed by experimental measurements. The effect of current density was investigated between 0.3 and 1.1 A/cm^2. The influence on current efficiency was strong at 17.25 %CE per A/cm^2, in agreement with other studies, although this was only across the range stated. Current densities below 0.3 A/cm^2 were not investigated because the experimental system was unsuited to such low cell currents, however the current efficiency would be expected to drop away significantly as shown by other researchers. The effect of electrolyte chemistry was studied by varying the excess aluminium fluoride content in the electrolyte, giving cryolite ratios between 1.99 and 3. Once again a strong effect, of -7.8 %CE per unit cryolite molar ratio, was found. As well as establishing the performance characteristics of this cell, this was again in agreement with previous studies, and gave further verification of the current efficiency determination method.

Because of the uncertainty in the effect of alumina concentration on current efficiency in the literature, particular attention was paid to this. The current efficiency was shown to vary from sample to sample as the alumina concentration decreased towards anode effect, however in all cases a straight line could be fitted to the current efficiency curve after the start-up period was disregarded. The largest effect of alumina found in this study was still smaller than the smallest effect found in all of the previous studies except for one. The overall average effect found was -0.0376 %CE/wt% Al$_2$O$_3$, effectively no influence, in direct agreement with one other study using a sound experimental technique on a laboratory cell. This suggests that while in many other studies an influence of alumina concentration was found, the current efficiency was actually influenced by the cell stability, which varied as the alumina concentration changed through processes such as alumina feeding or dissolution of sludge from the cathode.

The most significant implication of this finding is that the alumina concentration itself should not be the prime consideration when operating a cell, rather the level of cell stability and minimising disruptions to the cell should take precedence. Isolating the operating variables in a cell is difficult, extremely so in the industrial environment. Therefore it may be more effective to consider all of the main variables in the operating strategy of a cell so that so that the best balance of current efficiency, energy consumption, anode carbon consumption and cell stability is found.

157

10.3. Cell Voltage Analysis.

A repeatable cell voltage pattern was shown, which featured an initial rapid increase due to cell resistance and polarisation changing, attributed to electrode surface reactions involving sodium and aluminium carbides. After the starting period, the voltage consistently increased, due primarily to electrode polarisation.

Cell voltage analysis by current interruption and identifying the nernst, polarisation and ohmic components showed the polarisation to be strongly dependent on the alumina concentration, whereas current density and anode-cathode distance had no noticeable effect. The magnitude of the polarisation increase across a normal operating alumina concentration range was 0.5 to 0.7V. Complementary voltage analysis by calculation of the individual components and determining the polarisation by difference showed very similar results.

Further voltage analysis has shown the alumina activity contribution to the total cell voltage to be very small, and of little influence to the shape of the polarisation curve. The value of the index in the activity equation from Rolin [6] was examined, and the difference between 1 and 2.77 was insignificant relative to the magnitude of the anode reaction polarisation.

The research has shown how cell voltage tracking can be taken further to determine the individual voltage components, which provides more information about the state of the cell, as some components are alumina concentration dependent while others are not.

10.4. The Anode Effect and Fluoride Compounds.

Thermodynamic calculations of the gases produced in the cell predict CO and CO_2 in similar levels in unoxidised gas during normal electrolysis. As the oxidation level is increased, the ratio of CO_2/CO shows a corresponding increase. At anode effect CF_4 was predicted as the predominant fluoride species, in concentration levels many orders of magnitude higher than C_2F_6. COF_2 was also shown to be a favoured equilibrium species for fully oxidised gases, however the mechanisms of formation were not considered.

Mass spectrometric analysis of the cell gases revealed a CO concentration higher than CO_2, the ratio increasing further during anode effect as the CO_2 dropped away faster with the

decreasing cell current. The onset of anode effect in the laboratory cell was clearly defined by the formation of CF_4, and the simultaneous step increase in the cell voltage. While these findings were in agreement with previous studies, the results when COF_2 was investigated confirmed the otherwise unproven theory postulated by some researchers. COF_2 was detected in the cell gas for a period of several minutes immediately prior to the cell going on anode effect, a time when voltage analysis indicated the anode reaction polarisation had increased sufficiently to allow the formation of COF_2 electrolytically. The positive identification of COF_2 demonstrates that a likely mechanism for the onset of anode effect is formation of COF_2 at an elevated cell potential, the subsequent reaction of COF_2 with carbon forming an initial film of CF_4 under the anode, the build-up of the CF_4 film until of sufficient thickness to become electrically insulating, and the final step of the voltage increasing rapidly due to the insulating film to an even higher potential where CF_4 and C_2F_6 are formed electrolytically.

The involvement of COF_2 in the onset of anode effect, combined with the link between cell voltage and the formation of COF_2, show how improved predictions of anode effect onset can be made to allow pro-active rather than reactive cell control to help reduce anode effects. Detection of COF_2 is not necessarily required, however detailed analysis showing the change and rate of change of cell voltage and an understanding of the anode effect onset mechanism are. An area of further work would be to define more precisely the times between the formation of COF_2, the appearance of the first CF_4 under the anode, and the point at which the cell voltage increases dramatically and CF_4 is released.

10.5. Sulfurous Species Formed in the Cell.

Thermodynamic equilibrium calculations showed carbonyl sulfide, until recently thought to be relatively unimportant, as the most important sulfurous species in the cell as it is the main form of sulfur when initially released in the low oxidation potential site under the anodes. Sulfur dioxide becomes more significant as the COS moves through the zones of increasing oxidation potential until finally mixing with the drafting air, being oxidised to SO_2. The thermodynamic calculations also revealed why many of the earlier studies discounted COS in favour of SO_2. If gas analysis was only performed on samples taken from the cell ducting or hooding, then the

gas would have already reached the environment with the greatest oxidising conditions, and most of the COS initially present would have reacted to SO_2.

Gas analysis on the laboratory cell showed that under the low oxidation potential with no free oxygen, COS was the only sulfurous species formed. This enhances the findings of the thermodynamic predictions, proving that COS is the form of sulfur when released from the anodes, and that SO_2 is a secondary species formed by the oxidation of the COS.

The major implications of COS being present in cells is firstly it must be included in the gaseous species considered when determining the exposure or required protection from exposure for personnel working in the immediate vicinity of a cell. Secondly COS must be considered in the gas treatment and scrubbing systems employed in aluminium smelters. The aim should be to eliminate COS in the final discharge to the atmosphere, because of the environmentally harmful effects, especially the damage to the ozone layer. One method may be to promote gas mixing and therefore oxidation of the COS to SO_2 before the gases reach the treatment stage, so only SO_2 has to be considered.

10.6. Future Work.

The areas covered in this study with the most promise for further work are in the investigation of current efficiency and the influence of alumina concentration, and of the anode effect phenomenon. Obviously the direction this must take is in translating the principles of this research in the laboratory to industrial cells. The challenges are to isolate cell variables to enable true measurement of the effect of alumina concentration on current efficiency in industrial cells, and also to establish the formation of COF_2 prior to the voltage increase and release of CF_4 at the start of anode effect as it is traditionally viewed. The most significant modifications to the method used here would be in the system of gas calibration, sampling and analysis. Special care would be needed to extract gas samples from under the anodes without the gas mixing with air, to allow analysis for COF_2 before it reacted with moisture present in the drafting air.

11. References.

[1]   H.S. Kenchington, J.L. Eisenhauer and J.A.S. Green, "A Technology Roadmap for the U.S. Aluminum Industry", JOM, Vol.49, No.8, 1997, 18-21.

[2]   K. Grjotheim and B.J. Welch, "Aluminium Smelter Technology", 2nd Edition, Aluminium-Verlag, Düsseldorf, 1988, p49.

[3]   B.J. Welch and A.T. Tabereaux, "A Summary of Chemical and Electrochemical Reactions in Smelting Cells", Fourth Australasian Aluminium Smelter Technology Workshop, Sydney, Australia, 1992.

[4]   N. Jarrett, "Future Developments in the Bayer-Hall-Héroult Process", in "Production of Aluminium and Alumina", A.R. Burkin (Editor), John Wiley and Sons, Chichester, 1987.

[5]   W.E. Haupin, "Energy Considerations", in "Production of Aluminium and Alumina", A.R. Burkin (Editor), John Wiley and Sons, Chichester, 1987.

[6]   M. Rolin, "Les Equilibres Chimiques dans les Bains d'Electrolyse de l'Aluminium", Edition L'Institut National des Sciences Appliquees de Lyon, Villeurbanne, France, 1973.

[7]   J. Thonstad, "Cell Voltage, Anode Effect", The International Course on Process Metallurgy of Aluminium, Course Notes, Trondheim, Norway, 1994.

[8]   R. Piontelli, B. Mazza and P. Pedeferri, "The Anodic Processes in Aluminium Cells", Electrochimica Acta, Vol.10, 1965, 1117-1126.

[9]   B.A. Sadler, B.J. Welch and S. Hume, "Anode Consumption Mechanisms", Fifth Australasian Aluminium Smelter Technology Workshop, 1995, 34-81.

[10] T.M. Hyde and B.J. Welch, "The Gas Under Anodes in Aluminium Smelting Cells Part I: Measuring and Modelling Bubble Resistance Under Horizontally Oriented Anodes", <u>Light Metals 1997</u>, 333-340.

[11] R.J. Aarberg, V. Ranuum, K. Williamson and B.J. Welch, "The Gas Under Anodes in Aluminium Smelting Cells Part II: Gas Volume and Bubble Release Characteristics", <u>Light Metals 1997</u>, 341-346.

[12] X. Wang, R.D. Peterson and A.T. Tabereaux, "A Multiple Regression Equation for the Electrical Conductivity of Cryolitic Melts", <u>Light Metals 1993</u>, 247-255.

[13] J. Hives, J. Thonstad, Å. Sterten and P. Fellner, "Electrical Conductivity of Molten Cryolite-based Mixtures Obtained with a Tube-type Cell made of Pyrolitic Boron Nitride", <u>Light Metals 1994</u>, 187-194.

[14] In reference 2, p158.

[15] In reference 2, p161.

[16] W. Zhang, "<u>Modelling of Anodic Gas Evacuation and Current Efficiency in Hall-Héroult Cells</u>", PhD Thesis, Department of Chemical and Materials Engineering, The University of Auckland, New Zealand, 1992.

[17] T.G. Pearson and J. Waddington, "Electrode Reactions in the Aluminium Reduction Cell", <u>Discussions of the Faraday Society</u>, Vol.1, 1947, 307-319.

[18] W.K. Fischer and R. Perruchoud, "Factors Influencing the Carboxy- and Air-Reactivity Behaviour of Prebaked Anodes in Hall-Héroult Cells", <u>Light Metals 1986</u>, 575-580.

[19] P. Fellner, K. Grjotheim, K. Matiaš ovský and J. Thonstad, "Current Efficiency Measurements in Laboratory Aluminum Cells", <u>Canadian Metallurgical Quarterly</u>, Vol.8, No.2, 1969, 245-248.

[20] B.A. Clover, "<u>Determination of the Performance of the Hall-Héroult Aluminium Production Cell by Gas Analysis</u>", ME Thesis, Department of Chemical and Materials Engineering, The University of Auckland, New Zealand, 1994.

[21] C. Castellano, D. Bratland, K. Grjotheim, T. Müftüoglu and J. Thonstad, "Current Efficiency Measurements in Laboratory Aluminum Cells-IV. Depletion of Alumina and Cell Voltage", <u>Canadian Metallurgical Quarterly</u>, Vol.18, 1979, 13-18.

[22] B. Lillebuen, S.A. Ytterdahl, R. Huglen and K.A. Paulsen, "Current Efficiency and Back Reaction in Aluminium Electrolysis", <u>Electrochimica Acta</u>, Vol.25, 1980, 131-137.

[23] P. Fellner, K. Grjotheim and H. Kvande, "Current Efficiency Measurements in Laboratory Aluminum Cells-VI. Back Reactions", <u>Canadian Metallurgical Quarterly</u>, Vol.23, No.4, 1984, 421-425.

[24] K. Grjotheim, F.N. Xiang, B. Haugsdal and H. Kvande, "Current Efficiency Measurements in Laboratory Aluminum Cells-XII. Low-Melting Bath", <u>Canadian Metallurgical Quarterly</u>, Vol.26, No.3, 1987, 185-188.

[25] M.J. Leroy, T. Pelekis and J.M. Jolas, "Continuous Measurement of Current Efficiency, by Mass Spectrometry, on a 280KA Prototype Cell", <u>Light Metals 1987</u>, 291-294.

[26] T.R. Alcorn, C.J. McMinn and A.T. Tabereaux, "Current Efficiency in Aluminum Electrolysis by Anode Gas Analysis", <u>Light Metals 1988</u>, 683-695.

[27] E.W. Dewing, "Loss of Current Efficiency in Aluminum Electrolysis Cells", <u>Metallurgical Transactions B</u>, Vol.22B, 1991, 177-182.

[28] F.J Stevens, W. Zhang, M.P. Taylor and J.J.J. Chen, "The Interaction Between Current Efficiency and Energy Balance in Aluminium Reduction Cells", <u>Light Metals 1992</u>, 541-547.

[29] K.A. Paulsen, J. Thonstad, S. Rolseth and T. Ringstad, "Current Efficiency as a Function of the Contents of Alumina and CaF_2 in Industrial Aluminium Electrolysis Cells", <u>Light Metals 1993</u>, 233-238.

[30] P.A. Solli, T. Haarberg, T. Eggen, E. Skybakmoen and Å. Sterten, "A Laboratory Study of Current Efficiency in Cryolitic Melts", <u>Light Metals 1994</u>, 195-203.

[31] H. Kvande, "Bath Chemistry and Aluminum Cell Performance-Facts, Fictions, and Doubts", <u>JOM</u>, Vol.46, No.11, 1994, 22-29.

[32] H. Kvande, "Current Efficiency of Alumina Reduction Cells", <u>Light Metals 1988</u>, 261-268.

[33] K. Grjotheim, C. Krohn, M. Malinovský, K. Matiaš ovský and J. Thonstad, <u>Aluminium Electrolysis-Fundamentals of the Hall-Héroult Process</u>, 2nd Edition, Aluminium Verlag, Düsseldorf, 1982, 339.

[34] In reference 33, p322.

[35] K. Grjotheim, M. Malinovský, K. Matiaš ovský, A. Silný and J. Thonstad, "Current Efficiency Measurements in Laboratory Aluminum Cells-II: Influence of Alumina Content", <u>Canadian Metallurgical Quarterly</u>, Vol.11, No.2, 1972, 295-298.

[36] R.T. Poole and C. Etheridge, "Aluminium Reduction Cell Variables and Operations in Relation to Current Efficiency", <u>Light Metals 1977</u>, 163-183.

[37] B. Lillebuen and Th. Mellerud, "Current Efficiency and Alumina Concentration", <u>Light Metals 1985</u>, 637-645.

[38] K. Grjotheim, W.E Haupin and B.J. Welch, "Current Efficiency-Relating Fundamental Studies to Practice", <u>Light Metals 1985</u>, 679-694.

[39] B. Langon and JM. Peyneau, "Current Efficiency in Modern Point Feeding Industrial Potlines", <u>Light Metals 1990</u>, 267-274.

[40] A. Solheim, S. Rolseth, E. Skybakmoen, L. Støen, Å. Sterten and T. Støre, "Liquidus Temperature and Alumina Solubility in the System Na_3AlF_6-AlF_3-LiF-CaF_2-MgF_2", <u>Light Metals 1995</u>, 451-460.

[41] R. Ødegård, Å. Sterten and J. Thonstad, "The Solubility of Aluminium in Cryolitic Melts", <u>Light Metals 1987</u>, 389-398.

[42] K. Yoshida and E.W. Dewing, "The Apparent Solubility of Aluminum in Cryolite Melts", <u>Metallurgical Transactions</u>, Vol.3, 1972, 1817-1821.

[43]   B.J. Welch, "Electrochemical Production of Quality Aluminium", <u>Alumitech 1997</u>, Proceedings, Vol.III, Aluminum Association USA, Atlanta, May 1997, 800-813.

[44]   R.A. Lewis, "Aluminum Reduction: Evaluating 5%LiF-Modified Hall Bath in 10-KA Experimental Reduction Cells", <u>Journal of Metals</u>, Vol. 19, May, 1967, 30-36.

[45]   J.W. Burck and D. Fern, "Experimentation to Modify Cell Design and Optimize the Operation in Aluminum Reduction Cells", <u>Light Metals 1971</u>, 123-131.

[46]   R. Dorin, E.J. Frazer and E.M. Vecchio-Sadus, "Current Efficiency, Mass Transfer & Bubble Evolution Characteristics in a Laboratory-Scale Alumina Reduction Cell with Optional Sleeved Anode", <u>Light Metals 1994</u>, 205-210.

[47]   T. Müftüoglu, D. Bratland, C. Castellano, K. Grjotheim and J. Thonstad, "Current Efficiency Measurements in Laboratory Aluminum Cells-V: The Influence of Stirring and LiF Additions", <u>Canadian Metallurgical Quarterly</u>, Vol.18, No.1, 1979, 19-22.

[48]   K. Grjotheim, W.Q. Bin and H. Kvande, "Current Efficiency Measurements in Laboratory Aluminum Cells-VII: Using Al-Cu Cathodes", <u>Canadian Metallurgical Quarterly</u>, Vol.24, No.1, 1985, 65-67.

[49]   R. Dorin and E.J. Frazer, "Operational Characteristics of Laboratory Scale Alumina Reduction Cells with Wettable Cathodes", <u>Journal of Applied Electrochemistry</u>, Vol.23, 1993, 933-942.

[50]   B.J. Welch, "Energy Balances in Aluminium Smelting Cells - Static and Dynamic Considerations", <u>Private Communication</u>, Department of Chemical and Materials Engineering, The University of Auckland, 1994.

[51]   In reference 2, p116.

[52]   A.T. Tabereaux, "Anode Effects, PFCs, Global Warming, and the Aluminum Industry", <u>JOM</u>, Vol.46, No.11, 1994, 30-34.

[53]   In reference 33, p281.

[54]   A.J. Calandra, C.E. Castellano and C.M. Ferro, "The Electrochemical Behaviour of Different Graphite/Cryolite Alumina Melt Interfaces Under Potentiodynamic Perturbations", Electrochimica Acta, Vol.24, 1979, 425-437.

[55]   A.J. Calandra, C.M. Ferro and C.E. Castellano, "Experimental and Theoretical Analysis of the Anode Effect on Graphite Electrodes in Molten Sodium Fluoride under Potentiodynamic Perturbations", Electrochimica Acta, Vol.25, 1980, 201-209.

[56]   S.S. Djokic, B.E. Conway and T.F. Belliveau, "Specificity of Anodic Processes in Cyclic Voltammetry to the Type of Carbon used in Electrolysis of Cryolite-Alumina Melts", Journal of Applied Electrochemistry, Vol.24, 1994, 827-834.

[57]   H.J. Eleméus and J.F. Wood, "The Preparation and Reactions of Carbonyl and Sulphuryl Fluorides and Chlorofluorides", Journal of the Chemical Society, 1948, 2183-2188.

[58]   H.V. Wartenburg, "Die Bildungswärme eineger Fluoride", Zeitschrift für anorganische Chemie, No.258, 1949, 356-360.

[59]   A. Øygård, T.A. Halvorsen, J. Thonstad, T. Røe and M. Bugge, "A Parameter Study of the Formation of C-F Gases During Anode Effect in Aluminium Reduction Cells", Light Metals 1995, 279-287.

[60]   J.C. Amphlett, J.R. Dacey and G.O. Pritchard, "An Investigation of the Reaction $2COF_2 \rightarrow CO_2 + CF_4$ and the Heat of Formation of Carbonyl Fluoride", The Journal of Physical Chemistry, Vol.75, No.19, 1971, 3024-3026.

[61]   W.D. Treadwell and A. Köhl, "Über die anodische Bildung von Kohlenstofftetrafluorid bei der technischen Aluminiumgewinnung", Helvetica Chimica Acta, Vol.9, 1926, 681-691.

[62]   J.L. Henry and R.D. Holliday, "Mass Spectrometric Examination of Anode Gases from Aluminum Reduction Cells", Journal Of Metals, October 1957, 1384-1385.

[63]   R.D. Holliday and J.L. Henry, "Anode Polarization and Fluorocarbon Formation in Aluminum Reduction Cells", Industrial and Engineering Chemistry, Vol.51, No.10, 1959, 1289-1292.

[64] A.T. Tabereaux, N.E. Richards and C.E. Satchel, "Composition of Reduction Cell Anode Gas During Normal Conditions and Anode Effects", <u>Light Metals 1995</u>, 325-333.

[65] I. Berge, R. Huglen, M. Bugge, J. Lindstrøm and T. Røe, "Measurement and Characterisation of Fluorocarbon Emissions from Alumina Reduction Cells", <u>Light Metals 1994</u>, 389-392.

[66] R.A. Roberts and P.J. Ramsey, "Evaluation of Fluorocarbon Emissions from the Aluminium Smelting Process", <u>Light Metals 1994</u>, 381-388.

[67] F.M. Kimmerle, G. Potvin and J.T. Pisano, "Measured Versus Calculated Reduction of the PFC Emissions from Prebaked Hall Héroult Cells", <u>Light Metals 1997</u>, 165-171.

[68] S.S. Nissen and D.R. Sadoway, "Perfluorocarbon (PFC) Generation in Laboratory-Scale Aluminium Reduction Cells", <u>Light Metals 1997</u>, 159-164.

[69] M.J. Gibbs and C. Jacobs, "Reducing PFC Emissions from Primary Aluminum Production in the United States", <u>Light Metal Age</u>, February, 1996, 26-34.

[70] In reference 2, p42.

[71] In reference 33, p378.

[72] R. Oedegard, S. Roenning, A. Sterten and J. Thonstad, "Sulphur Containing Species in the Anode Gas from Aluminium Cells", <u>Light Metals 1985</u>, 661-670.

[73] J. Harnisch, R. Borchers, P. Fabian and K. Kourtidis, "Aluminium Production as a Source of Atmospheric Carbonyl Sulfide (COS)", <u>Environmental Science and Pollution Research</u>, Vol.2, No.3, 1995, 161-162.

[74] J. Harnisch, R. Borchers and P. Fabian, "COS, CS_2 and SO_2 in Aluminium Smelter Exhaust: The Contribution of Aluminium Production to the Global COS Budget", <u>Environmental Science and Pollution Research</u>, Vol.2, No.4, 1995, 229-232.

[75] F.M. Kimmerle, L. Noël, J.T. Pisano and G. I. Mackay, "COS, CS_2 and SO_2 Emissions from Prebaked Hall Héroult Cells", <u>Light Metals 1997</u>, 153-158.

[76] M. Sørlie, Z. Kuang and J. Thonstad, "Effect of Sulphur on Anode Reactivity and Electrolytic Consumption", Light Metals 1994, 659-665.

[77] Z. Kuang, J. Thonstad and M. Sørlie, "Effects of Additives on the Electrolytic Consumption of Carbon Anodes in Aluminium Electrolysis", Carbon, Vol.33, No.10, 1995, 1479-1484.

[78] T. Løver, "Quantitative Quadrupole Mass Spectrometry for the Measurement of Current Efficiency of Hall-Héroult Aluminium Reduction Cells", *Sivil Ingeniør i Kjemi* Thesis, Faculty of Chemistry, The Norwegian Institute of Technology, NTH University of Trondheim, Norway, December 1993.

[79] Instruction Manual, Dycor Quadrupole Gas Analyser Operating Instructions, Ametek Process and Analytical Instruments Division, Pittsburgh, U.S.A., 1994.

[80] B-S. Hu, R-Z. Wang and S-X. Zhou, "Fragment Ion Pattern Coefficients of Quadrupole Mass Spectrometers", Journal of Vacuum Science Technology, Vol.20, No.4, April, 1982, 1031-1033.

[81] F.M. Mao and J.H. Leck, "The Quadrupole Mass Spectrometer in Practical Operation", Vacuum, Vol.37, No's.8-9, 1987, 669-675.

[82] Instruction Manual, PHI Model 2500 Secondary Ion Mass Spectrometer (SIMS), 1976, (cited in reference 79).

[83] "ASTM Special Technical Publication 356: Index of Mass Spectral Data Listed by Molecular Weight and the Four Strongest Peaks", American Society for Testing and Materials, Philadelphia, Pa, 1st Edition, July, 1963.

[84] J.R. Maher, "Mass Spectrometry of Fluorine Compounds", in "Advances in Fluorine Chemistry", Editors M. Stacey, J.C. Tatlow and A.G. Sharpe, Vol.2, Butterworths, London, 1961, 55-103.

[85] F.W. McLafferty, "The Wiley/NBS Registry of Mass Spectral Data", Wiley, U.S., 1989.

[86] In reference 2, p211.

[87]   E. Keul, "Emission Control", 13th International Course on the Process Metallurgy of Aluminium, Trondheim, Norway, 1994.

[88]   W.D. Lamb, "SO_2 in Aluminum Reduction-Cell Dry Scrubbing Systems", Journal of Metals, Vol.2, 1979, 32-37.

[89]   G. Wedde, "Improved Efficiencies in the Dry Scrubbing Process", Light Metals 1997, 183-186.

[90]   I. Utne, K.A. Paulsen and J. Thonstad, "The Emission of Carbonyl Sulphide from Prebake and Söderberg Aluminium Cells", Light Metals 1998, 293-301.

[91]   A. Silny and T.A. Utigard, "Determination of the Factors Which Control the CO/CO_2 Ratio of the Anode Gas", Light Metals 1995, 205-211.

[92]   In reference 2, p13.

[93]   A. Røstum, A. Solheim and A. Sterten, "Phase Diagram Data in the System Na_3AlF_6-Li_3AlF_6-AlF_3-Al_2O_3 Part 1: Liquidus Temperatures for Primary Cryolite Crystallization", Light Metals 1990, 311-316.

[94]   In reference 2, p66.

[95]   R.G. Haverkamp, "Towards Zero Anode Effect", Proceedings of the 6th Australasian Smelting Workshop 1998, 267-274.

[96]   A. Tabereaux, "Potroom Diagnostics", Proceedings of the 6th Australasian Smelting Workshop 1998, 237-263.

[97]   J. Thonstad, I. Utne, K.A. Paulsen and G. Svendsen, "Sulphurous Gases in Aluminium Electrolysis", Proceedings of the 6th Australasian Smelting Workshop 1998, 369-380.

12. Appendix 1: Accuracy and Variability of Current Efficiency Measurement

These calculations assume typical operating conditions of:

75A cell current

2 l/min Ar flow into the cell

6% CO_2 and 8% CO product gas concentration

Applying Faraday's law (equation *2.13*) to the main alumina reduction reaction (*2.1*) gives the theoretical amount of oxygen liberated from the cell.

Theoretical oxygen = 3.886×10^{-4} mol/s

Assuming no variation in the gas concentrations and flowrates:

Ar concentration out of the cell

$\qquad = 100 - 6\%\ CO_2 - 8\%\ CO$

$\qquad = 84\%$

Total flow rate from the cell

$\qquad = 2\ /\ 84\%$

$\qquad = 2.326$ l/min

Molar flow rate of gas from cell (using ideal gas law)

$\qquad = 0.0951$ mol/min

$\qquad = 1.585 \times 10^{-3}$ mol/s

Molar flow of CO_2 from cell

$\qquad = 1.585 \times 10^{-3} \times 0.06 \times 2$

$\qquad = 1.902 \times 10\text{-}4$ mol/s

Molar flow of CO from cell

$\qquad = 1.585 \times 10^{-3} \times 0.08$

$\qquad = 1.268 \times 10^{-4}$ mol/s

Total molar flow of oxygen from the cell

$= (1.902 + 1.268)$ x 10^{-4}

$= 3.17$ x 10^{-4} mol/s

Theoretical current efficiency

$= (3.17$ x $10^{-4}) / (3.886$ x $10^{-4})$

$= 0.8157$

$= 81.6\%$ CE

The first calculation shows the theoretical accuracy of the current efficiency measurement, which is influenced by the acuracy of the calibration gas concentrations and the gas flow rates:

Assuming the limits of accuracy in the gas concentrations and flow rates:

6% CO_2 is made up of

(0.50 l/min cal. gas x 20 mol%) / (1.17 l/min Ar + 0.50 l/min cal. gas)

limits of accuracy are $\pm$ 1% of flow rate value

$\pm$ 0.2% gas concentration

CO_2 concentration allowing for limits of accuracy

$= (0.49$ x $19.8\%) / (1.19 + 0.49)$

$= 5.775\%$

8% CO is made up of

(0.50 l/min cal. gas x 20 mol%) / (0.75 l/min Ar + 0.50 l/min cal. gas)

CO concentration allowing for limits of accuracy

$= (0.49$ x $19.8\%) / (0.76 + 0.49)$

$= 7.762\%$

Ar concentration out of the cell

$= 100 - 5.775\%$ CO_2 - 7.762% CO

$= 86.463\%$

Total flow rate from the cell

$= 1.98 / 86.463\%$

$= 2.290$ l/min

Molar flow rate of gas from cell (using ideal gas law)

$= 0.0937$ mol/min

$= 1.562 \times 10^{-3}$ mol/s

Molar flow of CO_2 from cell

$= 1.562 \times 10^{-3} \times 0.05775 \times 2$

$= 1.804 \times 10\text{-}4$ mol/s

Molar flow of CO from cell

$= 1.562 \times 10^{-3} \times 0.07762$

$= 1.212 \times 10^{-4}$ mol/s

Total molar flow of oxygen from the cell

$= (1.804 + 1.212) \times 10^{-4}$

$= 3.016 \times 10^{-4}$ mol/s

Theoretical current efficiency

$= (3.016 \times 10^{-4}) / (3.886 \times 10^{-4})$

$= 0.7761$

$= 77.6\%$ CE

Accuracy of current efficiency measurement

$= 81.6\% - 77.6\%$

$= \pm 4\%$

The second calculation shows the theoretical point to point variability in the current efficiency measurement, which is influenced by the variation in the argon flow through the cell and the variation in the partial pressure readings from the mass spectrometer.

The standard deviations of the mass spectrometer readings were determined by measuring the output for a period with a fixed gas concentration. This gave values of 0.35% of the concentration for CO_2 and 0.17% of the concentration for CO.

CO_2 variability gives concentration of 5.979%

CO variability gives concentration of 7.986%

Ar concentration out of the cell

$= 100 - 5.979\% \ CO_2 - 7.986\% \ CO$

= 86.035%

Although the actual argon flow variability used in calculations was ± 0.0004 l/min, the original measured value of ± 0.017 l/min was used to give a conservative estimate of the current efficiency variability.

Argon flow into the cell

= 2 - 0.017

= 1.983 l/min

Total flow rate from the cell

= 1.983 / 86.035%

= 2.305 l/min

Molar flow rate of gas from cell (using ideal gas law)

= 0.0942 mol/min

= 1.57×10^{-3} mol/s

Molar flow of CO_2 from cell

= $1.57 \times 10^{-3} \times 0.05979 \times 2$

= 1.877 x 10-4 mol/s

Molar flow of CO from cell

= $1.57 \times 10^{-3} \times 0.07986$

= 1.254×10^{-4} mol/s

Total molar flow of oxygen from the cell

= $(1.877 + 1.254) \times 10^{-4}$

= 3.131×10^{-4} mol/s

Theoretical current efficiency

= $(3.131 \times 10^{-4}) / (3.886 \times 10^{-4})$

= 0.8057

= 80.57% CE

Variability of current efficiency measurement

= 81.57% - 80.57%

= ± 1.00%